

# Research Proposal

**Chanaprom Cholsuk, Student ID SCPY/M 6136544**  
Department of Physics, Faculty of Science, Mahidol University

## 1 Project Title

First-principles studies of the effects of combined supervalent cations and lithium ion vacancies doping on the ionic and electronic conduction in LiFePO<sub>4</sub>

## 2 Project Advisors

### **Asst. Prof. Dr. Sujin Suwanna**

Optical and Quantum Physics Laboratory, Department of Physics, Faculty of Science, Mahidol University, Bangkok 10400, Thailand

### **Asst. Prof. Dr. Worasak Sukkabot**

Department of Physics, Faculty of Science, Ubonratchathani University, Ubonratchathani 34190, Thailand

### **Dr. Wutthikrai Busayaporn**

Synchrotron Light Research Institute, Nakhon Ratchasima 30000, Thailand

### **Dr. Pimsiree Suwanna**

Department of Materials Science, Faculty of Science, Kasetsart University, Bangkok 10900, Thailand

## 3 Introduction, Motivation and Literature Review

LiFePO<sub>4</sub> is an alternative material applied as the cathode of Lithium-ion battery because of its outstanding properties such as structural, chemical, and thermal stabilities, high voltage (approximately 3.5 volts compared with the lithium metal), high theoretical discharge capacity (170 mAh/g), environmental friendliness, and low-cost material [1]. However, it gets obstructed related to limitations used in commercial activities due to poor electronic and ionic conductivities which cause the low performance in chemical properties of the cell battery [2, 3]. Many research groups attempted to seek the methodologies to improve the conductivities of LiFePO<sub>4</sub>. One of the successful ways was doping or coating at the surface of LiFePO<sub>4</sub> with conductive nanocarbons [4, 5, 6, 7]. This method, however, did not improve mobilities of electron and ion inside the lattice structure [8]. Moreover, carbon coating sometimes became disadvantageous additional step of synthesis and made the energy density lower because of the presence of electrochemical inert about 30% of total [5, 6].

Another popular method firstly proposed by Chung *et al* [8] was doping with the positive ion being greater than Li<sup>+</sup> (supervalent cations) such as Mg<sup>2+</sup>, Al<sup>3+</sup>, Ti<sup>4+</sup>, Zr<sup>4+</sup>, or Nb<sup>5+</sup> to substitute the positive ion at M1 (Li) or M2 (Fe) in the LiFePO<sub>4</sub> structure with solid solution. This can potentially enhance the conductivities of LiFePO<sub>4</sub> about 10<sup>8</sup> at room temperature. Later, other research groups[9, 10, 11, 12, 13] also reported the corresponding experimental results. Nevertheless, role and mechanism of supervalent cations improving the electronic and ionic conductivities were unclear and conflicting arguments [14, 15]. Understanding, therefore, mechanism of conductivities by electron and ion of

pure LiFePO<sub>4</sub> and effect of doping in LiFePO<sub>4</sub> on conductivities are crucial for effectively improving efficiency and developing lithium ion battery technology.

Lattice and electronic structures of undoped and doped LiFePO<sub>4</sub> are theoretically investigated using first-principles methods by several research groups [16, 17, 18, 19]. Overall, it is acceptable that undoped LiFePO<sub>4</sub> is an insulator with high band gap energy (about 3.8 eV). Furthermore, Hoang *et al* [20] reported that LiFePO<sub>4</sub> generally has some native defects located inside the lattice structure. Such native defects which always have low formation energies comprise of small hole polaron ( $p^+$ ), lithium vacancy ( $V_{Li}^-$ ), lithium antisite ( $Li_{Fe}^-$ ), and iron antisite ( $Fe_{Li}^+$ ). They also concluded that electronic conductivity or conductivity by electron results from hopping of  $p^+$  between Fe<sup>2+</sup> and Fe<sup>3+</sup> but ionic conductivity or conductivity by ion results from diffusion of  $V_{Li}^-$  (or diffusion of Li<sup>+</sup>). Consequently, electronic conductivity depends on number or concentration of  $p^+$  but ionic conductivity depends on concentration and mobility of  $V_{Li}^-$  in moving in and out along the specific channel for lithium. If this channel is too narrow or obstructed, ionic conductivity will get worse. For example, if we have  $Fe_{Li}^+$  which has mobility less than  $V_{Li}^-$ , it will block the diffusion of lithium.

Later, Hoang *et al* [21] studied effect of impurity on electronic and ionic conductivities using first-principles methods. The results indicated that some impurity could make fermi energy closer to conduction band minimum (CBM) or valence band maximum (VBM). All of which caused the lower formation energy of some defects and subsequently produced those defects more and more. In case of positively effective charge impurity such as Al<sup>+</sup><sub>Fe</sub>, it makes fermi energy closer to CBM and causes the reduction of formation energy of  $V_{Li}^-$ . This causes the enhancements of the number of  $V_{Li}^-$  and ionic conductivity. Whereas formation energy of  $p^+$  is higher so it leads to the reductions of the number of  $p^+$  and electronic conductivity. In case of negatively effective charge impurity such as K<sup>-</sup><sub>Fe</sub>, it makes fermi energy closer to VBM and has opposite effect. However, if impurity has neutral effective charge such as Na<sup>0</sup><sub>Li</sub>, it will not affect on variations of number of  $V_{Li}^-$  and  $p^+$  and conductivities. This study reveals that doping with an impurity cannot improve both electronic and ionic conductivities at the same time. The most efficient method is doping with an impurity enhancing ionic conductivity and applies another method such as coating with carbon to improve electronic conductivity etc.

Nonetheless, the work of Hoang *et al* [21] is investigated only in case of variation of the number of defects after making charge equilibrium when doping. For instance, the number of  $V_{Li}^-$  is increased after doping with Al<sup>3+</sup> substituted at the Fe<sup>2+</sup> site (Al<sup>+</sup><sub>Fe</sub>) which has chemical equation as  $Li_{1-x}^{+} Al_x^{3+} Fe_{1-x}^{2+} [PO_4]$  where x is quantity of Al<sup>3+</sup> that substitutes at Fe<sup>2+</sup>. In case of doping with any positive charge (M<sup>n+</sup>) which has positive charge n substituting at Fe<sup>2+</sup> site, the chemical equation can be expressed as  $Li_{1-(n-2)x}^{+} M_x^{n+} Fe_{1-x}^{2+} [PO_4]$ . It can be seen that case of adding extra  $V_{Li}^-$  in the structure such as material synthesis in lithium insufficient environment has not been studied yet. This case may have an effect on the rest of Fe<sup>2+</sup> which is not substituted. These Fe<sup>2+</sup> ions need to be transformed to Fe<sup>3+</sup> to satisfy total charge equilibrium which can be expressed as  $Li_{1-x-a}^{+} Al_x^{3+} (Fe_{1-x-a}^{2+}/Fe_a^{3+}) [PO_4]$  where x is the amount of Al<sup>3+</sup> that substitutes at the Fe<sup>2+</sup> site and a is the proportion of additional  $V_{Li}^-$  (or removal Li<sup>+</sup>). Consequently, our work focus on doping with impurity in Li deficient environment. We assume that adding  $V_{Li}^-$  will increase the amount of Fe<sup>3+</sup> which improves hopping of  $p^+$  and electronic conductivity. At the same time, ionic conductivity can also be improved by doping with Al<sup>+</sup><sub>Fe</sub>. If this assumption is true, it will become one of excellent methods to improve the properties and performances of lithium battery.

## 4 Background Theory

### 4.1 Density functional theory calculation

Solving all problems associated with many-body particles needs to employ a highly efficient computer due to the complicated cumbersome equations. There are several possible methods for solving such as quantum Monte Carlo method (QMC) consisting of variational Monte Carlo (VMC) and diffusion Monte Carlo (DMC) methods. However, these approaches consume the computational cost

too much so the other possible technique is density functional theory (DFT). DFT deals with the problem based on electron density instead of wave function so it can reduces a large number of degree of freedom and can save the computational cost about thousand times compared to QMC. As a result, DFT is now widespread throughout condensed matter physics and quantum chemistry. All concepts regarding DFT are summarized below.

#### 4.1.1 Many-body Schrodinger equation

In solid state physics and quantum mechanics, a primary aim is to discover the properties existing inside nano-scale materials which exceed the limitation of classical scheme. These behaviors can be investigated through eigenvectors and eigenvalues derived from Schrodinger equation involving nuclei and electron as shown below,

$$\hat{H}\Psi_i(\vec{r}_1, \vec{r}_2, \dots, \vec{r}_N, \vec{R}_1, \vec{R}_2, \dots, \vec{R}_M) = E_i\Psi_i(\vec{r}_1, \vec{r}_2, \dots, \vec{r}_N, \vec{R}_1, \vec{R}_2, \dots, \vec{R}_M) \quad (1)$$

This is the stationary Schrodinger equation where Hamiltonian  $\hat{H}$  consists of M nuclei and N electrons.

$$\hat{H} = -\sum_{i=1}^N \frac{\hbar^2}{2m_e} \nabla_i^2 - \sum_{A=1}^M \frac{\hbar^2}{2M_A} \nabla_A^2 + \frac{e^2}{4\pi\epsilon_0} \left[ -\sum_i^N \sum_A^M \frac{Z_A}{|\vec{r}_i - \vec{R}_A|} + \frac{1}{2} \sum_i^N \sum_{j \neq i}^N \frac{1}{|\vec{r}_i - \vec{r}_j|} + \frac{1}{2} \sum_A^M \sum_{B \neq A}^M \frac{Z_A Z_B}{|\vec{R}_A - \vec{R}_B|} \right] \quad (2)$$

For tacking with all cumbersome fundamental physical constants, the atomic units are used. The length and energy are measured in terms of ground state radius (Bohr radius  $a$ ) and electron ground state energy in the hydrogen atom (Hartree  $E_H$ ) respectively. That is,  $a_0 = \frac{4\pi\epsilon\hbar^2}{m_e e^2}$  and  $E_H = \frac{\hbar^2}{m_e a_0^2} = \frac{e^2}{4\pi\epsilon_0}$ . Thus, the Hamiltonian subsequently reduces with  $\vec{r} = \frac{\vec{r}}{a_0}$  and  $\nabla^2 = \frac{\tilde{\nabla}^2}{a_0^2}$  as follows

$$\hat{H} = -\sum_{i=1}^N \frac{1}{2} \tilde{\nabla}_i^2 - \sum_{A=1}^M \frac{1}{2M_A} \tilde{\nabla}_A^2 + \left[ -\sum_i^N \sum_A^M \frac{Z_A}{|\vec{r}_i - \vec{R}_A|} + \frac{1}{2} \sum_i^N \sum_{j \neq i}^N \frac{1}{|\vec{r}_i - \vec{r}_j|} + \frac{1}{2} \sum_A^M \sum_{B \neq A}^M \frac{Z_A Z_B}{|\vec{R}_A - \vec{R}_B|} \right] \quad (3)$$

where  $\sim$  represents the dimensionless term and ignore it later for simplicity. As a result, the rescaling Schrodinger equation becomes

$$\hat{H} = -\frac{1}{2} \sum_{i=1}^N \nabla_i^2 - \frac{1}{2} \sum_{A=1}^M \frac{1}{M_A} \nabla_A^2 - \sum_{i=1}^N \sum_{A=1}^M \frac{Z_A}{r_{iA}} + \sum_{i=1}^N \sum_{j>1}^N \frac{1}{r_{ij}} + \sum_{A=1}^M \sum_{B>A}^M \frac{Z_A Z_B}{R_{AB}} \quad (4)$$

$$\hat{H} = T_e + T_n + V_{ne} + V_{ee} + V_{nn} \quad (5)$$

where A and B run over the M nuclei whereas i and j represent the N electrons. The first two terms denote the electron and nuclei kinetic energy. The remaining three terms account for the attractive coulomb interaction between the electrons and nuclei, the repulsive interaction owing to the electron-electron and nucleus-nucleus interactions respectively.

#### 4.1.2 Born Oppenheimer Approximation

According to equation.4, all interactions between nuclei and electron are considered which make the equation too complicated to solve. Thus, Born Oppenheimer approximation was proposed to simplify some terms in the equation as follows. Since mass of nucleus is much heavier than that of electron by a factor of at least 1000, the nuclei moves so slowly that it seems stationary compared to electron movement. As a result, the nuclei can be classically treated to fix with electron moving around it. This adiabatic property of nuclei can separate the degree of freedom of nuclei and electrons so some terms in equation 4 can be neglected. That is, the nuclear kinetic term is zero and its potential energy

term is almost a constant and can be treated as classical regime so the Hamiltonian is reduced to

$$\hat{H}_{electron} = -\frac{1}{2} \sum_{i=1}^N \nabla_i^2 - \sum_{i=1}^N \sum_{A=1}^M \frac{Z_A}{r_{iA}} + \sum_{i=1}^N \sum_{j>1}^N \frac{1}{r_{ij}} = \hat{T} + \hat{V}_{Ne} + \hat{V}_{ee} \quad (6)$$

This is the Hamiltonian  $\hat{H}_{electron}$  for electron part only. Hence, the nucleus energy is later added so the total energy becomes

$$E_{total} = E_{electron} + E_{nucleus} \quad (7)$$

where

$$E_{nucleus} = \sum_{A=1}^M \sum_{B>A}^M \frac{Z_A Z_B}{R_{AB}} \quad (8)$$

Now, the task is to solve the electronic Schrodinger equation which will be discussed in the next section.

#### 4.1.3 The Hartree-Fock approximation

According to equation 6, it is incompletely because electrons are fermions which are indistinguishable particles and also satisfy the Pauli exclusion principle. Thus, it needs to include additional exchange term  $K_{ij}$ . However, before dealing with the equation, we first need to have trial solution. Assume that the ground state wave function  $\Psi_0$  is approximated as an wave function  $\Psi_{HF}(\vec{r}_1, \vec{r}_2, \dots, \vec{r}_N)$ . This  $\Psi_{HF}$  should be anti-symmetric to prevent the electron having the same direction of spin. It is a function of N electrons and each electron has 6 degrees of freedom comprising of 3 spatial terms  $\phi(x, y, z)$  and 3 spin functions  $\sigma(S_x, S_y, S_z)$  so the appropriate trial wave function should be in terms of Slater determinant of spin-orbital wave function as shown in equation 9.

$$\Psi_0 \approx \Psi_{HF} = \frac{1}{\sqrt{N!}} \begin{vmatrix} \psi_1(\vec{r}_1) & \psi_1(\vec{r}_1) & \cdots & \psi_N(\vec{r}_1) \\ \psi_1(\vec{r}_2) & \psi_2(\vec{r}_2) & \cdots & \psi_N(\vec{r}_2) \\ \vdots & \vdots & & \vdots \\ \psi_1(\vec{r}_N) & \psi_2(\vec{r}_N) & \cdots & \psi_N(\vec{r}_N) \end{vmatrix} \quad (9)$$

where  $\psi_i(\vec{r}) = \phi_i(x, y, z)\sigma_+(S_x, S_y, S_z)$  for spin up or  $\psi_i(\vec{r}) = \phi_i(x, y, z)\sigma_-(S_x, S_y, S_z)$  for spin down. After that, employing variational method to calculate the energy.

$$\begin{aligned} E_{HF} &= \langle \Psi_{HF} | \hat{H} | \Psi_{HF} \rangle \\ &= \sum_{i=1}^N h_i + \frac{1}{2} \sum_{i,j=1}^N (J_{ij} - K_{ij}) \end{aligned} \quad (10)$$

where  $h_i$  is the core Hamiltonian containing kinetic energy and electron-nucleus attraction,  $J_{ij}$  is the coulomb term or Hartree term, and  $K_{ij}$  is the exchange term.

$$h_i = \int \psi_i^*(\vec{r}) \left[ -\frac{1}{2} \nabla^2 - V_{ext}(\vec{r}) \right] \psi_i(\vec{r}) d\vec{r} \quad (11)$$

$$J_{ij} = \int \int \psi_i(\vec{r}_1) \psi_i^*(\vec{r}_1) \frac{1}{|\vec{r}_1 - \vec{r}_2|} \psi_j^*(\vec{r}_2) \psi_j(\vec{r}_2) d\vec{r}_1 d\vec{r}_2 \quad (12)$$

$$K_{ij} = \int \int \psi_i^*(\vec{r}_1) \psi_j(\vec{r}_1) \frac{1}{|\vec{r}_1 - \vec{r}_2|} \psi_i(\vec{r}_2) \psi_j^*(\vec{r}_2) d\vec{r}_1 d\vec{r}_2 \quad (13)$$

However, Hartree-Fock method still has an issue associated with ignoring the electrons correlations. This issue is tackled by Kohn-Sham approach fulfilling the equation by adding new exchange-correlation potential term. The details are discussed in the next sections.

#### 4.1.4 The Hohenberg-Kohn theorems

As mentioned earlier, the many-body Schrodinger equation can be solved using several methods. One of methods is density functional theory (DFT) which treats electrons as the density. Thus, this section describes why we can always find  $E[\rho]$  and why we can always find  $\rho(\vec{r})$  from minimising  $E[\rho]$ .

The first theorem states that the external potential  $V_{ext}(\vec{r})$  is uniquely determined by the ground state density  $\rho(\vec{r})$ . In other words,  $V_{ext}(\vec{r})$  is one to one mapping with  $\rho(\vec{r})$  so each  $V_{ext}(\vec{r})$  cannot provide the same density  $\rho(\vec{r})$ . As a result, the ground state density  $\rho(\vec{r})$  can represent all ground state properties. In addition, the kinetic energy, the potential energy, and the total energy can be expressed in terms of  $\rho(\vec{r})$  that are  $T[\rho]$ ,  $V[\rho]$ , and  $E[\rho]$  respectively.

$$E[\rho] = E_{Ne}[\rho] + T[\rho] + E_{ee}[\rho] \quad (14)$$

$$= E_{Ne}[\rho] + T[\rho] + J[\rho] + E_{ncl}[\rho] \quad (15)$$

$$= \int \rho(\vec{r}) V_{Ne}(\vec{r}) d\vec{r} + T[\rho] + \frac{1}{2} \int \int \frac{\rho(\vec{r}_1)\rho(\vec{r}_2)}{r_{12}} d\vec{r}_1 d\vec{r}_2 + E_{ncl}[\rho]$$

where the third term is classical part but the last term is not classic. The explicit forms of  $T[\rho]$  and  $E_{ncl}[\rho]$  are still unclear. According to this first theorem and equation 15, all energies can be expressed as a term of density  $\rho(\vec{r})$  as shown below.

Normally, the electron density for many-body particles are

$$\begin{aligned} \rho(\vec{r}) &= \langle \psi | \rho(\vec{r}) | \Psi \rangle \\ &= \sum_{i=1}^N \int \delta(\vec{r} - \vec{r}_i) |\psi(\vec{r}_1, \dots, \vec{r}_N)|^2 d\vec{r}_1 \dots d\vec{r}_N \\ &= \int |\psi(\vec{r}, \vec{r}_2, \vec{r}_3, \dots, \vec{r}_N)|^2 d\vec{r}_2 d\vec{r}_3 \dots d\vec{r}_N + \int |\psi(\vec{r}_1, \vec{r}, \vec{r}_3, \dots, \vec{r}_N)|^2 d\vec{r}_1 d\vec{r}_3 \dots d\vec{r}_N + \dots \\ &= N \int |\psi(\vec{r}, \vec{r}_2, \vec{r}_3, \dots, \vec{r}_N)|^2 d\vec{r}_2 d\vec{r}_3 \dots d\vec{r}_N \end{aligned} \quad (16)$$

where  $\vec{r}_i$  are the variable related to each electron and  $N$  is the total number of electrons. For the first term, the nuclei-electron interaction  $E_{Ne}$  is

$$\hat{V}_{Ne} = - \sum_i^N \sum_A^M \frac{Z_A}{|\vec{r}_i - \vec{R}_A|} \quad (17)$$

Thus, its expectation value is

$$\begin{aligned} E_{Ne} &= \langle \psi(\vec{r}_1, \dots, \vec{r}_N) | \hat{V}_{Ne} | \psi(\vec{r}_1, \dots, \vec{r}_N) \rangle \\ &= - \sum_i^N \sum_A^M \int \psi^*(\vec{r}_1, \dots, \vec{r}_N) \frac{Z_A}{|\vec{r}_i - \vec{R}_A|} \psi(\vec{r}_1, \dots, \vec{r}_N) d\vec{r}_1 \dots d\vec{r}_N \\ &= - \sum_A^M \left[ \int \frac{Z_A}{|\vec{r}_1 - \vec{R}_A|} |\psi(\vec{r}_1, \dots, \vec{r}_N)|^2 d\vec{r}_1 \dots d\vec{r}_N + \int \frac{Z_A}{|\vec{r}_2 - \vec{R}_A|} |\psi(\vec{r}_2, \dots, \vec{r}_N)|^2 d\vec{r}_1 \dots d\vec{r}_N + \dots \right] \\ &= - \sum_A^M \left[ \int \frac{Z_A}{|\vec{r}_1 - \vec{R}_A|} d\vec{r}_1 \int |\psi(\vec{r}_1, \dots, \vec{r}_N)|^2 d\vec{r}_2 d\vec{r}_3 \dots d\vec{r}_N \right. \\ &\quad \left. + \int \frac{Z_A}{|\vec{r}_2 - \vec{R}_A|} d\vec{r}_2 \int |\psi(\vec{r}_2, \dots, \vec{r}_N)|^2 d\vec{r}_1 d\vec{r}_3 \dots d\vec{r}_N + \dots \right] \end{aligned} \quad (18)$$

Given from equation 16, the expectation value becomes

$$\begin{aligned}
E_{Ne} &= -\frac{1}{N} \sum_A^M \left[ \int \frac{Z_A}{|\vec{r}_1 - \vec{R}_A|} \rho(\vec{r}_1) + \int \frac{Z_A}{|\vec{r}_2 - \vec{R}_A|} \rho(\vec{r}_2) + \dots \right] \\
&= -\sum_A^M \left[ \int \frac{Z_A}{|\vec{r}_i - \vec{R}_A|} \rho(\vec{r}_i) d\vec{r} \right] \\
E_{Ne} &= \int \rho(\vec{r}) V_{Ne}(\vec{r}) d\vec{r}
\end{aligned} \tag{19}$$

For the electron-electron interaction  $E_{ee}$ ,

$$E_{ee} = \frac{1}{2} \sum_i^N \sum_{j \neq i}^N \frac{1}{|\vec{r}_i - \vec{r}_j|} \tag{20}$$

However, practically it cannot perform in terms of single-particle density so it has to perform based on the two-particle density as following

$$E_{ee} = \frac{1}{2} \int \int d\vec{r}_1 d\vec{r}_2 \frac{\rho^{(2)}(\vec{r}_1, \vec{r}_2)}{|\vec{r}_1 - \vec{r}_2|} \tag{21}$$

Since many-particle problem is difficult to solve, the two-particle density  $\rho^{(2)}(\vec{r}, \vec{r}')$  is approximated as the combination of one-particle densities and the correction term as follows

$$\rho^{(2)}(\vec{r}_1, \vec{r}_2) = \rho(\vec{r}_1)\rho(\vec{r}_2) + \Delta\rho^{(2)}(\vec{r}_1, \vec{r}_2) \tag{22}$$

As a result, this term eventually becomes

$$E_{ee} = +\frac{1}{2} \int \int \frac{\rho(\vec{r}_1)\rho(\vec{r}_2)}{r_{12}} d\vec{r}_1 d\vec{r}_2 + E_{ncl}[\rho] \tag{23}$$

The second H-K theorem states that the functional provides the lowest energy if and only if the input density is the true ground state density. In other words, electron density  $\rho$  can always be derived from minimizing  $E[\rho]$ . Hence, it ensures that an obtaining density is the ground state density. This is actually similar to the variational principle so the DFT calculation is limited to the ground state only.

#### 4.1.5 The Kohn-Sham approach

Up to now, we can convert all energy terms to be a function of density as shown in equation 15 except for the kinetic term  $T[\rho]$  and non classical term  $E_{ncl}[\rho]$ . Thus, the remaining task is to convert these two terms. In 1965, Kohn and Sham proposed that the kinetic energy term can be calculated using non-interacting frame or the single-particle orbitals which have the same density as the actual interacting reference or full many-particle system as following,

$$\rho_S(\vec{r}) = \sum_i^N \sum_s |\phi_i(\vec{r}, s)|^2 = \rho(\vec{r}) \tag{24}$$

$$T_S = -\frac{1}{2} \sum_i^N \langle \phi_i | \nabla^2 | \phi_i \rangle \tag{25}$$

where  $\phi_i$  is the orbitals of the non-interacting system called Kohn-Sham orbitals. Obviously,  $T_S$  is not the real kinetic energy term so Kohn and Sham clarified that issue by defining the functional  $F[\rho]$  that is,

$$F[\rho] = T_S[\rho] + J[\rho] + EXC[\rho] \tag{26}$$

where  $E_{XC}$  is the exchange-correlation energy containing all unknown terms defined as

$$E_{XC}[\rho] \equiv (T[\rho] - T_S[\rho]) + (E_{ee}[\rho] - J[\rho]) \quad (27)$$

Finally, the total energy can be obtained by

$$E[\rho] = T_S[\rho] + J[\rho] + E_{XC}[\rho] + E_{Ne}[\rho] \quad (28)$$

$$E[\rho] = -\frac{1}{2} \sum_i^N \int d\vec{r} \phi_i^* \nabla^2 \phi_i + \frac{1}{2} \int \int \frac{\rho(\vec{r}_1) \rho(\vec{r}_2)}{r_{12}} d\vec{r}_1 d\vec{r}_2 + \int d\vec{r} \epsilon_{xc}[\rho] \rho(\vec{r}) + \int V_{Ne} \rho(\vec{r}) d\vec{r} \quad (29)$$

When substituting in Schrodinger equation, we call it as Kohn-Sham equation:

$$\left( -\frac{1}{2} \nabla^2 + \int \frac{\rho(\vec{r}_2)}{|r_1 - r_2|} d\vec{r}_2 + V_{XC}(\vec{r}_1) - \sum_A^M \frac{Z_A}{|r_1 - r_A|} \right) \psi_i = \epsilon_i \psi_i$$

$$\left( -\frac{1}{2} \nabla^2 + V_S(\vec{r}_1) \right) \psi_i = \epsilon_i \psi_i \quad (30)$$

where  $V_S(\vec{r}_1)$  is the Kohn-Sham potential. Consequently, the last unknown term is the exchange-correlation term discussed below.

#### 4.1.6 The exchange-correlation function

Theoretically, the interacting electron gas problem can be tackled using the Kohn-Sham equations to obtain its exact ground state energy if we know an exchange-correlation functional  $E_{xc}[\rho(\vec{r})]$ . Nevertheless, the  $E_{xc}[\rho(\vec{r})]$  is still not obvious so an approximation is required for an inhomogeneous interacting electron gas. That is, the exchange-correlation energy for the homogeneous system is approximated to use in the inhomogeneous system as following.

$$E_{xc}^{LDA}[\rho] = \int \rho(\vec{r}) \epsilon_{xc}(\rho(\vec{r})) d\vec{r} \quad (31)$$

where  $E_{xc}[\rho(\vec{r})]$  is the exchange-correlation energy of an uniform electron gas which is now available. This approximation is called the local density approximation (LDA). From equation 31, it indicates that the information depends on the electron density at a considering single point only so an improvement exists. The little supplement is that rather than considering only at one specific single point, we consider the gradient of the charge density. It means that it considers not only one particular point but also neighboring points. This improvement is called generalized gradient approximation (GGA) as shown in equation 32.

$$E_{xc}^{GGA}[\rho] = \int \rho(\vec{r}) \epsilon_{xc}(\rho(\vec{r}), \nabla \rho(\vec{r})) d\vec{r} \quad (32)$$

#### 4.1.7 DFT+U approach

Previously, we discussed Hartree-Fock approximation as shown in equation 10. The second term  $J_{ij}$  or coulomb interaction term has self-interaction calculation behind in case of  $i = j$ . However, this self-interaction is cancelled by the third term or the exchange term  $K_{ij}$ . As a result, Hartree-Fock approximation does not have errors about self-interaction. Compared with DFT framework, this cancellable term is absent so DFT normally cannot remove the electron self-interaction properly. It causes the overestimation of electron-electron repulsion resulting in incorrect delocalization, invalid electronic band gap etc. These errors are much obvious when involving in the strongly correlated atoms such as transition metals because of the presence of d or f shells. Consequently, the concept of solution for this problem is that a Hartree Fock (HF)-like formalism is included at the interactions of electrons localized on the same atomic centers called as the on-site interactions. Moreover, additional term  $E^{dc}$  or double counting term is suggested to correct the energy contribution. Thus, the energy

functional based on DFT+U approach can be expressed as

$$E^{DFT+U}[\rho(r), n_{Ilm\sigma}] = E^{DFT}(\rho) + E^{on-site}[n_{Ilm\sigma}] - E^{dc}[n_{Il\sigma}] \quad (33)$$

where  $E^{DFT}(\rho)$  is the conventional energy attaining from electron density  $\rho(\vec{r})$ ,  $E^{on-site}$  is the energy derived from HF to deal with the on-site interactions of localized electrons. This term relies on the number of electrons occupying on atom  $I$  with angular momentum  $l$ , magnetic number  $m$ , and spin  $\sigma$ . The last term,  $E^{dc}$ , is the double counting term. Finally, Dudarev *et al* [22] proposed the rotationally invariant formulation to express  $E^{on-site}$  and  $E^{dc}$  for the total energy in terms of Coulomb interaction  $U_{ll}$  and exchange interaction  $J_{ll}$ . Therefore, the accuracy of DFT+U framework mostly depends on the values of U and J parameters determined in each particular system.

## 4.2 Electronic Band Structure

Electronic band structure is one of representations for roughly informing the type of materials. It is expressed as an energy along selected high symmetry points ( $E_n(\vec{k})$ ). Such band structure is divided into 2 bands: valence and conduction bands. Band in which electrons are occupied is called valence band. All levels are allowed to occupy until fermi level which is the maximum energy that electrons can occupy. After that it is a zone of forbidden band. However, when electrons are excited, they can hop to another allowed band namely conduction band which electron can freely move. The width of these two bands is called band gap. This band gap can indicate several properties and also type of materials as shown below.

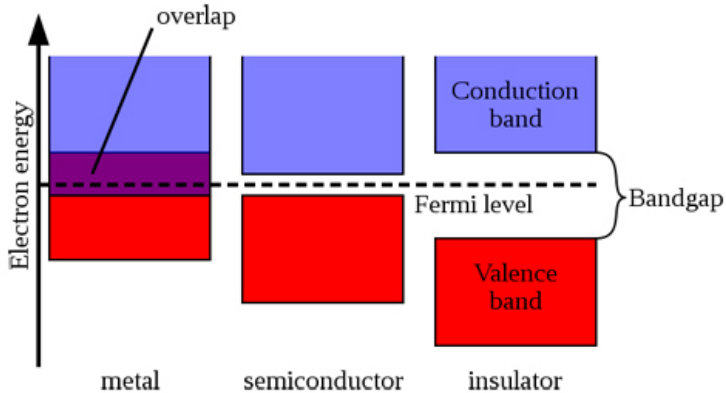


Figure 1: Electronic band structure

For metal, valence band overlaps conduction band which means that metal does not have band gap so electron can be very conductive. Then, if it has some small gap between valence and conduction bands which electron can still hop when excited, that material is semiconductor. Last, if band gap is large until electron cannot hop from valence band to conduction band, that material is insulator.

## 4.3 Density of States (DOS)

The density of states is a numerical parameter informing the states availability at each energy level. It is a function of delta function which means that if some electrons can occupy at some energy level, it causes peak at such energy level. If there is no occupation of electrons, at that energy level the value of density of states is zero. Therefore, density of states will be employed to consider the orbital of each atom and then, we will know what atom is dominant after doping.

## 4.4 Electron and Ion Conductivity Calculation

A device which has ability to store energy and reversibly convert chemical to electrical energy is typically called a rechargeable battery. It is used as solid electrolytes in electrochemical cells and consists of three major components: anode, cathode, and electrolyte as shown in figure 2

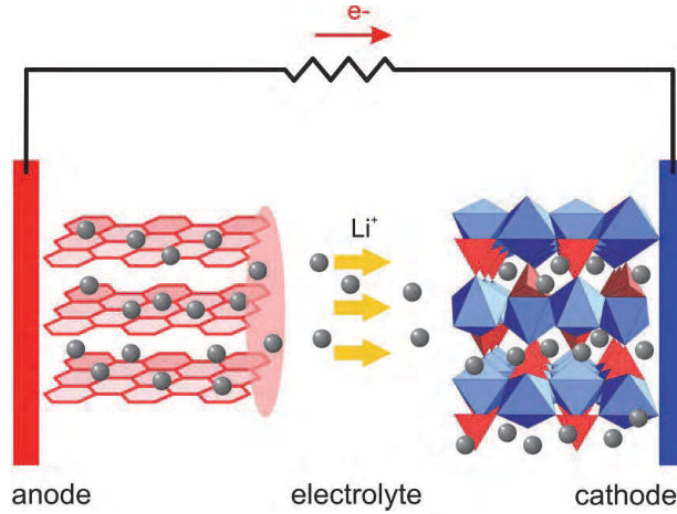
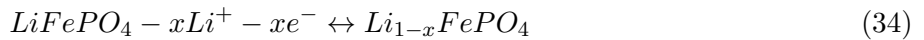
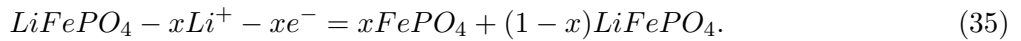


Figure 2: Working mechanism of Li-ion batteries (taken from Ref.[23])

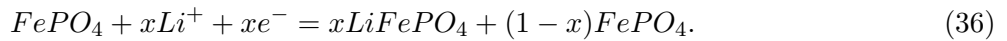
Nowadays, anode is normally made from graphite. However, there are many possible materials making cathode such as  $\text{LiCoO}_2$ ,  $\text{LiMn}_2\text{O}_4$ , and  $\text{LiFePO}_4$ . Due to the outstanding properties of  $\text{LiFePO}_4$  as discussed in the introduction,  $\text{LiFePO}_4$  is chosen for improvement. Generally, the process of battery is described by



Nevertheless,  $\text{LiFePO}_4$  does not proceed like above equation. Work of Molenda [23] reported that  $\text{LiFePO}_4$  actually comprises two phases during activation process. The first phase is  $\text{LiFePO}_4$  lithiation, existing during battery charging. In this phase, a Li ion and an electron are extracted from  $\text{LiFePO}_4$  to  $\text{FePO}_4$  phase as explained in the following equation,



On the other hand, the other phase is  $\text{FePO}_4$  delithiation occurring during battery discharging. In this phase,  $\text{FePO}_4$  obtains the Li ion and electron to form  $\text{LiFePO}_4$ , as shown below



Overall, it can be concluded that  $\text{LiFePO}_4$  battery has two phases and two types of charge carriers. Hence, conductivity in  $\text{LiFePO}_4$  will be improved if the electrons and Li ions, which are relevant, to electronic and ionic conductivity, respectively, are investigated. Both types of conductivity are discussed further below.

### 4.4.1 Electronic Conductivity Mechanism

According to earlier discussion, electron moving through battery is actually the small hole polaron migrating between  $\text{Fe}^{2+}$  and  $\text{Fe}^{3+}$ . In  $\text{LiFePO}_4$  phase, all Fe atoms have charge 2+; however, while it converts to the other phase  $\text{FePO}_4$ ,  $\text{Fe}^{2+}$  will transform to  $\text{Fe}^{3+}$  for charge compensation for disappearing Li atom by extracting one negative charge. Such negative charge exchange causes the localized hole which is actually a quasiparticle. In addition, this migration causes the distortion around the

Fe site which leads to self-trapped state because the carrier always minimizes its energy to localize at the lattice deformation. The quasiparticle with self-induced distortion is hole polaron [24]. As the distortion is in the range of the order of lattice constant, we call it as a small hole polaron [25]. There are three crucial criteria for specifying whether the small hole polaron exists in our structure.

- (i) Magnetic moment at the Fe site: work of Gu *et al* [25] investigated the behaviours of magnetic moments at Fe atoms when an Li atom is slightly extracted to the  $\text{FePO}_4$  phase. They reported that when one Li atom is removed, the magnetic moment of one Fe atom will jump from  $3.76 \mu_B$  to  $4.29 \mu_B$ . Similarly, when two Li atoms are removed, the magnetic moment of two Fe atoms will also jump from  $3.76 \mu_B$  to  $4.29 \mu_B$ , as shown in figure 3. In other words, the  $\text{Fe}^{2+}$  will convert to  $\text{Fe}^{3+}$  one by one when Li atoms are removed.

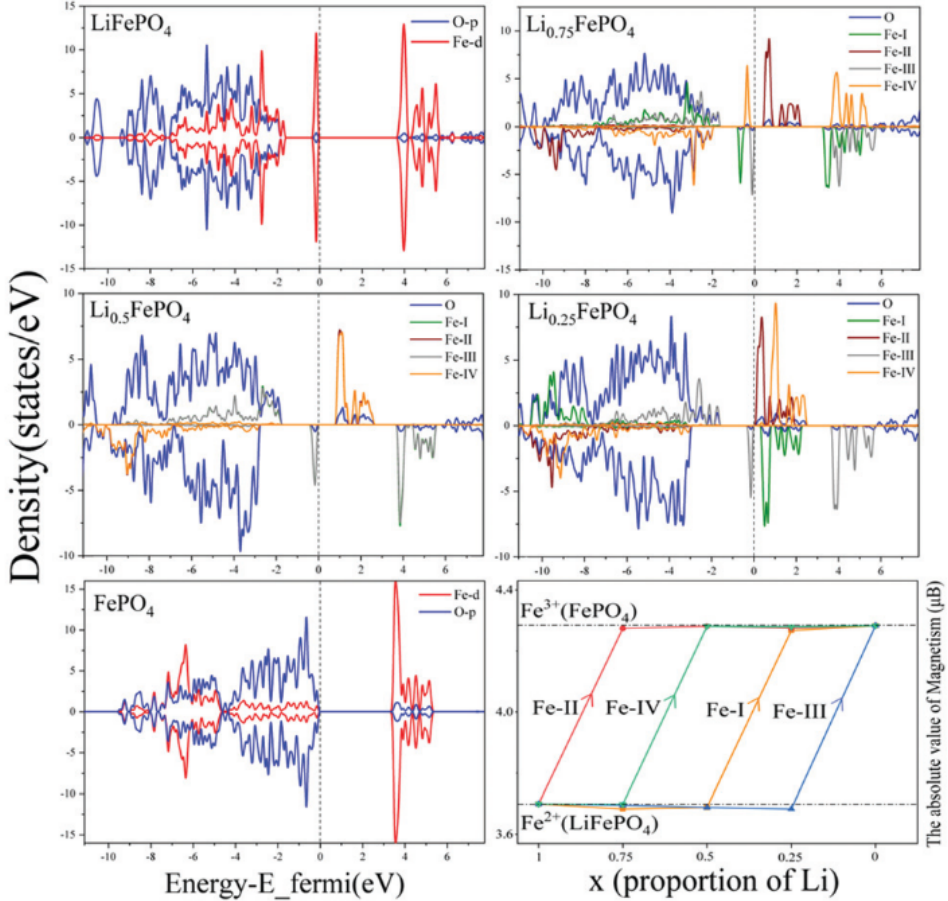


Figure 3: The HSE06 calculated partial density of states (PDOS) of  $\text{Li}_x\text{FePO}_4$  and the absolute value of the calculated magnetic moments of four Fe ions in  $\text{Li}_x\text{FePO}_4$  ( $x = 1, 0.75, 0.5, 0.25, 0$ ). (taken from Ref.[25])

This enhancement of the magnetic moment of the Fe atom indicates that a small hole polaron exists in the interested structure with the same number of  $\text{Fe}^{3+}$  ions. Finally, it can be concluded that for  $\text{LiFePO}_4$  when the polaronic behaviour occurs, or when  $\text{Fe}^{2+}$  converts to  $\text{Fe}^{3+}$ , the magnetic moment of an Fe atom jumps from  $3.7 \mu_B$  to  $4.3 \mu_B$ . This is the unique property occurring only in  $\text{LiFePO}_4$ . For other cathode materials, such as  $\text{Li}_x\text{MnPO}_4$ ,  $\text{Li}_x\text{CoPO}_4$ , and  $\text{Li}_x\text{NiPO}_4$ , their investigation results showed that the magnetic moment at a transition metal atom does not need to jump from an exact value to another exact value. As illustrated in figure 4, when some Li atom is removed, the charge of transition metal atom does not have to convert to the higher charge. It means that the polaronic behaviour sometimes does not exist. This suggests that  $\text{LiFePO}_4$  is the best cathode material with this regard since the polaronic behaviour occurs most easily, which will have a directly positive effect on electronic conductivity.

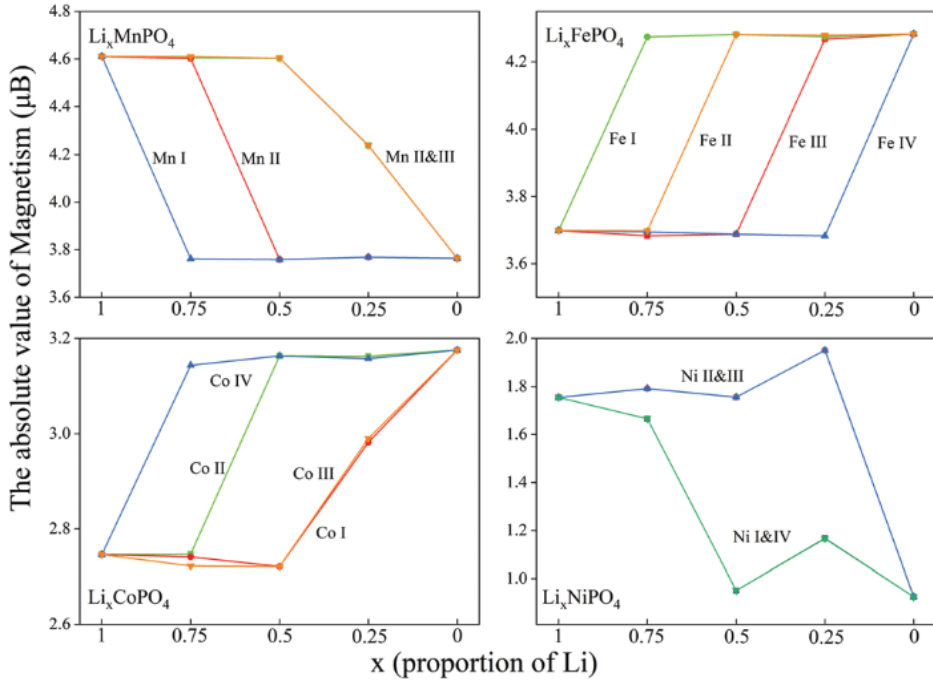


Figure 4: The absolute value of the calculated magnetic moments of four transition metal ions in  $\text{Li}_x\text{MPO}_4$  ( $x = 1, 0.75$ ;  $M = \text{Mn}, \text{Fe}, \text{Co}, \text{Ni}$ ). (taken from Ref.[25])

- (ii) Average Fe-O bond length: another criteria for affirming the presence of a small hole polaron is the Fe-O bond length. Since a small hole polaron results from the lattice distortion, bond length around the Fe site should be varied. Thus, many research groups [20, 24, 26, 27] exploited this variation to indicate the small hole polaron effect. All groups proceeded the same task that is measuring the Fe-O bond length around the Fe site as shown as follows:

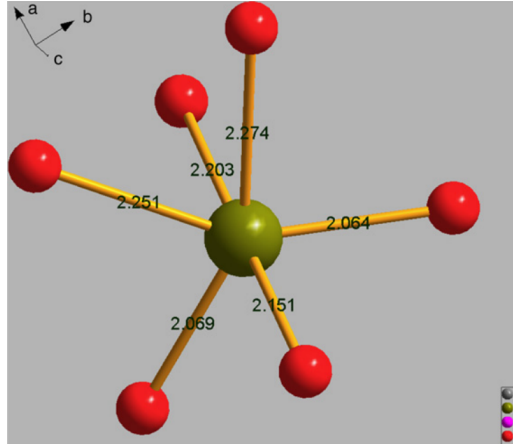


Figure 5: Fe–O octahedral bond length. (taken from Ref. [26])

The  $\text{Fe}^{2+}$  site must have the average bond length about 2.18 Å. The small hole polaron shortens the Fe-O bond length at  $\text{Fe}^{3+}$  site about 2.06 Å.

- (iii) Density of state: The last criteria for determining small hole polaron studied by work of M. Johannes *et al* [24] is the polaron state obviously existed at the conduction band. That is, when small hole polaron is produced, it must have the new state near fermi level at the conduction band which stems from the combination of transition metals with less than 1/3 of total of oxygen state.

#### 4.4.2 Ionic Conductivity Mechanism

Ionic conductivity results from Li ions hopping from the lithiation  $\text{LiFePO}_4$  phase to the delithiation  $\text{FePO}_4$  phase along the  $b$  axis as shown below,

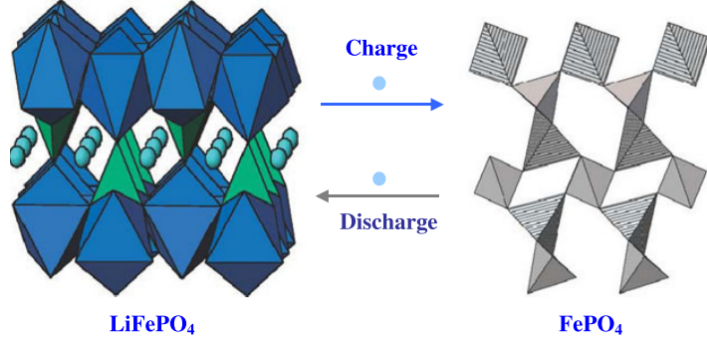


Figure 6: Structure transformation of orthorhombic  $\text{LiFePO}_4$  and  $\text{FePO}_4$  during the charging and discharging process. (taken from Ref.[28])

During delithiation  $\text{FePO}_4$ , the battery is charging so all Li ions already move to anode. However, during lithiation  $\text{LiFePO}_4$  phase, the battery is discharging so Li ion moves from anode to  $\text{LiFePO}_4$  as displayed in figure 7 whereas small hole polaron will migrate from  $\text{Fe}^{2+}$  to  $\text{Fe}^{3+}$  for charge compensation.

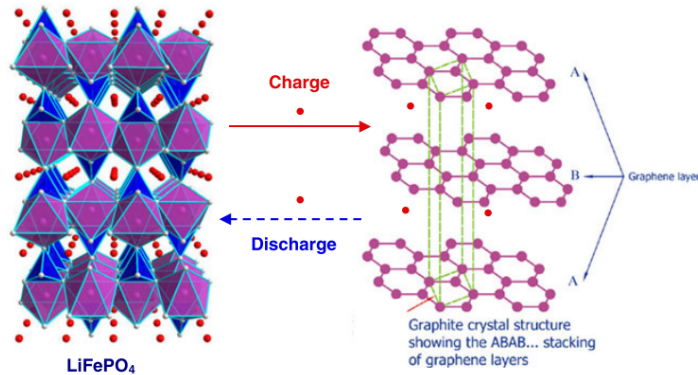


Figure 7: Charge and discharge diagram of  $\text{LiFePO}_4$ /graphite battery. (taken from Ref.[28])

Therefore, the processes between lithiation and delithiation phases ( $\text{Li}_x\text{FePO}_4$ ,  $x = 1, 0.75, 0.5, 0.25, 0$ ) are studied.

#### 4.4.3 Nudge Elastic Band (NEB) Method

After we know the conductivity mechanism existing in the structure, we need to have the method to measure their performance. One of the famous and possible indicators is the Nudge Elastic Band (NEB) method [29, 30, 31]. This is a qualified approach for specifying a lowest energy path often called as "minimum energy path" (MEP) for the reaction or diffusion from one local minimum (initial state) to another one (final state). The maximum point energy along such path is the saddle point energy relevant to the activation energy barrier. It means that if we can take this method to investigate the small hole polaron hopping and  $\text{Li}^+$  hopping, we will be able to exploit energy barrier to compare which path is most efficient. Most crystals contain atoms which are densely packed and are in low temperature compared with the melting temperature so finding minimum energy path (MEP) has to comply with harmonic transition state theory (hTST) which bases on two basic assumptions. First, the rate is so slow that a Boltzmann distribution exists and remains in the reactant state. Second, a diffusion process going from the initial state to the final state has to take place only one way direction

so the main task is to find the saddle points. It is necessary to examine the shape of MEP since it will be able to specify the actual highest saddle point on the energy surface [29].

**4.4.3.1 Chain of state method and Elastic band method** To be able to find MEPs and saddle points, we need to manipulate the chain of state method to produce a set of images (replica) of the system. The number of images from starting and ending states should be about 4-20 images. The chain of state method generates the mimic spring interaction between adjoining images to prevent discontinuity of the path. It is called an elastic band. Previously, the plain elastic band was proposed. The force affecting on image  $i$  is

$$\vec{F}_i = -\nabla V(\vec{R}_i) + \vec{F}_i^s \quad (37)$$

where

$$\vec{F}_i^s = k_{i+1}(\vec{R}_{i+1} - \vec{R}_i) - k_i(\vec{R}_i - \vec{R}_{i-1}) \quad (38)$$

where  $F$  is the force,  $V$  is potential energy, and  $k$  is spring constant. The plain elastic band soon became failure since the algorithm faces the problems about corner cutting and sliding-down as illustrated in figure 8.

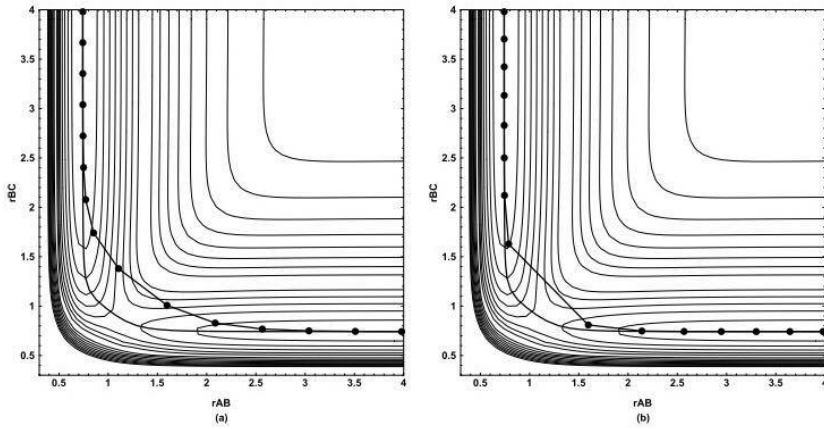


Figure 8: A contour plot of the potential energy surface for a simple test problem where (a)  $k=1$  and (b)  $k=0.1$ . (taken from Ref [29])

The circular dashed line represents the plain elastic band (PEB or EB) method and the solid line represents the nudge elastic band (NEB) method. It is obviously seen that the PEB skips the exact saddle point region which leads to the corner cutting problem. This problem always happens because the spring force acting on the path in parallel direction is so enormous that the perpendicular restoring force cannot subtract. Thus, the images are always driven out of the MEP. In addition, when they tried reducing spring constant as shown in figure 8, the resolution of path is less unbelievable due to the true force  $\nabla V(\vec{R}_i)$  attempting to slide down and escape the saddle points. In other words, it causes too much distance between the incoming and outgoing points near saddle point energy. Thus, it leads to sliding-down effect. As a result, elastic band method always misses the saddle point region.

**4.4.3.2 Nudge elastic band (NEB) method** The failure of the elastic band method is that it considers all associated forces around the image as shown in equation 37. It means that all forces in all components are computed. In order to tackle with these two problems, the nudge elastic band approach has been carried out by projecting these two forces out. That is, the spring force and true force are projected to parallel and perpendicular direction respectively. This projection is called nudge. The related total force affecting an image  $i$  becomes

$$\vec{F}_i^0 = -\nabla V(\vec{R}_i)|_{\perp} + \vec{F}_i^s \cdot \hat{\tau}_{\parallel} \hat{\tau}_{\parallel} \quad (39)$$

where the true force and the spring force are provided by

$$\nabla \vec{V}(\vec{R}_i)|_{\perp} = \nabla \vec{V}(\vec{R}_i) - \nabla \vec{V}(\vec{R}_i) \cdot \hat{\tau}_{\parallel} \hat{\tau}_{\parallel} \quad (40)$$

$$\vec{F}_i^s = k_{i+1}(\vec{R}_{i+1} - \vec{R}_i) - k_i(\vec{R}_i - \vec{R}_{i-1}) \quad (41)$$

where  $\hat{\tau}_{\parallel}$  is the normalized unit tangent to the path. Now, we have force algorithm to optimize the image movement. That is, the relaxed configuration of the images should satisfy  $\nabla \vec{V}(\vec{R}_i)|_{\perp} = 0$ . Practically, the same spacing between each images which defines from equal spring constant is normally set in order to help them converge on MEP more easily. Hence, the images we need to define and fix are only the initial and final states. However, due to this method, images cannot be located at the exact saddle point. It implies that the saddle point energy needs interpolation to obtain.

**4.4.3.3 Climbing image NEB method (CI-NEB)** This is only small improvement from NEB to deal with the problem about finding the exact saddle point. All the processes remain unchanged except for the image at the saddle point. When the saddle point is determined from NEB method, this image is forced by different ways. That is, [30, 31]

$$\vec{F}_{i_{max}}^0 = -\nabla V(\vec{R}_{i_{max}}) + 2\nabla V(\vec{R}_{i_{max}}) \cdot \hat{\tau}_{i_{max}} \hat{\tau}_{i_{max}} \quad (42)$$

The force turns to fully act on this highest energy image. This means that the spring forces do not affect anymore. Furthermore, the spacing of this image needs to be different on each side of the saddle point because an image on one side will be compressed and another side will be spread out in order to approach the highest energy point. The effect of this improvement can be illustrated figure 9 below,

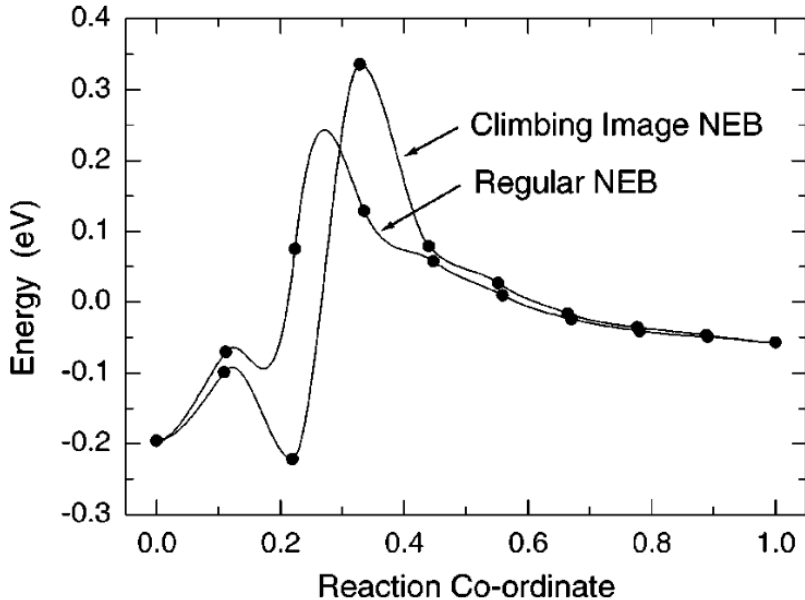


Figure 9: A comparison between NEB and cNEB impremented in DFT calculations of the minimum energy path for CH<sub>4</sub> dissociative adsorption on a Ir(111) surface. (taken from Ref.[30])

**4.4.3.4 Implementation in VASP** To investigate electronic conductivity from small hole polaron hopping and ionic conductivity from Li ion hopping, we can employ NEB method to compute activation energy ( $E_a$ ) of each selected path and then, it will be able to know the diffusion coefficient related to the mobility and conduction of charge carriers which are summarized as follows.

To employ NEB approach, we need to define the initial  $q_A$  and final  $q_B$  configurations. Then, the intermediate paths are linearly generated with the number of images we input in order to obtain the maximum total energy. In this case, suppose that the saddle point is in the  $q_C$  configuration. Hence,

the activation energy can be calculated using [17]

$$E_a = E(q_C) - E(q_A) \quad (43)$$

where  $E_a$  is activation energy,  $E(q_C)$  is the total energy of activated state, and  $E(q_A)$  is the total energy of initial state.

- Small hole polaron hopping investigation [17, 27, 24].

In order to perform migration of small hole polaron between a  $\text{Fe}^{2+}$  site and a  $\text{Fe}^{3+}$  site, the calculation needs to satisfy the Franck-Condon principle and spin conservation so the structure needs performing with an A-type antiferromagnetic configuration. That is, all Fe atoms in the same plane have the aligned spins. Before operating NEB method, the structure first has to remove one electron from  $\text{Fe}^{2+}$  to create  $\text{Fe}^{3+}$  at that site and then, relax this configuration. After that we remove one electron at the adjacent  $\text{Fe}^{2+}$  to create  $\text{Fe}^{3+}$  again and relax as well. The schematic view of small hole polaron hopping is shown in figure 10. Now we have two configurations with different  $\text{Fe}^{3+}$  sites. The intermediate paths along these 2 fixed position are linearly generated [24].

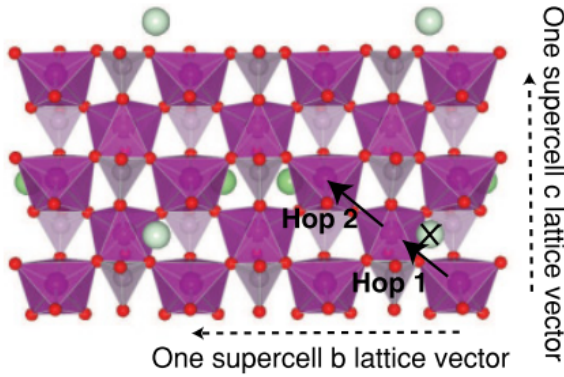


Figure 10: A migration path of small hole polaron hopping from  $\text{Fe}^{3+}$  to another  $\text{Fe}^{3+}$  site. The marked atom is Lithium. (taken from Ref.[27])

According to work of Maxish *et al* [17], they investigated the migration of two adjacent Fe ion sites. The results indicated that this small hole polaron uses the activation energy about 215 meV for migration as shown in figure 11,

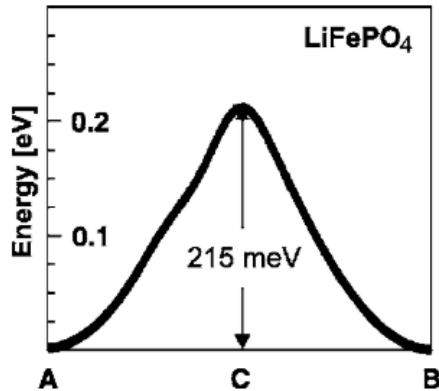


Figure 11: Total energy along polaron migration path between two adjacent Fe site. A, B, and C indicate the configurational coordinates  $q_A$ ,  $q_B$ , and  $q_C$ , respectively. (taken from Ref.[17])

- Li ion hopping investigation

For Li ion hopping, almost all of the tasks are consistent with small hole polaron investigation except for migration paths. According to work of Lin [32], Li ion normally migrates along b-axis. They studied the effect of Vanadium on ionic conductivity. The results indicated that V-doping can improve conductivity as it reduces the energy barrier of Li hopping as shown in figure 12.

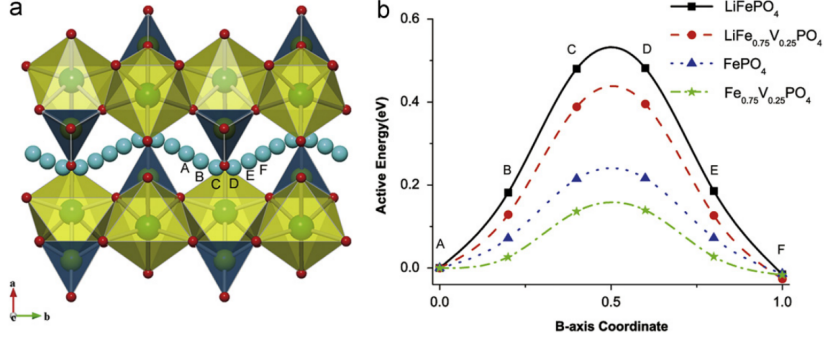


Figure 12: Minimum energy path of Li diffusing along the tunnel of b axis in pure and doped  $\text{LiFePO}_4$  of fully lithiated and fully de-lithiated phases. (taken from Ref.[32])

- Diffusion coefficient and mobility

After we attain the activation energy, we can calculate the diffusion coefficient using [33]

$$D = a^2 \nu \exp\left\{-\frac{E_a}{k_B T}\right\} \quad (44)$$

where D is diffusion coefficient,  $\nu$  is frequency ( $10^{13}$  Hz), a is hopping distance, and T is temperature (300 K). In addition, we also calculate the mobility of charge carrier using Einstein relation [34].

$$\mu = \frac{eD}{k_B T} \quad (45)$$

#### 4.5 Formation energy

Formation energy is the energy the system requires to produce the crystal. It can be calculated as follows [35, 36]):

- In the case of supervalent cation doping

$$E_{formation} = E(\text{Li}_{1-(n-2)x}M_x^{n+}\text{Fe}_{1-x}\text{PO}_4) - [E(\text{Li}_{1-(n-2)x}\text{FePO}_4) - xE(\text{Fe}) + xE(M)] \quad (46)$$

- In the case of Li deficient environment

$$E_{formation} = E(\text{Li}_{1-(n-2)x-a}\text{M}_x^{n+}\text{Fe}_{1-x}\text{PO}_4) - [E(\text{Li}_{1-(n-2)x}\text{M}_x^{n+}\text{Fe}_{1-x}\text{PO}_4) - aE(\text{Li})] \quad (47)$$

where  $M^{n+}$  is dopant.

As expressed in equation, we can apply formation energy to investigate the structure stability after the pure crystal is perturbed. If formation energy provides negative value, it indicates that the crystal doped with other impurities is stable.

## 5 Objectives

In this research we aim to investigate several various structures doped with supervalent cations and lithium vacancies and achieve the following objectives

- 5.1 To study electronic structure of LiFePO<sub>4</sub> doped with combined supervalent cations and lithium ion vacancies
- 5.2 To compare and study effect of combined supervalent cations and lithium ion vacancies doping on ionic and electronic conductivities
- 5.3 To compare energy barrier of charge carriers doped with different dopants

## 6 Methodology

This research work comprises two main parts: (i) implementation of computational codes in Vienna ab initio simulation package (VASP) [37, 38, 39] to simulate the electronic structures, which includes investigation of conductivity improvement. All simulated results are performed using Python code and then compared with the experimental results, and (ii) the theoretical work to develop the indicator for analyzing the simulation data and extract it efficiently.

### 6.1 Computational Work

I plan to study all relevant knowledge such as parameters in VASP and Python to simulate the electronic structures and perform the results respectively.

All density functional theory (DFT) calculations were implemented using VASP program within a plane wave basis set and a projector augmented wave (PAW) [40] framework. It is acceptable that transition metals always give the underestimate band gap if employed under the generalized gradient approximation (GGA) [41]. In order to avoid such considerable self-interaction errors, the GGA+U approach proposed by Dudarev *et al* [22] was adopted to deal with the d orbitals by adding the onsite coulomb interaction term U and the exchange term J into the system. These two extra terms can be combined into an effective interaction parameter  $U_{eff} = U - J$  according to Dudarev approach. In this work, the correction term  $U_{eff} = 4.3, 4.0, 2.0$ , and  $2.0$  eV for Fe, Zr, Ti, and Nb respectively [42, 43, 44, 45] were applied.

Calculation of unit cell applied a  $3 \times 4 \times 5$  Monkhorst–Pack  $k$ -point [46] sampling over the first Brillouin zone, a plane-wave basis-set cutoff setting at 550 eV, the total energy convergence at  $10^{-5}$ , and Gaussian smearing with 0.03 eV width. All of these values are higher than the values reported from other literatures [42, 44] to obtain reliable results which will be discussed in section 7.1.1. In addition, the denser kpoint ( $5 \times 7 \times 11$ ) and tetrahedra method were applied for DOS calculation. For doped LiFePO<sub>4</sub>, a  $1 \times 2 \times 2$  supercell (112 atoms) with a  $2 \times 2 \times 2k$ -point mesh was used to dilute dopants at least 6.25% doping. In order to save the computational resources, the energy cutoff and total energy convergence were reduced to 500 eV and  $10^{-4}$  according to Hoang’s work [20]. The gaussian smearing with 0.05 eV width was applied. For DOS calculation, we operated Gamma-centered  $k$ -point at  $4 \times 4 \times 4$ . For all relaxed structure optimizations within the conjugate gradient algorithm framework, the ionic positions and cell parameters were optimized until the residual force was less than 0.01 eV Å<sup>-1</sup>. The ground state antiferromagnetic (AFM) spin configuration were assumed for all calculations to correspond with the behaviors in low temperature reported in the experiment [47]. For the climbing nudge elastic band (cNEB) calculation, 5 intermediate images are used to obtain accurate energy barrier.

### 6.2 Theoretical Work

In this research, LiFePO<sub>4</sub> is investigated based on some motivations as follows:

1. In LiFePO<sub>4</sub>, electronic conductivity results from hopping of small hole polaron ( $p^+$ ) between Fe<sup>2+</sup> and Fe<sup>3+</sup> so electronic conductivity depends on the number of  $p^+$ . As a result, doping with extra  $p^+$  by producing lithium vacancy ( $V_{Li}^-$ ) should improve electronic conductivity. In other words, doping in Li deficient environment should enhance the number of  $p^+$  and subsequently improve electronic conductivity.

2. In LiFePO<sub>4</sub>, ionic conductivity results from the number of lithium vacancy ( $V_{Li}^-$ ) so the presence of  $V_{Li}^-$  should improve ionic conductivity
3. For total conductivities, it is necessary to consider both p<sup>+</sup> and  $V_{Li}^-$  so the situation that p<sup>+</sup> and  $V_{Li}^-$  exist at the same time should be investigated
4. Doping with Al<sup>3+</sup>, Ti<sup>4+</sup>, Zr<sup>4+</sup>, and Nb<sup>5+</sup> can improve ionic conductivity since those dopants increase the number of  $V_{Li}^-$ . However, they obstruct the electronic conductivity efficiency because of the lower number of p<sup>+</sup>

Consequently, the scope of this research focuses on doping with Al<sup>3+</sup>, Ti<sup>4+</sup>, Zr<sup>4+</sup>, and Nb<sup>5+</sup> at Fe site which will improve ionic conductivity and also create extra small hole polaron at the same time to improve electronic conductivity by doping in Li-deficient environment so we can express the chemical equation as  $Li_{1-(n-2)x-a}M_x^{n+}(Fe_{1-x-a}^{2+}/Fe_a^{3+})[PO_4]$  where M is dopant and a is ratio of removing Li<sup>+</sup> or increasing Fe<sup>3+</sup>. After each simulation is completed, the data is extracted through lattice parameters, electronic band structure, density of states, and projected density of states to consider the variation of electronic structure from those effects. Then, we apply NEB approach to study energy barrier of  $V_{Li}^-$  and p<sup>+</sup> hoppings of each case so we subsequently compare them and compute diffusion coefficient and mobility which are the main factors for conductivity. All of work can be summarized as shown below,

**Hypothesis:**

Doping with combined lithium vacancy ( $V_{Li}^-$ ) and supervalent cation at Fe site ( $Al_{Fe}^+$ ,  $Ti_{Fe}^{2+}$ ,  $Zr_{Fe}^{2+}$ , and  $Nb_{Fe}^{3+}$ ) in  $LiFePO_4$  structure can enhance the number of  $V_{Li}^-$  and  $p^+$  which results in the improvement of both ionic and electronic conductivities.

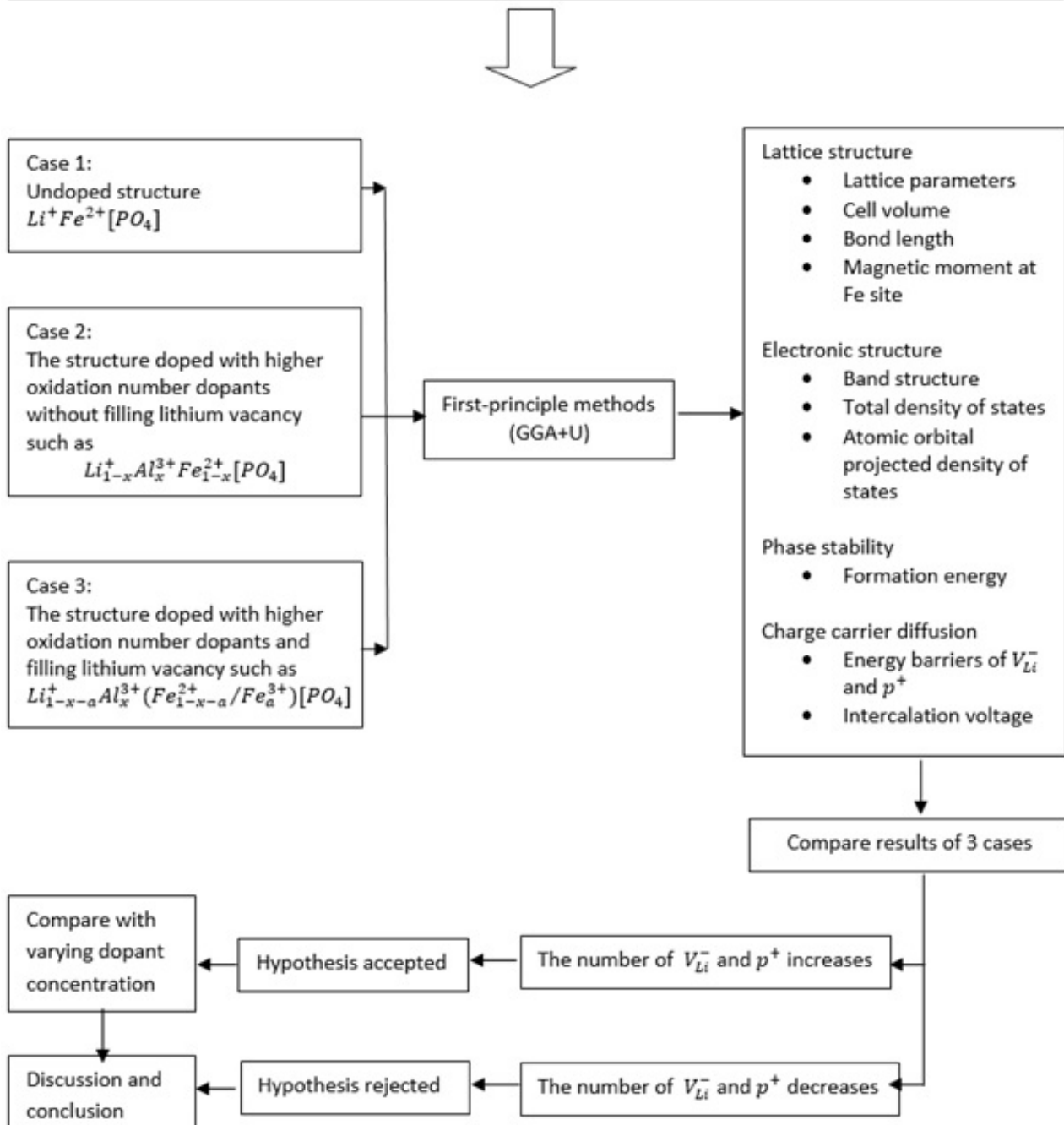


Figure 13: Scope of this work.

After all above works are completed, I will conclude the relation between supervalent doping and Li deficient environment in order to know what solution is the best for improving  $LiFePO_4$  battery.

## 7 Preliminary Results

### 7.1 Parameter optimization for simulation

$\text{LiFePO}_4$  is in orthorhombic Pnma 62 space group and consists of 28 atoms/unit cell. The database of all atomic positions can be extracted from Materials project available in online resources [48]. In order to obtain the accurate and reliable results, we first investigate the convergence validations of cutoff energy and k-point sampling.

#### 7.1.1 Convergence Test

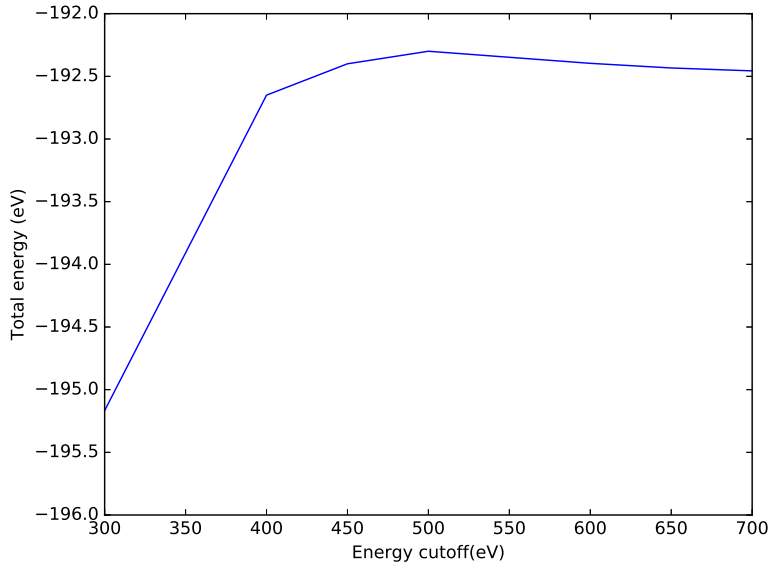


Figure 14: Convergence test of cutoff energy using  $2 \times 2 \times 2$  Monkhorst–Pack  $k$ -point sampling.

As shown in figure 14, the cutoff energy starts approaching some values at 500 eV. However, we choose cutoff energy at 550 eV to ensure the total energy convergence. Then, we investigate  $k$ -point sampling with the same case as shown in figure 15. The result indicates that  $3 \times 3 \times 3$  seems sufficient. To confirm that we use enough dense  $k$ -point,  $3 \times 4 \times 5$   $k$ -point sampling was used.

#### 7.1.2 Lattice parameter optimizations

Before we carry on further simulations, we need to verify our data extracted from database by expanding and shortening the lattice parameters with scaling factor as shown in figure 16. For scaling factor 1, it is the data from database. Then, we expand the volume by increasing scaling factor to be greater than 1 and also shorten the volume by reducing the factor to be less than 1. The graph proves that our atomic positions at scaling factor 1 are the most stable configuration due to its lowest total energy. Thus, our atomic position data is accurate enough for further simulations.

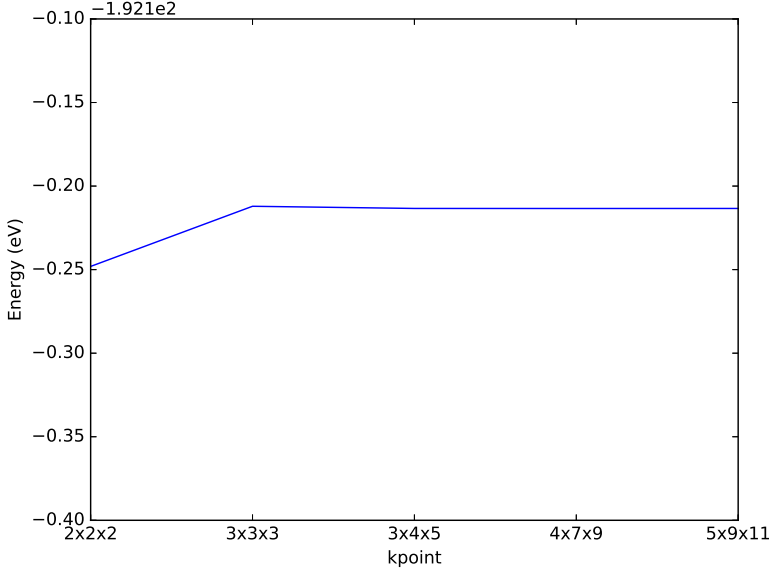


Figure 15: Convergence test of  $k$ -point sampling using energy cutoff at 550 eV.

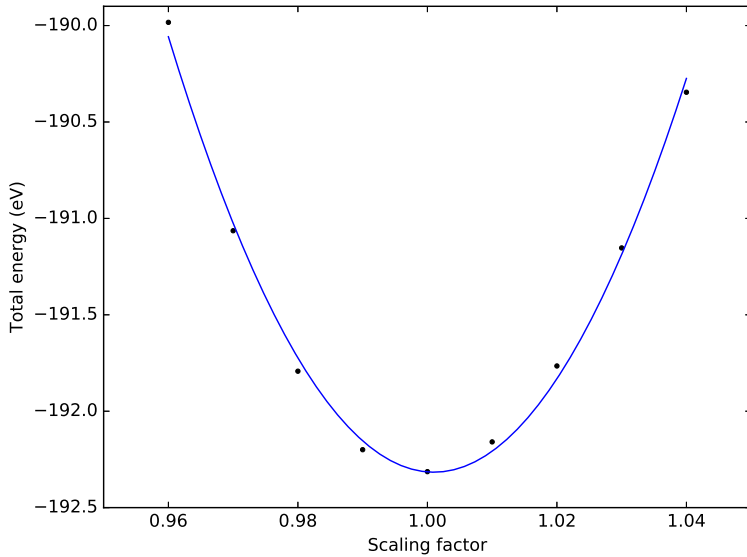


Figure 16: Lattice parameter optimization.

## 7.2 Relaxed structure of LiFePO<sub>4</sub> and FePO<sub>4</sub>

After we gain the appropriate parameters for making results accurate, we now investigate the lattice parameters, magnetic moment, electronic band structure, and density of state and compare with the experimental results as follows.

### 7.2.1 Lattice parameters and Magnetic moments of LiFePO<sub>4</sub>

As shown in table 1, although all simulated results overestimate the lattice parameters when compared with experiments, the volumes of unit cell are just 3.01% for FM and 0.20% for AFM larger than experiments in average. This confirms that our calculated results are in acceptable range with experiments and also consistent in good agreement with other simulated results. Turning to consider magnetic moment at Fe sites, the plus and minus signs represent the direction of spin. Our

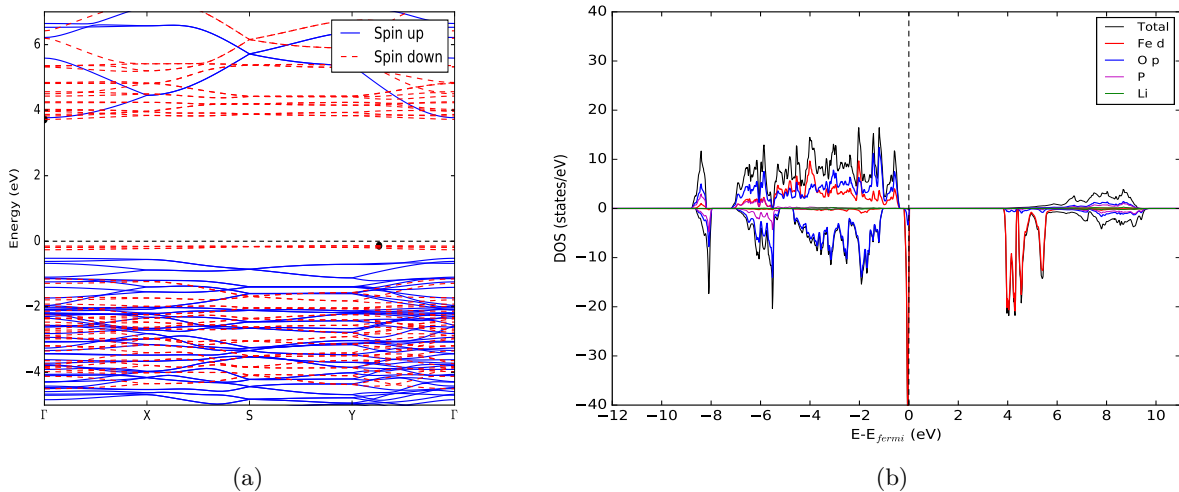
Table 1: Calculated values of optimized LiFePO<sub>4</sub> structure

Lattice parameters (Å)	Simulations				Experiments		
	Ours (FM)	Ref.[49] (FM)	Ours (AFM)	Ref [25] (AFM)	Ref.[50]	Ref.[15]	Ref.[51]
a	10.42232	10.3377	10.4159	10.457	10.3470(0)	10.318(1)	10.3052(1)
b	6.06552	6.0112	6.0622	6.083	6.0189(0)	6.004(1)	5.9946(1)
c	4.74604	4.742	4.7450	4.749	4.7039(0)	4.694(1)	4.6833(1)
volume (Å <sup>3</sup> )	300.029	293.76	299.61	302.08	292.95(5)	290.762(5)	289.32(1)
Magnetic moment							
1 <sup>st</sup> Fe site	3.785	3.74	-3.774	-3.7	-	-	-
2 <sup>nd</sup> Fe site	3.785	3.74	3.774	3.7	-	-	-
3 <sup>rd</sup> Fe site	3.785	3.74	3.774	3.7	-	-	-
4 <sup>th</sup> Fe site	3.785	3.74	-3.774	-3.7	-	-	-
Band gap (eV)	3.836	3.70	3.802	3.76	3.84	3.8	3.8
Fermi level (eV)	2.899		2.956		(Ref.[19])	(Ref.[16])	(Ref.[52])

calculated values are also in good agreement with other simulations although there is no experimental data measuring magnetic moment at zero temperature (0 K). In practice, there is only one experiment group [47] measuring the magnetic moment at 2 K. They reported that the magnetic moment at Fe sites is around  $\pm 4.19(5)\mu_B$ . Finally, our calculated band gap with GGA+U approach [22] provides the consistent value with only 0.24% error when compared with experiments. Therefore, we then investigate electronic structure and density of state as following.

### 7.2.2 Electronic structure and Density of states (DOS) of FM and AFM configurations

Since LiFePO<sub>4</sub> has 2 possible magnetic states: Ferromagnetic(FM) and Antiferromagnetic (AFM), we need to investigate the electronic structure and DOS in order to know which atom is the primary electronic character around fermi level and then we will be able to determine the appropriate magnetic state for further studies.


 Figure 17: (17a) band structure and (17b) DOS of ferromagnetic LiFePO<sub>4</sub>

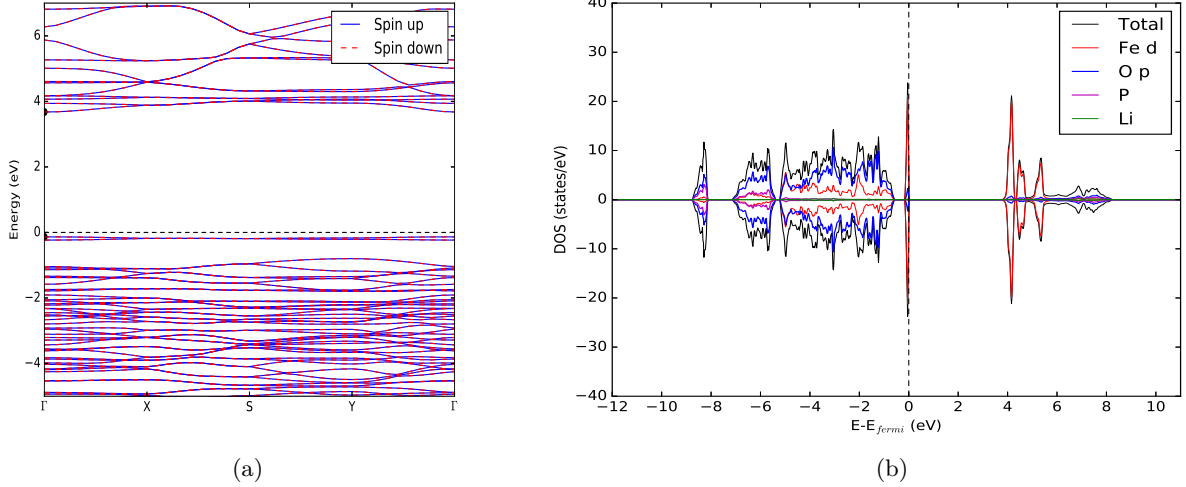


Figure 18: (18a) band structure and (18b) DOS of antiferromagnetic LiFePO<sub>4</sub>

It can be seen from figure 17 and 18 that LiFePO<sub>4</sub> has band gap about 3.8 eV with Fe 3d orbital acting as the dominant contributor near valence band maximum (VBM) and conduction band minimum (CBM), following with O 2p orbital which is a minor contributor. All of which are in satisfied agreement with other works [21, 33]. This large band gap causes the poor electronic conductivity [33]. Therefore, if we can reduce the band gap, electronic conductivity by hopping of small hole polaron will be improved. In addition, although electronic structures of FM and AFM configurations are not different, AFM configuration is the better choice for further studies in doping because LiFePO<sub>4</sub> naturally prefers antiferromagnetic behavior at low temperature (2K) as reported in experiment [47].

### 7.2.3 Electronic structure of FePO<sub>4</sub>

As mentioned before, LiFePO<sub>4</sub> has 2 phases: lithiation and delithiation. Therefore, it is also necessary to study the electronic structure of this phase. This is the result,

Table 2: Calculated values of FePO<sub>4</sub> in AFM configuration

Lattice parameters (Å)	Simulation		Experiment	
	Ours	Ref.[53]	Ref.[53]	Ref.[54]
a	9.93234	9.9807	9.7599	9.8142
b	5.88321	5.8941	5.7519	5.7893
c	4.85883	4.8693	4.7560	4.7820
volume (Å <sup>3</sup> )	283.921	281.46	266.99	271.70
Magnetic moment	Ref.[25]			
1 <sup>st</sup> Fe site	-4.306	-4.3	-	-
2 <sup>nd</sup> Fe site	4.306	4.3	-	-
3 <sup>rd</sup> Fe site	4.305	4.3	-	-
4 <sup>th</sup> Fe site	-4.305	-4.3	-	-
Band gap (eV)	2.431	2.1 Ref[16]	-	-

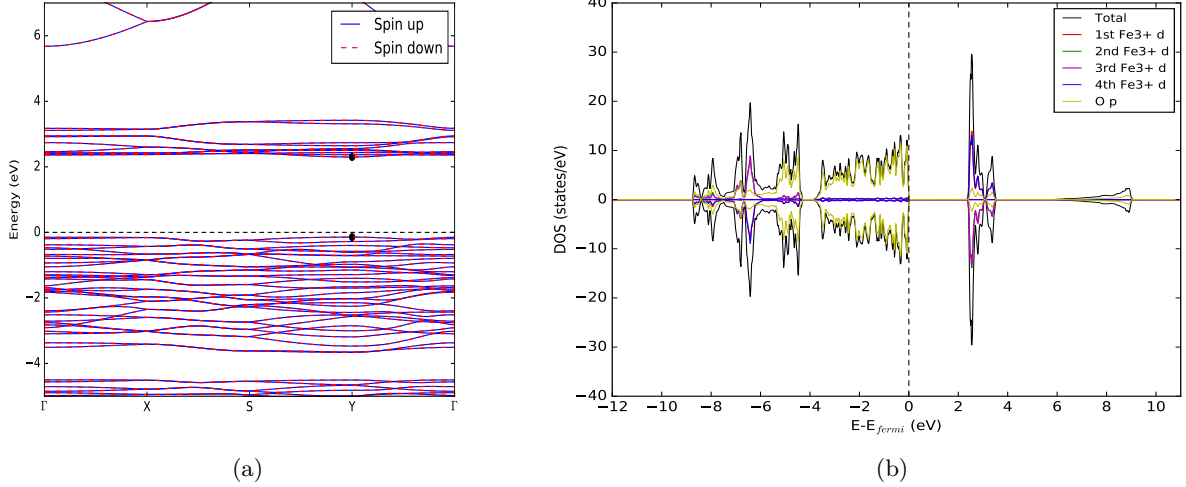


Figure 19: (19a) band structure and (19b) DOS of antiferromagnetic FePO<sub>4</sub>

The results indicate that unit cell volume is less than LiFePO<sub>4</sub> since this phase Li atoms are all vanished. Furthermore, all Fe ions here are Fe<sup>3+</sup> as shown in magnetic moment of table 2. It causes the obvious peak at VBM completely vanishes and all shifts to CBM so the dominant atoms in VBM and CBM are O<sup>2-</sup> p orbital and Fe<sup>3+</sup> d orbital. In other words, small hole polaron does not localize around these Fe<sup>3+</sup> atoms since this phase is also stable like lithiation phase. Therefore, distortion cannot occur and then, small hole polaron cannot exist. Due to the absence of small hole polaron, the band gap is around 2.431 eV.

### 7.3 Effect of Lithium configuration on the band gap

This study focuses on whether Li configuration has an effect on electronic structure. In order to do so, the system is doped under Li-deficient condition with all possible Li configurations. In this case, we use Aluminium (Al<sup>3+</sup>) as the representative dopant substituted at fixed Fe site. After that all results from all configurations are compared. As discussed earlier, doping with Al<sup>3+</sup> can be proceeded via this chemical equation  $Li_{1-x-a}^+Al_x^{3+}(Fe_{1-x-a}^{2+}/Fe_a^{3+})[PO_4]$ . Thus, an Al atom is substituted at Fe site and then, 2 Li atoms are removed in 4 study cases. Since a LiFePO<sub>4</sub> unit cell comprises of 4 Li configurations, we can categorize the removed Li positions as 1-2, 1-3, 1-4, 2-3, 2-4, and 3-4 where 1, 2, 3, 4 represent the position of Li atom as shown below,

After the position of 2 Li vacancies ( $V_{Li}$ ) are differently removed, this is the results.

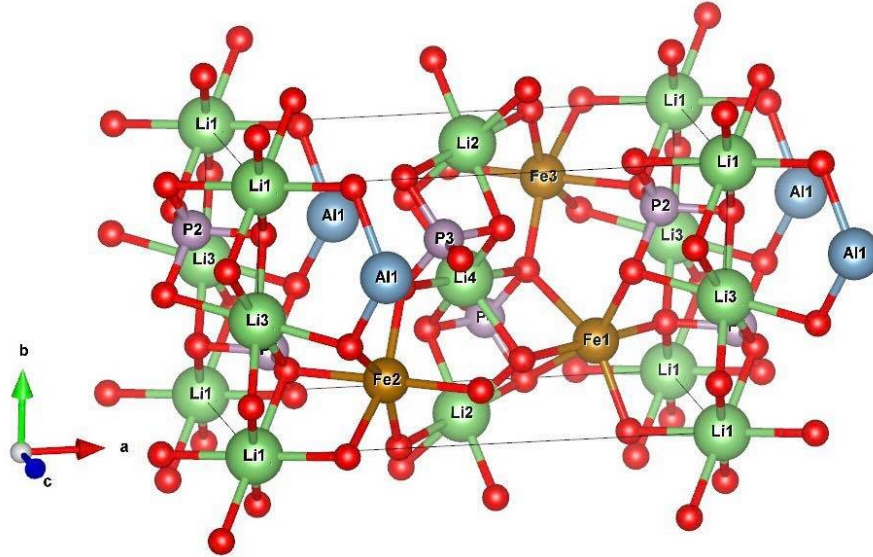


Figure 20:  $Li_2AlFe_3P_4O_{16}$  structure.

Table 3: Calculated values of  $Li_2AlFe_3P_4O_{16}$  structure

Lattice parameters (Å)	Position of 2 Li atoms removed					
	Li1-Li2	Li1-Li3	Li1-Li4	Li2-Li3	Li2-Li4	Li3-Li4
a	10.0688	10.0479	10.0606	10.0606	10.0241	10.0684
b	5.9097	5.8819	5.8997	5.8997	5.9288	5.9099
c	4.8196	4.7902	4.8148	4.8148	4.7946	4.8197
volume (Å³)	286.7549	283.0734	285.7552	285.7531	284.7925	286.7651
Magnetic moment						
1 <sup>st</sup> Al site	0.002	0.002	0.002	0.002	0.002	0.002
1 <sup>st</sup> Fe site	3.754	-4.273	3.755	3.755	3.746	3.754
2 <sup>nd</sup> Fe site	3.776	3.779	3.776	3.776	3.772	3.776
3 <sup>rd</sup> Fe site	-4.298	-3.753	-4.299	-4.299	-4.267	-4.298
Fe-O bond length(Å)*						
1 <sup>st</sup> Al site	1.98	1.99	1.97	1.97	1.96	1.93
1 <sup>st</sup> Fe site	2.15	2.09	2.15	2.15	2.13	2.15
2 <sup>nd</sup> Fe site	2.16	2.15	2.16	2.16	2.20	2.16
3 <sup>rd</sup> Fe site	2.06	2.14	2.06	2.06	2.09	2.06
Band gap (eV)	1.188	1.026	1.188	1.188	0.774	1.188
Total energy (eV)	-182.871	-182.011	-182.847	-182.847	-182.375	-182.871
Symmetry	P1	P1m1	P1	P1	P1m1	P1

\*Average value

From table 3, all lattice parameters and volumes of all Li configurations are not different. It means that the difference of removing Li atoms does not affect them. When considering the magnetic moment, all cases are in the same trend. That is, as small hole polaron results from distortion with neighbors around the Fe site, this causes jumping of the magnetic moment from around  $3.7\mu_B$  for  $Fe^{2+}$  to  $4.3\mu_B$  for  $Fe^{3+}$  [20, 25]. It also corresponds to the average Fe-O bond length which is actually another criteria. Because of distortion around Fe neighbors, Fe-O bond length reduces from about 2.16 Å for  $Fe^{2+}$  to 2.06 Å for  $Fe^{3+}$  [20]. Thus, when 2 Li atoms are removed, some  $Fe^{2+}$  site is distorted and becomes  $Fe^{3+}$  as highlighted. This result has a direct effect on band gap which leads to 2 groups categorized by the band gap energy. For the first group consisting of Li1-2, Li1-4, Li2-3, and Li3-4, they have band gap about 1.188 eV. but the second group comprising of Li1-3 and Li2-4 has

lower energy band gap. We found that this different band gap can actually classified by symmetry. In addition, as the total energy can roughly indicate which configuration is more stable, P1 or no symmetry which has lower energy than P1m1 symmetry has more chance to occur in practice. In conclusion, Li configuration has an effect on the electronic structure so we should take it into account before implementing further studies.

## 7.4 Effect of supervalent cations and Lithium vacancies on LiFePO<sub>4</sub> electronic structure in unit cell

This study concentrates on how each dopant and Lithium vacancy affect the electronic structure under Li deficient condition as expressed as  $\text{Li}_{1-(n-2)x-a}^+ \text{M}_x^{n+} (\text{Fe}_{1-x-a}^{2+}/\text{Fe}_a^{3+})[\text{PO}_4]$  where x is the amount of dopant that substitutes at the Fe<sup>2+</sup> site, n is oxidation number, and a is the proportion of additional V<sub>Li</sub><sup>-</sup> (or removal Li<sup>+</sup>). In this study, we set x at 0.25 (dope 25%) and vary a as much as possible in order to initially study the tendency of each case. After that doping with 6.25% and 12.5% will be implemented in 1 × 2 × 2 supercell later.

### 7.4.1 Effect of Magnesium (Mg<sup>2+</sup>) on electronic structure

Normally, oxidation number of Mg is +2 so doping with charge compensation has to satisfy this chemical equation:  $\text{Li}_{1-a}^+ \text{Mg}_{0.25}^{2+} (\text{Fe}_{0.75-a}^{2+}/\text{Fe}_a^{3+})[\text{PO}_4]$ . Hence, in this case a can be 0 (0V<sub>Li</sub><sup>-</sup>), 0.25 (1V<sub>Li</sub><sup>-</sup>), 0.50 (2V<sub>Li</sub><sup>-</sup>), and 0.75 (3V<sub>Li</sub><sup>-</sup>) only.

Table 4: Calculated values of Mg doping

Lattice parameters (Å)	EXP <sup>1</sup>	SIM <sup>2</sup>	This work			
	Ref.[50]	Ref.[35]	0V <sub>Li</sub> <sup>-</sup>	1V <sub>Li</sub> <sup>-</sup>	2V <sub>Li</sub> <sup>-</sup>	3V <sub>Li</sub> <sup>-</sup>
a	10.3327(1)	10.247	10.3660	10.1709	10.1646	10.0267
b	6.0060(4)	6.026	6.0400	5.9163	5.9504	5.8988
c	4.6932(0)	4.723	4.7427	4.7037	4.8108	4.8430
volume (Å <sup>3</sup> )	-	-	296.9396	283.0147	290.9566	286.3978
Magnetic moment						
1 <sup>st</sup> Mg site	-	-	0.001	0.003	0.002	0.002
1 <sup>st</sup> Fe site	-	-	3.774	3.773	3.761	4.3
2 <sup>nd</sup> Fe site	-	-	3.779	4.301	4.314	4.32
3 <sup>rd</sup> Fe site	-	-	-3.773	-3.762	-4.299	-4.286
Fe-O bond length(Å)*						
1 <sup>st</sup> Mg site	-	2.133	2.13	2.08	2.12	2.11
1 <sup>st</sup> Fe site	-	2.176	2.17	2.14	2.16	2.05
2 <sup>nd</sup> Fe site	-	2.176	2.17	2.06	2.06	2.06
3 <sup>rd</sup> Fe site	-	2.176	2.18	2.15	2.09	2.06
Band gap (eV)	-	-	3.854	0.846	1.297	1.891

\*Average value

<sup>1</sup> Experiment 2% doping

<sup>2</sup> Simulation 6.25% doping

The electronic structure and density of state in each case can be seen below,

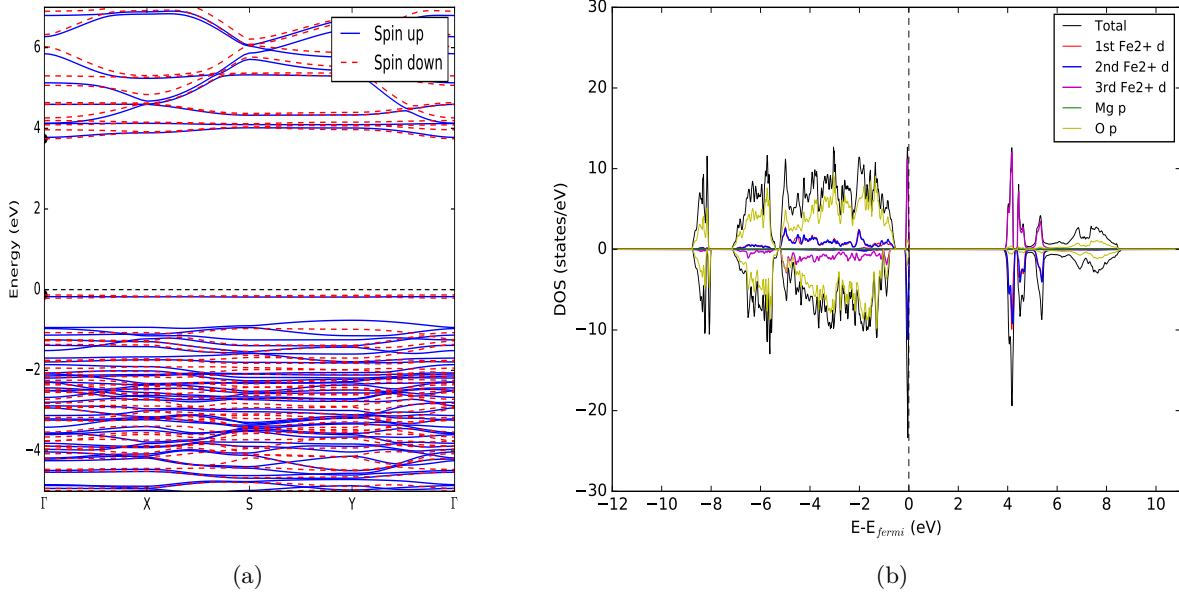


Figure 21: (21a) band structure and (21b) DOS of  $0V_{Li}^-$

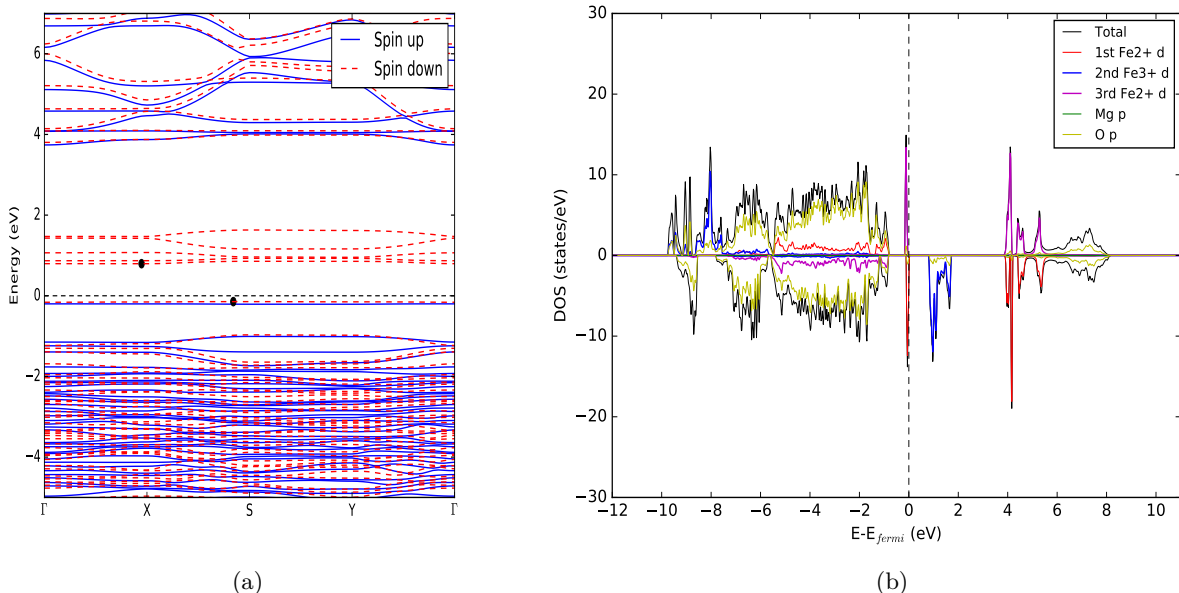


Figure 22: (22a) band structure and (22b) DOS of  $1V_{Li}^-$

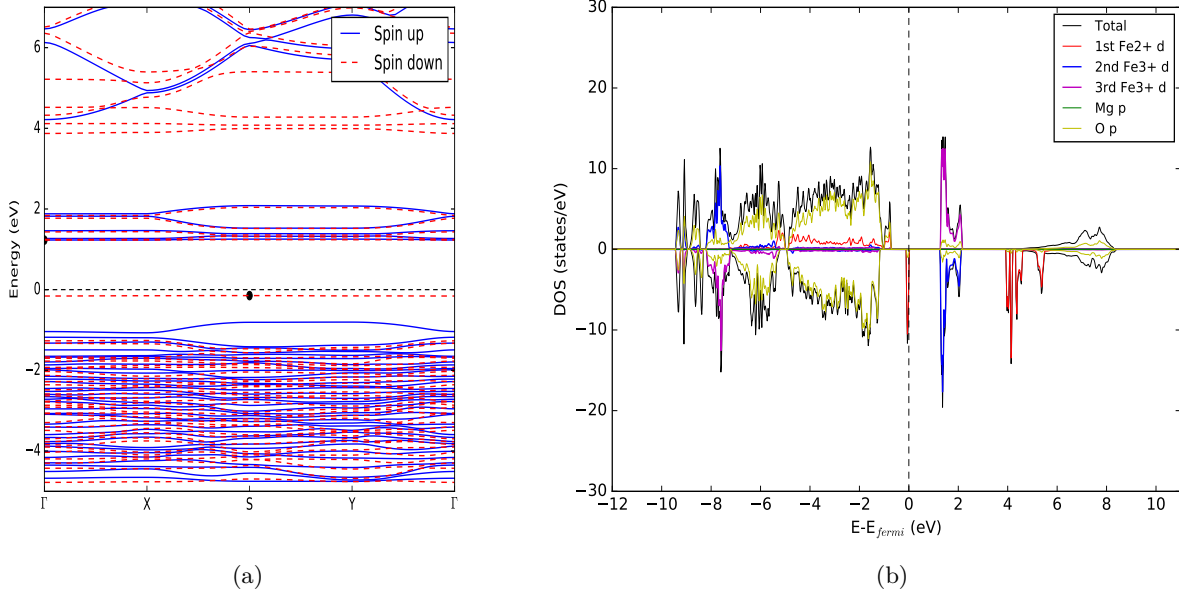


Figure 23: (23a) band structure and (23b) DOS of  $2V_{Li}^-$

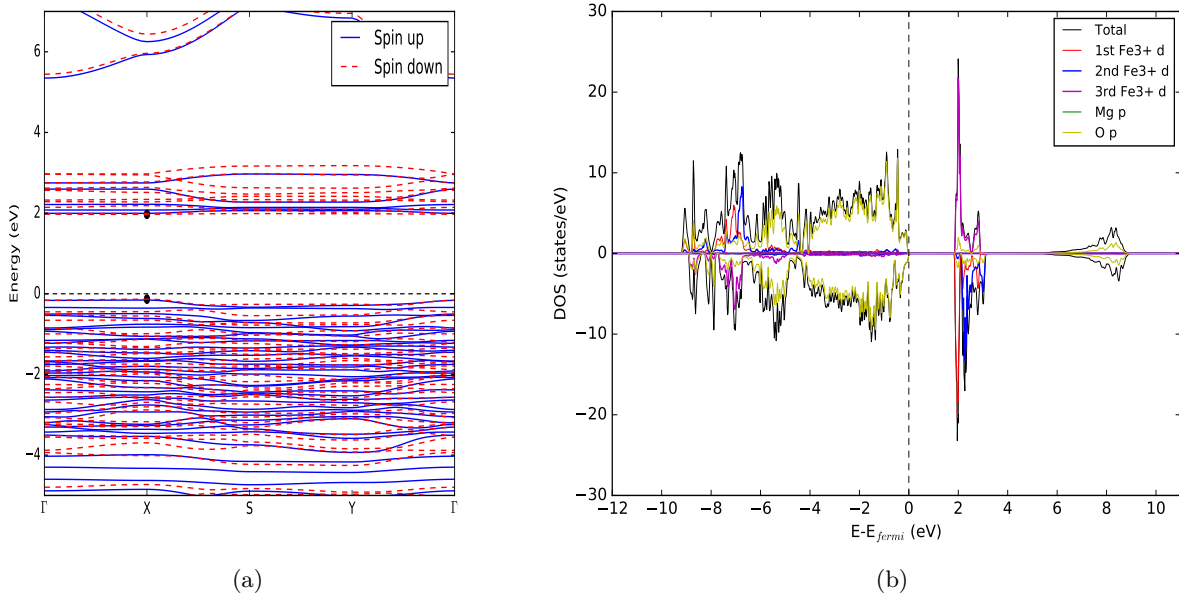


Figure 24: (24a) band structure and (24b) DOS of  $3V_{Li}^-$

The results demonstrate that lattice parameters of all cases reduce because the ionic radius of Mg<sup>2+</sup> (0.72 Å) is less than Fe<sup>2+</sup> (0.78 Å) [35]. In order to confirm the accuracy of our results, we first proceeded the case of 0V<sub>Li</sub><sup>-</sup> which is the normal doping like other experimental and simulated works [50, 35] as shown in table 4. The comparison points out that all lattice parameters are consistent in the reliable range with maximum error only 1.05%. However, although there is no report on magnetic moment, our result is consistent by ourselves with Fe-O bond lengths which are also in precise agreement with another simulation. For the band gap, doping with Mg enlarges the gap about 0.05 eV and still maintains the character of both band and DOS compared with the undoped case as shown in figure 21. Then, when we dope in Li-deficient environment to increase the number of small hole polaron p<sup>+</sup>, all outcomes completely change. One extra Li atom removed represents one V<sub>Li</sub><sup>-</sup>. For the 1V<sub>Li</sub><sup>-</sup>, 2V<sub>Li</sub><sup>-</sup>, and 3V<sub>Li</sub><sup>-</sup>, volumes are fluctuated. Magnetic moment and Fe-O bond length ensure the presence of Mg substituting at Fe site and Fe<sup>3+</sup> transformed from Fe<sup>2+</sup> as highlighted. Turning to analyze band gap for 1V<sub>Li</sub><sup>-</sup> case, as shown in figure 22 compared with figure 21, Fe<sup>2+</sup> state shifts from valence band to conduction band and becomes Fe<sup>3+</sup>. This makes band gap energy much smaller. Then, for 2V<sub>Li</sub><sup>-</sup> case, more Fe<sup>2+</sup> shifts to conduction band obviously seen from the purple spin up dos in figure 23. This also makes band gap smaller than undoped case but wider than 1V<sub>Li</sub><sup>-</sup> case. Eventually, the last group which has 3V<sub>Li</sub><sup>-</sup> (3Fe<sup>3+</sup>) is presented in figure 24. It is apparently seen that peaks of Fe<sup>2+</sup> state at VBM completely disappear. In other word, the Fe<sup>3+</sup> states clearly appear at CBM. This mechanism is called polaronic redox behaviour [25]. Overall, band gap energy depends on Fe d orbital states but does not mean that the more system has Fe<sup>3+</sup>, the wider band gap is.

#### 7.4.2 Effect of Aluminium (Al<sup>3+</sup>) on electronic structure

Oxidation number of Al is +3 so doping with charge compensation has to satisfy this chemical equation: Li<sub>0.75-a</sub>Al<sub>0.25</sub><sup>3+</sup>(Fe<sub>0.75-a</sub><sup>2+</sup>/Fe<sub>a</sub><sup>3+</sup>)[PO<sub>4</sub>]. Hence, in this case *a* can be 0 (1V<sub>Li</sub><sup>-</sup>), 0.25 (2V<sub>Li</sub><sup>-</sup>), 0.50 (3V<sub>Li</sub><sup>-</sup>), and 0.75 (4V<sub>Li</sub><sup>-</sup>).

Table 5: Calculated values of Al doping

Lattice parameters (Å)	EXP <sup>1</sup>	EXP <sup>2</sup>	This work			
	Ref.[55]	Ref.[56]	1V <sub>Li</sub> <sup>-</sup>	2V <sub>Li</sub> <sup>-</sup>	3V <sub>Li</sub> <sup>-</sup>	4V <sub>Li</sub> <sup>-</sup>
a	10.313	10.2547	10.2496	10.0684	9.9845	9.8525
b	6.002	5.9846	5.9773	5.9100	5.8718	5.8138
c	4.691	4.6684	4.7629	4.8197	4.7999	4.8073
volume (Å <sup>3</sup> )	290.35	286.4985	291.7376	286.7651	281.3650	275.3672
Magnetic moment						
1 <sup>st</sup> Al site	-	-	0.002	0.002	0.002	0.002
1 <sup>st</sup> Fe site	-	-	3.774	3.754	3.757	4.311
2 <sup>nd</sup> Fe site	-	-	3.779	3.776	4.304	4.324
3 <sup>rd</sup> Fe site	-	-	-3.772	-4.298	-4.304	-4.306
Fe-O bond length(Å)*						
1 <sup>st</sup> Al site	-	-	1.97	1.93	1.96	1.96
1 <sup>st</sup> Fe site	-	-	2.15	2.15	2.13	2.06
2 <sup>nd</sup> Fe site	-	-	2.18	2.16	2.06	2.05
3 <sup>rd</sup> Fe site	-	-	2.19	2.06	2.06	2.06
Band gap (eV)	-	-	3.421	1.188	0.576	2.341

\*Average value

<sup>1</sup> Experiment 5% doping

<sup>2</sup> Experiment 3% doping

The electronic structure and density of state in each case can be seen below,

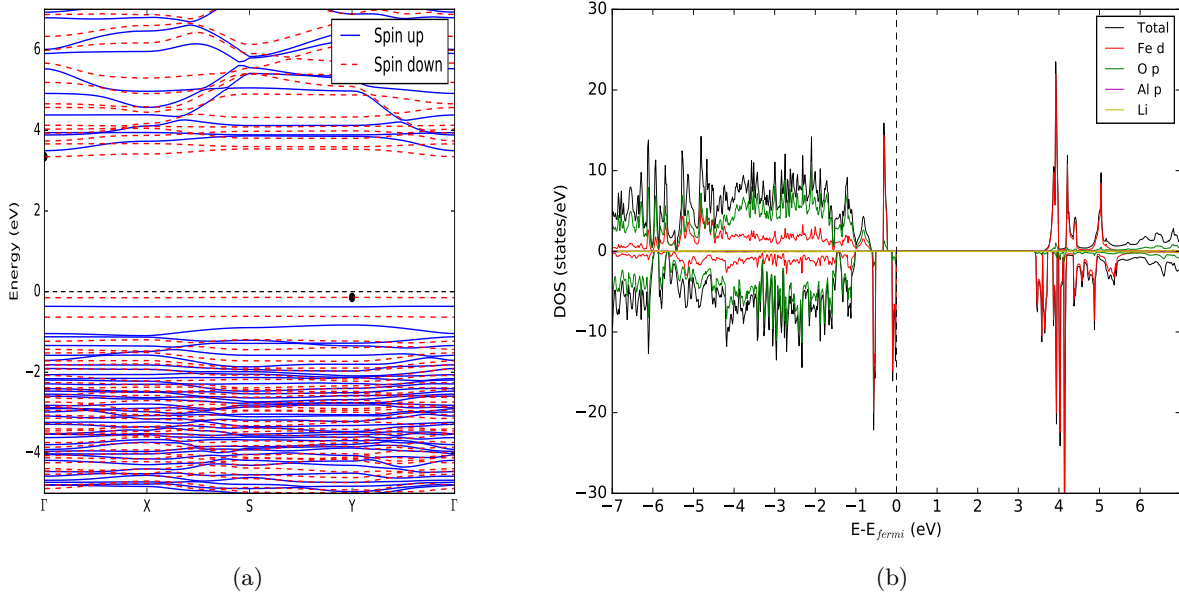


Figure 25: (40a) band structure and (40b) DOS of  $1V_{Li}^-$

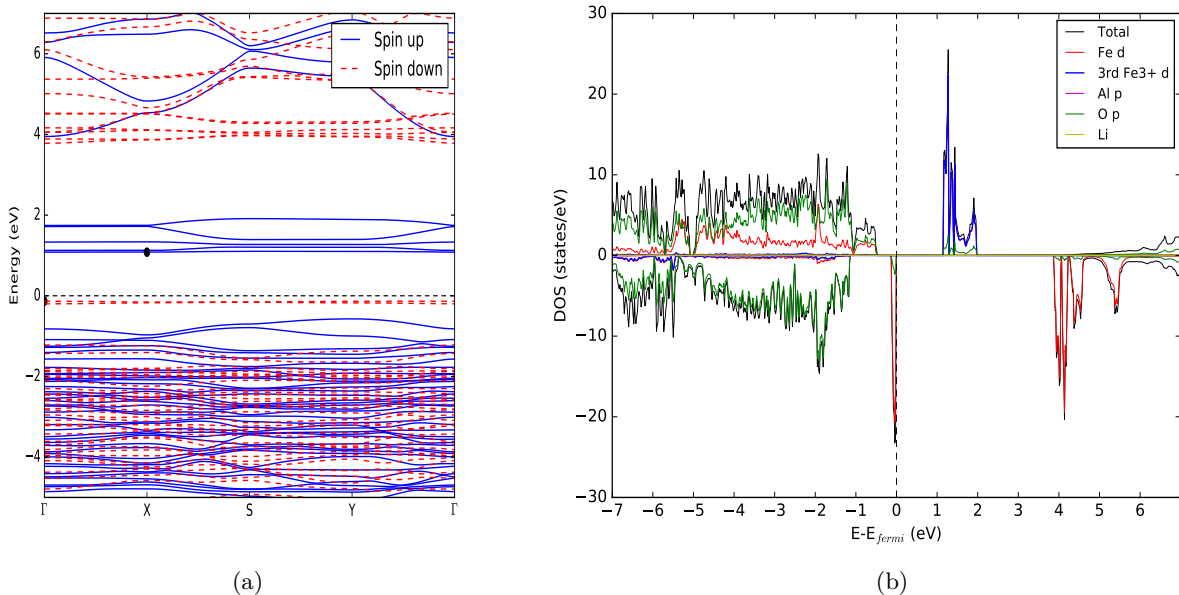


Figure 26: (42a) band structure and (42b) DOS of  $2V_{Li}^-$

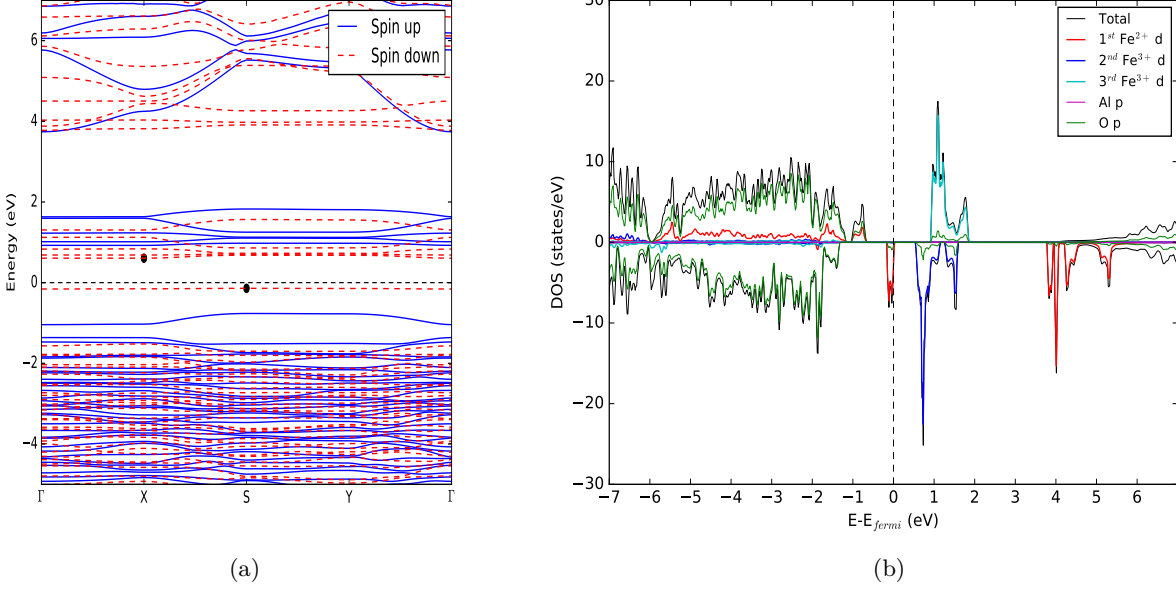


Figure 27: (44a) band structure and (44b) DOS of  $3V_{Li}^-$

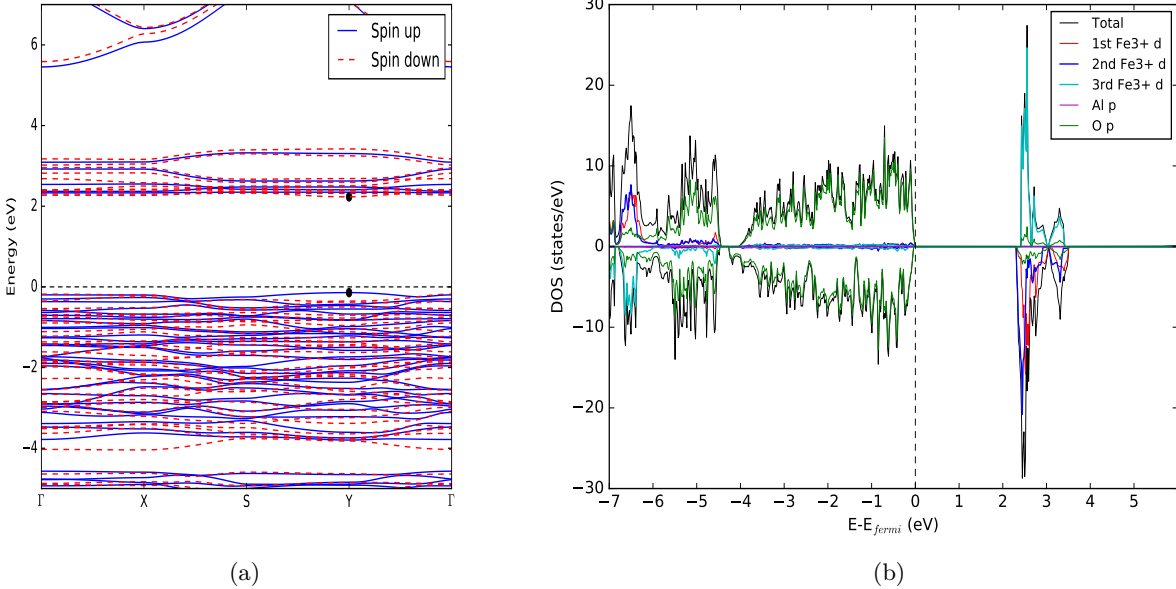


Figure 28: (46a) band structure and (46b) DOS of  $4V_{Li}^-$

The results demonstrate that lattice parameters of all cases are shorter than LiFePO<sub>4</sub> because the ionic radius of Al<sup>3+</sup> (0.54 Å) is less than Fe<sup>2+</sup> (0.78 Å) [55]. In order to confirm the accuracy of our results, we first proceeded the case of  $1V_{Li}^-$  which is the normal doping like other experimental works [55, 56] as shown in table 5. The comparison points out that all lattice parameters are varied in the reliable range with maximum error only 1.53%. However, although there is no report on magnetic moment, our result is consistent by ourselves with Fe-O bond lengths. For the band gap, doping with Al decreases the gap about 0.4 eV as shown in figure 25 which results from loss of antiferromagnetic

state. It means that the configuration behaves like ferrormagnetic state because Al-doped atom is not magnetic state. Therefore, the states in VBM and CBM approach each other more than the undoped case so it causes the reduction of band gap. This result can enhance the electronic conductivity because of smaller band gap. Moreover, some experimental work [56] analyzed from XPS data and concluded that metal doping like Al can improve conductivity as it weakens Li-O interaction which helps Li ion diffuse more easily. Then, we dope in Li-deficient environment to increase the number of  $V_{Li}^-$ . For the  $2V_{Li}^-$ ,  $3V_{Li}^-$ , and  $4V_{Li}^-$ , lattice parameters reduce because of disappearance of Li atom. Moreover, magnetic moment and Fe-O bond length ensure the presence of Al substituting at Fe site and  $Fe^{3+}$  transformed from  $Fe^{2+}$  as highlighted. Turning to analyze band gap for  $2V_{Li}^-$  case, as shown in figure 26 compared with figure 25,  $Fe^{2+}$  state shifts from valence band to conduction band and becomes  $Fe^{3+}$  since small hole polaron successfully localizes at that site. Then, for  $3V_{Li}^-$  case, all the mechanism is in the same tendency. That is, the much narrower band gap stems from the localization of small hole polaron. Finally, the last group which has  $4V_{Li}^-$  ( $3Fe^{3+}$ ) is presented in figure 28. It is apparently seen that peaks of  $Fe^{2+}$  state at VBM completely disappear. In other word, the  $Fe^{3+}$  states clearly appear at CBM. This narrower band gap in delithiation process also has positive impact on electronic conductivity improvement.

#### 7.4.3 Effect of Titanium ( $Ti^{4+}$ ) on electronic structure

Oxidation number of Ti is +4 so doping with charge compensation has to satisfy this chemical equation:  $Li_{0.5-a}^+ Ti_{0.25}^{4+} (Fe_{0.75-a}^{2+}/Fe_a^{3+})[PO_4]$ . Hence, in this case  $a$  can be 0 ( $2V_{Li}^-$ ), 0.25 ( $3V_{Li}^-$ ), and 0.50 ( $4V_{Li}^-$ ).

Table 6: Calculated values of Ti doping

Lattice parameters (Å)	EXP <sup>1</sup>	This work		
	Ref.[50]	$2V_{Li}^-$	$3V_{Li}^-$	$4V_{Li}^-$
a	10.3290(4)	10.3166	10.0122	10.0006
b	6.0096(8)	6.0288	5.9083	5.9167
c	4.6946(8)	4.8716	4.9855	4.8959
volume (Å <sup>3</sup> )	-	302.8843	294.8619	289.6843
Magnetic moment				
1 <sup>st</sup> Ti site	-	0.032	0.032	0.033
1 <sup>st</sup> Fe site	-	3.776	3.750	4.3
2 <sup>nd</sup> Fe site	-	3.778	3.774	3.778
3 <sup>rd</sup> Fe site	-	-3.776	-4.298	-4.303
Fe-O bond length(Å)*				
1 <sup>st</sup> Ti site	-	2.02	2.01	2.01
1 <sup>st</sup> Fe site	-	2.18	2.17	2.06
2 <sup>nd</sup> Fe site	-	2.18	2.18	2.17
3 <sup>rd</sup> Fe site	-	2.19	2.06	2.06
Band gap (eV)	-	0.973	1.459	0.937

\*Average value

<sup>1</sup> Experiment 2% doping

The electronic structure and density of state in each case can be seen below,

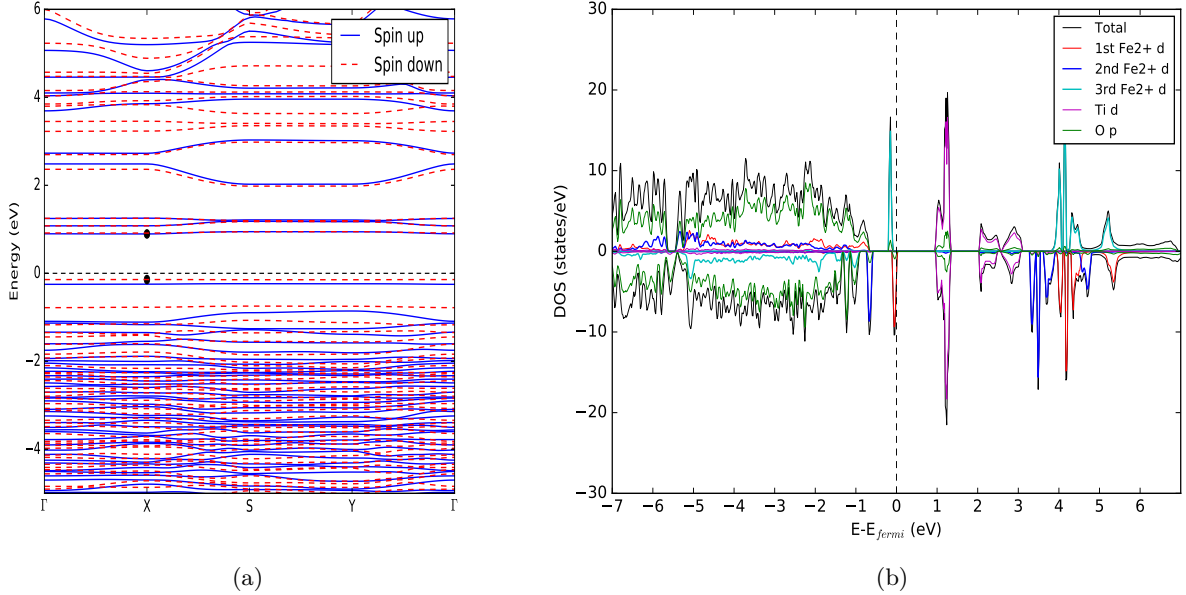


Figure 29: (29a) band structure and (29b) DOS of  $2V_{Li}^-$

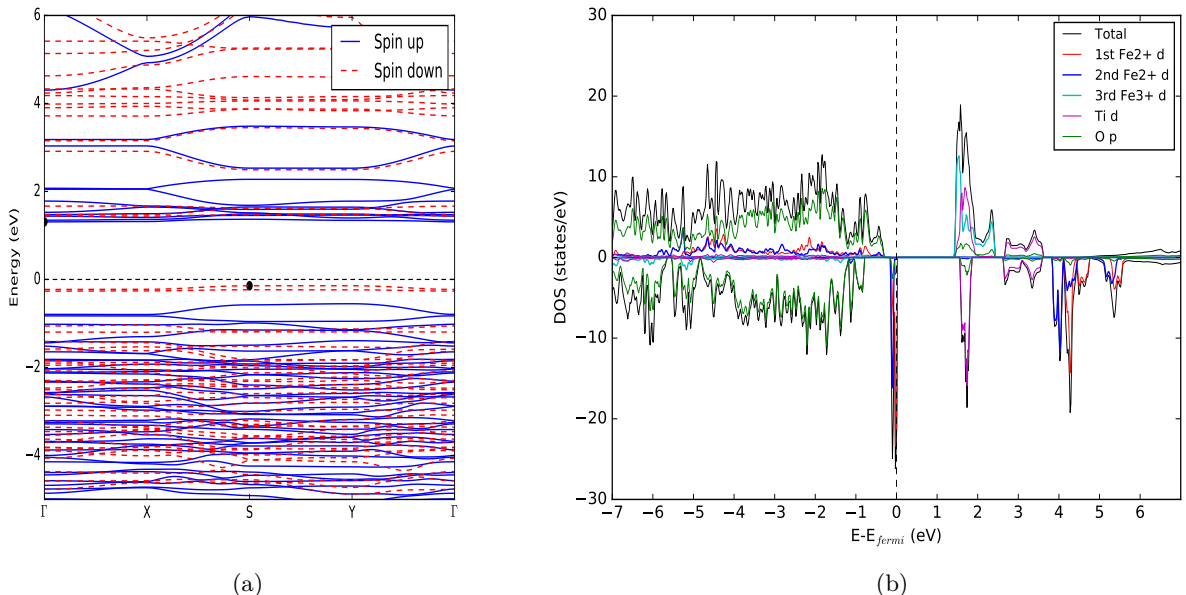


Figure 30: (30a) band structure and (30b) DOS of  $3V_{Li}^-$

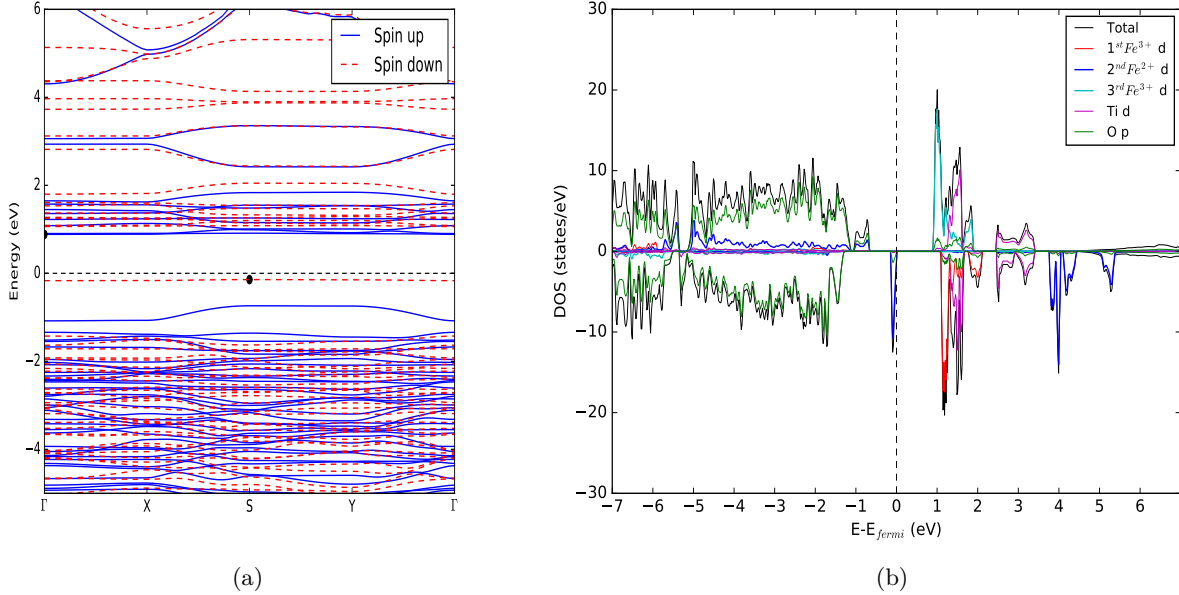


Figure 31: (51a) band structure and (51b) DOS of  $4V_{Li}^-$

The results demonstrate that although the ionic radius of  $Ti^{4+}$  ( $0.61 \text{ \AA}$ ) is less than  $Fe^{2+}$  ( $0.78 \text{ \AA}$ ) [50], all lattice parameters is smaller except for  $2V_{Li}^-$  case. It results from effect of  $V_{Li}^-$ . However, the range of lattice parameters is not too much different when compared with the experiment [50] as shown in table 6. The comparison points out that all lattice parameters are varied in the reliable range with maximum error only 3.79%. Although there is no report on magnetic moment, our result is consistent with Fe-O bond lengths. For the band gap, doping with Ti decreases the gap to 0.973 eV as shown in figure 29 which results from creating extra state at conduction band near fermi level of Ti d orbital which is actually the small hole polaron state. This result can highly enhance the electronic conductivity because of smaller band gap. Then, we dope in Li-deficient environment to increase the number of  $V_{Li}^-$ . For the  $3V_{Li}^-$  and  $4V_{Li}^-$ , magnetic moment and Fe-O bond length ensure the presence of Ti substituting at Fe site and  $Fe^{3+}$  transformed from  $Fe^{2+}$  as highlighted. Turning to analyze band gap for  $3V_{Li}^-$  case, as shown in figure 30 compared with figure 29,  $Fe^{2+}$  state shifts from valence band to conduction band and becomes  $Fe^{3+}$  due to localisation of hole polaron. That is, the polaronic behaviour happens. It cause mixing states between  $Fe^{3+}$  and  $Ti^{4+}$  which makes band gap energy narrower than pure case but larger than  $2V_{Li}^-$  case. Last,  $4V_{Li}^-$  ( $2Fe^{3+}$ ) is presented in figure 31. It is also the combination of extra Ti state and polaronic redox behaviour which reduce band gap energy to only 0.937 eV. This high narrower band gap in delithiation process also has positive impact on electronic conductivity improvement.

#### 7.4.4 Effect of Zirconium ( $Zr^{4+}$ ) on electronic structure

Since oxidation number of Zr is +4, doping with charge compensation has to satisfy this chemical equation:  $Li_{0.5-a}^+Zr_{0.25}^{4+}(Fe_{0.75-a}^{2+}/Fe_a^{3+})[PO_4]$ . Hence, in this case  $a$  can be 0 ( $2V_{Li}^-$ ), 0.25 ( $3V_{Li}^-$ ), and 0.50 ( $4V_{Li}^-$ ).

Table 7: Calculated values of Zr doping

Lattice parameters (Å)	EXP <sup>1</sup> Ref.[55]	EXP <sup>2</sup> Ref.[56]	2V <sub>Li</sub> This work	3V <sub>Li</sub> This work	4V <sub>Li</sub> This work
a	10.317	10.2729	10.4477	10.12447	10.1744
b	6.004	5.9989	6.1246	5.98801	6.0188
c	4.693	4.6782	4.9316	5.06011	4.9640
volume (Å <sup>3</sup> )	290.65	288.2948	315.5154	306.7234	303.9883
Magnetic moment					
1 <sup>st</sup> Zr site	-	-	0.010	0.008	0.009
1 <sup>st</sup> Fe site	-	-	3.779	3.752	4.296
2 <sup>nd</sup> Fe site	-	-	3.783	3.779	3.783
3 <sup>rd</sup> Fe site	-	-	-3.777	-4.304	-4.302
Fe-O bond length(Å)*					
1 <sup>st</sup> Zr site	-	-	2.14	2.13	2.13
1 <sup>st</sup> Fe site	-	-	2.20	2.19	2.07
2 <sup>nd</sup> Fe site	-	-	2.19	2.21	2.18
3 <sup>rd</sup> Fe site	-	-	2.20	2.07	2.07
Band gap (eV)	-	-	2.978	1.537	0.991

\*Average value

<sup>1</sup> Experiment 5% doping

<sup>2</sup> Experiment 3% doping

The electronic structure and density of state in each case can be seen below,

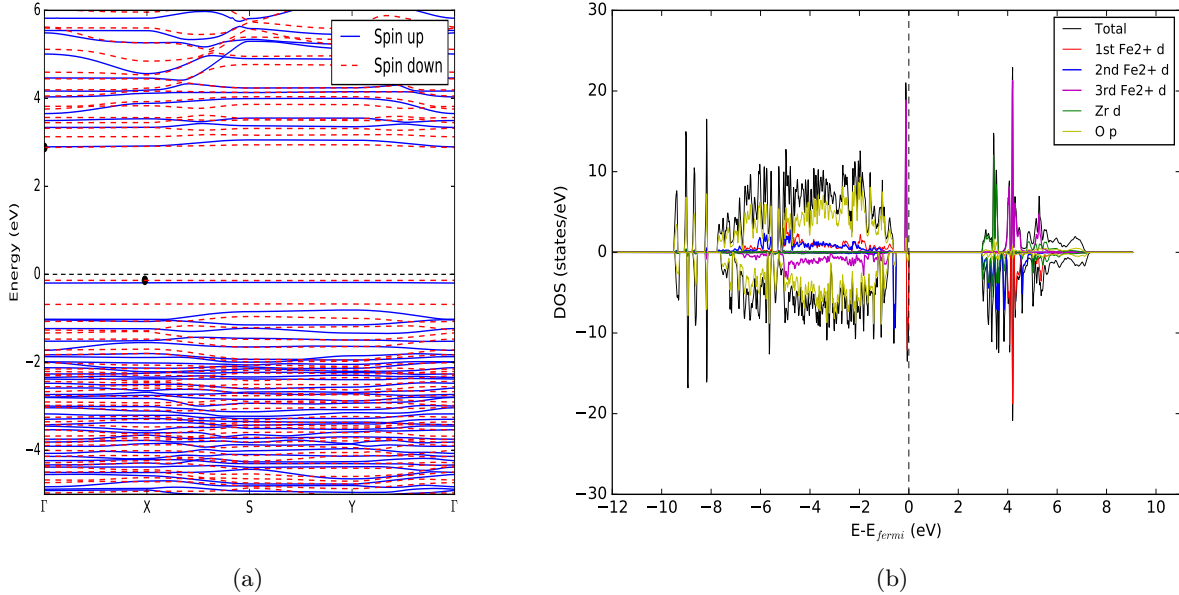


Figure 32: (32a) band structure and (32b) DOS of 2V<sub>Li</sub>

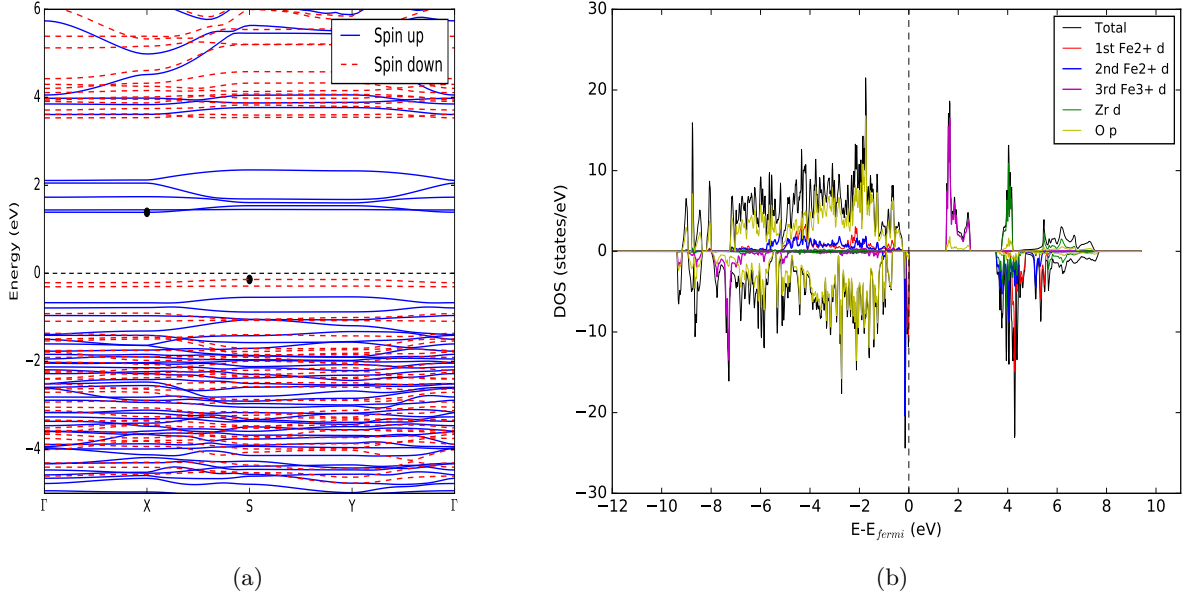


Figure 33: (33a) band structure and (33b) DOS of  $3V_{Li}^-$

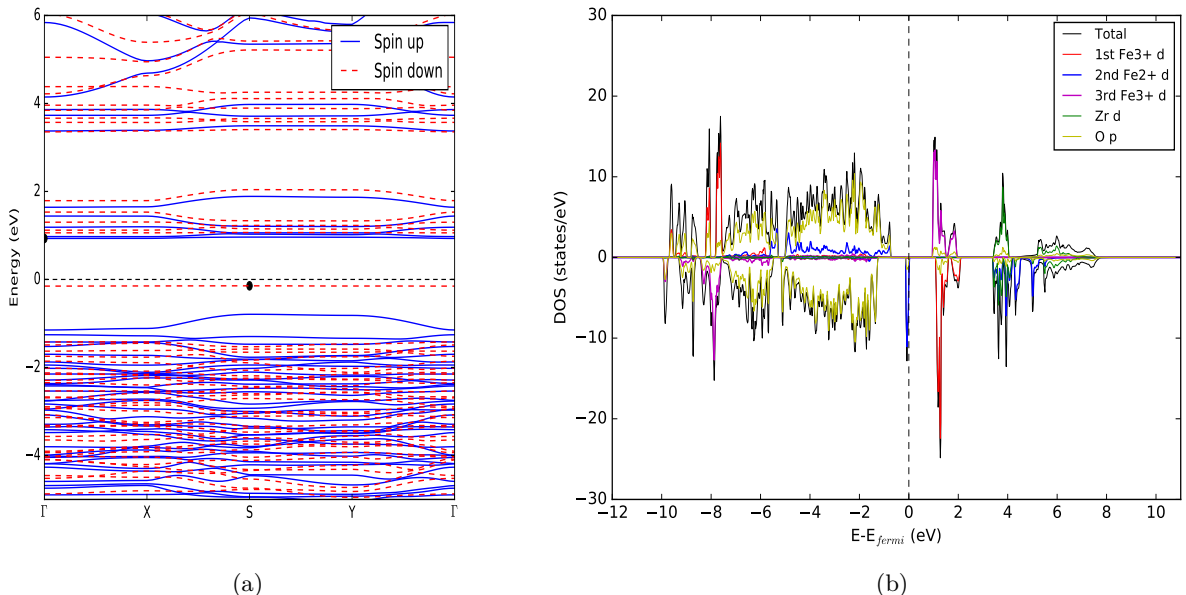


Figure 34: (34a) band structure and (34b) DOS of  $4V_{Li}^-$

The calculated values from table 7 demonstrate that even though the ionic radius of Zr<sup>4+</sup> (0.72 Å) is less than Fe<sup>2+</sup> (0.78 Å) [50], all lattice parameters is higher than the undoped case. Our calculated values are in satisfactory keeping with the experimental result [55]. This contradiction originates from removing V<sub>Li</sub><sup>-</sup> during doping for charge compensation. In other words, trend by ionic radius is not violated unless V<sub>Li</sub><sup>-</sup> is removed. Although there is no report on magnetic moment, our result is consistent with Fe-O bond length. For the band gap, doping with Zr as shown in figure 32 decreases the band gap from the undoped case which results from Fe<sup>2+</sup> state at VBM and Zr d-orbital state at conduction band at CBM. This result can highly enhance the electronic conductivity because of smaller band gap. Then, we dope in Li-deficient environment to increase the number of V<sub>Li</sub><sup>-</sup>. For the 3V<sub>Li</sub><sup>-</sup> and 4V<sub>Li</sub><sup>-</sup>, magnetic moment and Fe-O bond length ensure the presence of Zr substituting at Fe site and Fe<sup>3+</sup> transformed from Fe<sup>2+</sup> as highlighted. Turning to analyze band gap for 3V<sub>Li</sub><sup>-</sup> case, as shown in figure 33 compared with figure 32, Fe<sup>2+</sup> ion shifts from valence band to conduction band and becomes Fe<sup>3+</sup>. It can also evidently seen that the polaronic behaviour mainly exists rather than Zr d orbital. Last, 4V<sub>Li</sub><sup>-</sup> (2Fe<sup>3+</sup>) is presented in figure 34. The primary contributors around fermi level are Fe<sup>2+</sup> and Fe<sup>3+</sup> which are polaronic redox behaviour [25] affecting the reduction of band gap energy to only 0.991 eV. This high narrower band gap in delithiation process also has positive impact on electronic conductivity improvement.

#### 7.4.5 Effect of Niobium (Nb<sup>5+</sup>) on electronic structure

As oxidation number of Nb is +5, doping with charge compensation has to satisfy this chemical equation: Li<sub>0.25-a</sub>Nb<sub>0.25</sub><sup>5+</sup>(Fe<sub>0.75-a</sub><sup>2+</sup>/Fe<sub>a</sub><sup>3+</sup>)[PO<sub>4</sub>]. Hence, in this case *a* can be 0 (3V<sub>Li</sub><sup>-</sup>) and 0.25 (4V<sub>Li</sub><sup>-</sup>).

Table 8: Calculated values of Nb doping

Lattice parameters (Å)	EXP <sup>1</sup> Ref.[55]	EXP <sup>2</sup> Ref.[57]	SIM <sup>3</sup> Ref.[36]	This work	
				3V <sub>Li</sub> <sup>-</sup>	4V <sub>Li</sub> <sup>-</sup>
a	10.318	10.32252(9)	10.43	10.1231	10.0501
b	6.0045	6.00098(6)	6.06	6.1586	6.0466
c	4.696	4.6782	4.69633(5)	5.0807	4.9993
volume (Å <sup>3</sup> )	290.75	290.054(8)	298.96	316.6497	303.7795
Magnetic moment					
1 <sup>st</sup> Nb site	-	-	-	0.002	0.0014
1 <sup>st</sup> Fe site	-	-	-	3.754	4.31
2 <sup>nd</sup> Fe site	-	-	-	3.779	3.772
3 <sup>rd</sup> Fe site	-	-	-	-3.765	-3.767
Fe-O bond length(Å)*					
1 <sup>st</sup> Nb site	-	-	-	2.02	2.02
1 <sup>st</sup> Fe site	-	-	-	2.15	2.06
2 <sup>nd</sup> Fe site	-	-	-	2.21	2.20
3 <sup>rd</sup> Fe site	-	-	-	2.12	2.18
Band gap (eV)	-	-	-	1.188	1.315

\*Average value

<sup>1</sup> Experiment 5% doping

<sup>2</sup> Experiment 1% doping

<sup>3</sup> Simulation 12.5% doping

The electronic structure and density of state in each case can be seen below,

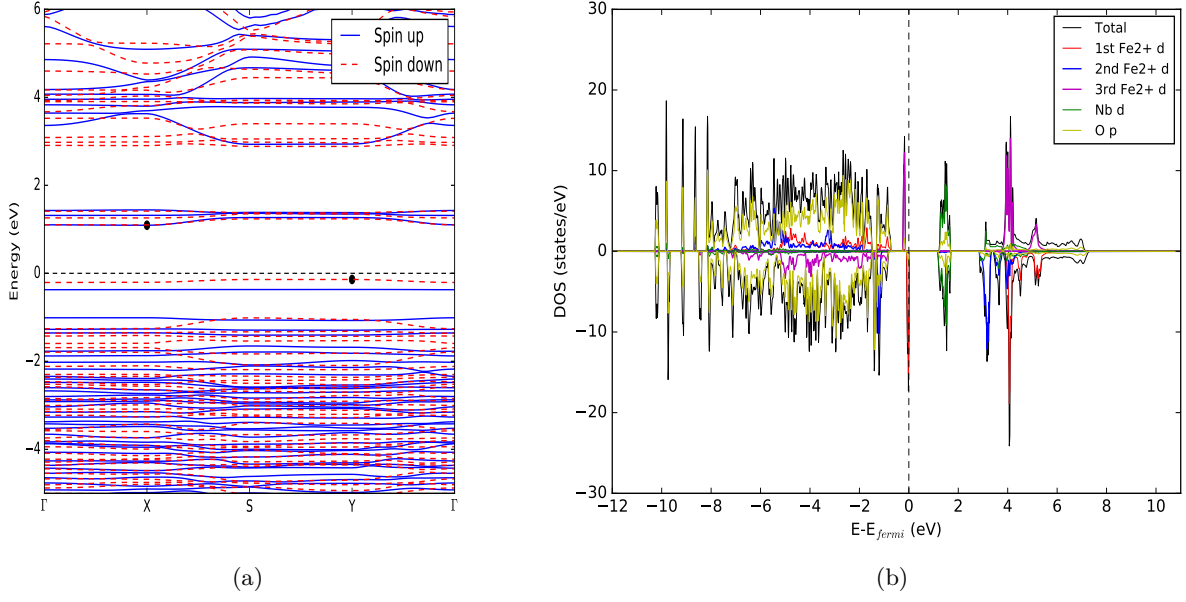


Figure 35: (35a) band structure and (35b) DOS of  $3V_{Li}^-$

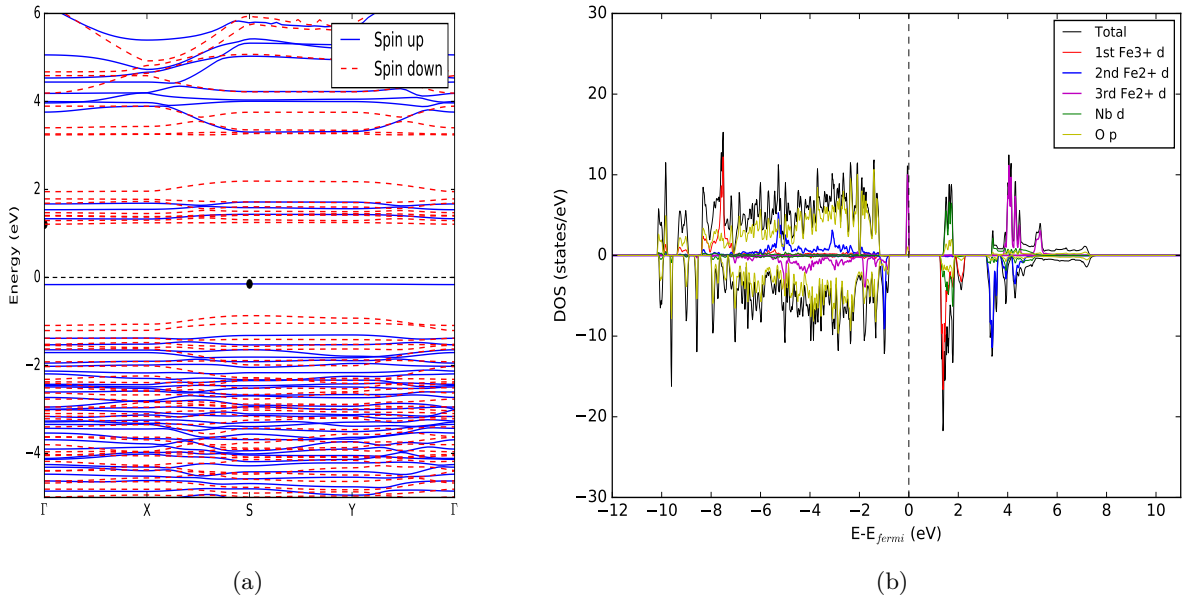


Figure 36: (36a) band structure and (36b) DOS of  $4V_{Li}^-$

The calculated values from table 8 points out that even though the ionic radius of Nb<sup>5+</sup> (0.64 Å) is less than Fe<sup>2+</sup> (0.78 Å) [50], all lattice parameters is higher than the undoped case. Our calculated values are in satisfactory accordance with the experimental result [55]. It means that the tendency cannot be judged only ionic radius. Then, although there is no report on magnetic moment, our result is consistent with Fe-O bond lengths. For the band gap, doping with Nb decreases band gap as shown in figure 35 which results from Fe<sup>2+</sup> state in VBM and d orbital state of Nb in CBM. Then, we dope in Li-deficient environment to increase the number of V<sub>Li</sub><sup>-</sup>. For the 4V<sub>Li</sub><sup>-</sup>, magnetic moment and Fe-O bond length ensure the presence of Nb substituting at Fe site and Fe<sup>3+</sup> transformed from Fe<sup>2+</sup> as highlighted. it indicates that it has Fe<sup>3+</sup> existing at 1<sup>st</sup> Fe site. Its smaller band gap is affected by Fe<sup>2+</sup> in valence band and combination of Fe<sup>3+</sup> and Nb d-orbital.

#### 7.4.6 Conclusion

We have investigated effect of types of dopant and lithium vacancy on electronic structure under Li-deficient condition. Based on band structure and DOS, the results indicate that doping with Mg prefers existing polaronic redox behaviour rather than creating new state. Normal doping cannot enhance electronic conductivity due to its larger band gap. However, it is possible for improvement if it is in Li-deficient condition. Conductivity will be improved if both lithiation (LiFePO<sub>4</sub>) and delithiation (FePO<sub>4</sub>) processes improve. Thus, we still cannot determine Mg dopant owing to impossibility of delithiation case. For Al dopant, it can enhance electronic conductivity based on narrower band gap. This case also points out that the more Li vacancy we have, the narrower band gap is. In addition, the delithiation also has little smaller band gap so doping with Al may enhance electronic conductivity. For Ti dopant, it can clearly seen that narrower energy gap originates from new additional state of Ti d-orbital. It is acceptable that major contribution near fermi level of LiFePO<sub>4</sub> comes from d orbital. Hence, we believe that Ti doping can enhance electronic conductivity because of smaller energy gap in all cases. Then, doping with Zr can enhance electronic conductivity observed by disappearing and smaller band gap although the atom mainly contributing near fermi level is not Zr-d orbital only in case of delithiation. Eventually, doping with Nb seems to be able to improve electronic conductivity and its band gap is mainly dominated by Nb atom. Nevertheless, the data is now insufficient to determine so we need to analyze it again in supercell doping.

### 7.5 Effect of supervalent cations and Lithium vacancies on LiFePO<sub>4</sub> electronic structure in supercell

All investigation was implemented in 1 × 2 × 2 supercell to dilute dopants at least 6.25%. After randomly vary configurations, we found that the transition between Fe<sup>2+</sup> and Fe<sup>3+</sup> is not completed in some configuration. In other words, Fe<sup>2+</sup> is not fully oxidized to Fe<sup>3+</sup> in some configuration which leads to misleading band structure and density of state. In order to avoid this issue, we optimized 3 different configurations and selected only lowest total energy configuration to study electronic band structure and density of state.

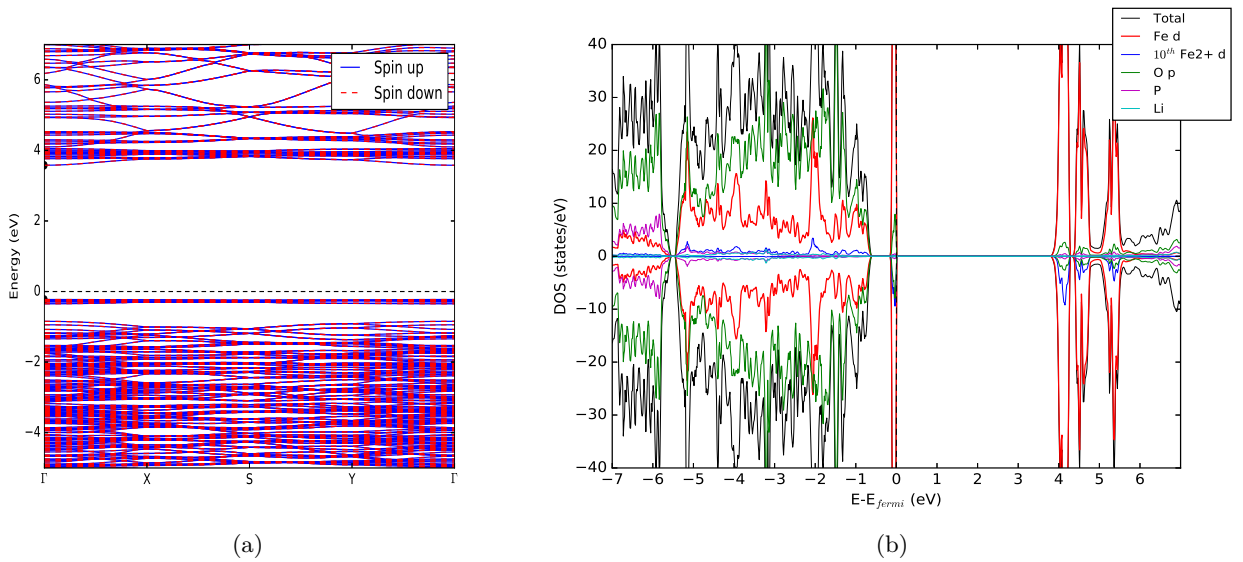
#### 7.5.1 Effect of Aluminium (Al<sup>3+</sup>) on electronic structure

**7.5.1.1 Lithiation phase** In this section, we discuss effect of Al dopant on electronic structure but the number of lithium vacancy (V<sub>Li</sub><sup>-</sup>) is implemented only for charge balance. Thus, all structures can be expressed as Li<sub>16</sub>Fe<sub>16</sub>(PO<sub>4</sub>)<sub>16</sub> for undoped case, Li<sub>15</sub>AlFe<sub>15</sub>(PO<sub>4</sub>)<sub>16</sub> for 6.25% doping case, Li<sub>14</sub>Al<sub>2</sub>Fe<sub>14</sub>(PO<sub>4</sub>)<sub>16</sub> for 12.5% doping case, and Li<sub>3</sub>AlFe<sub>3</sub>(PO<sub>4</sub>)<sub>4</sub> for 25% doping case. The data is summarized as shown in table below.

Table 9: Calculated values of Al doping

Para- meter	Exp <sup>1</sup> [Ref.[55]]		Exp <sup>2</sup> [Ref.[56]]		Pure	6.25%doping		12.5%doping		25%doping		
	pure	doping	pure	doping	unitcell	supercell value	%changevalue	%changevalue	%changevalue	%change		
a	10.313	10.313	10.287	10.255	10.416	10.266	10.350	0.820	10.310	0.435	10.250	-1.59
b	6.003	6.002	6.002	5.985	6.062	11.990	12.084	0.785	12.043	0.439	5.978	-1.39
c	4.694	4.691	4.683	4.668	4.745	9.372	9.496	1.326	9.526	1.643	4.820	1.58
V	290.50	290.35	289.11	286.50	299.61	1153.62	1187.74	2.958	1182.81	2.751	291.738	-2.63
Atom	-	-	-	-	1 <sup>st</sup> Fe							
Moment	-	-	-	-	3.76 $\mu_B$	3.77 $\mu_B$	-3.77 $\mu_B$	-3.77 $\mu_B$	-3.77 $\mu_B$	-3.77 $\mu_B$		
Fe-O(Å)	-	-	-	-	2.16	2.16	2.15	2.17	2.17	2.16		
Gap(eV)	-	-	-	-	3.827	3.643	3.423	3.423	3.421	3.421		

<sup>1</sup> Experiment 5% doping

<sup>2</sup> Experiment 3% doping

 Figure 37: Band structure and density of state: (37a) and (37b) for  $\text{Li}_{16}\text{Fe}_{16}(\text{PO}_4)_{16}$ 

As reported in table 9, Al doping enlarges cell volume especially in z-direction. Despite expansion of volume, when  $\text{LiFePO}_4$  is doped with more Al concentration, volume will slightly reduce in accordance with experiment [55, 56]. Then, one atom site is selected to consider the existence of small hole polaron via magnetic moment and bond length. Both data indicates the delocalization of small hole polaron which is correct because charge compensation can be dealt with only by Li removal in this case so small hole polaron does not need to occur. These results are consistent with electronic band structure and density of state as illustrated in fig 37 and fig 38. That is, there is no extra state existing near fermi energy at the conduction band. This indicates that Al doping can reduce the band gap energy because it destroys antiferromagnetic characteristics as seen in fig 38. It causes some states from VBM and CBM approaching fermi level more and more so the band gap energy is reduced.

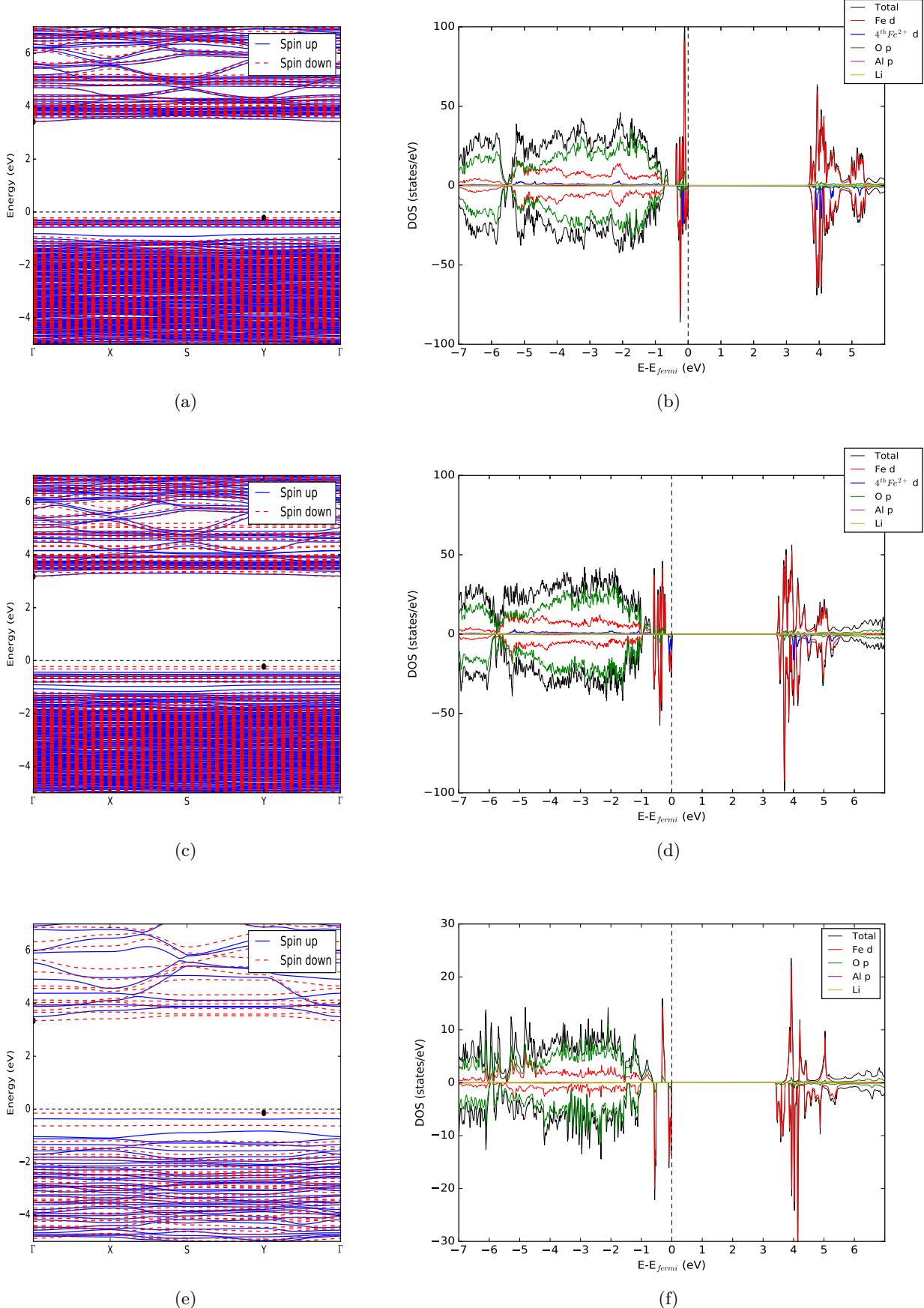


Figure 38: Band structure and density of state: (38a) and (38b) for  $\text{Li}_{15}\text{AlFe}_{15}(\text{PO}_4)_{16}$ , (38c), (38d) for  $\text{Li}_{14}\text{Al}_2\text{Fe}_{14}(\text{PO}_4)_{16}$ , and (40a) and (40b) for  $\text{Li}_3\text{AlFe}_3(\text{PO}_4)_4$

**7.5.1.2 One small hole polaron phase** In this section, we discuss effect of Al dopant on electronic structure and the additional number of lithium vacancy ( $V_{Li}^-$ ) for creating one small hole polaron. In other words, this phase is in Li deficient environment as follows:  $Li_{15}Fe_{16}(PO_4)_{16}$  for undoped case,  $Li_{14}AlFe_{15}(PO_4)_{16}$  for 6.25% doping and  $Li_{13}Al_2Fe_{14}(PO_4)_{16}$  for 12.5% doping case. All of these are also doped under 1 Li atom deficiency (6.25% Li deficiency). The data is summarized as shown in table below.

Table 10: Calculated values of combined Al doping and one Li deficiency

Lattice parameters	Undope unitcell	supercell	6.25% doping values	%difference	12.5% doping values	%difference
a(Å)	10.326	10.3727	10.3248	-0.461	10.2819	-0.875
b(Å)	6.027	12.1073	12.0552	-0.431	12.0025	-0.866
c(Å)	4.788	9.5056	9.5282	0.238	9.5358	0.317
Volume (Å <sup>3</sup> )	297.957	1193.7516	1185.9491	-0.654	1176.769	-1.423
Atom site	3 <sup>rd</sup> Fe	10 <sup>th</sup> Fe	1 <sup>st</sup> Al	4 <sup>th</sup> Fe	1 <sup>st</sup> Al	4 <sup>th</sup> Fe
Mag moment( $\mu_B$ ) <sup>1</sup>	4.295	4.296	0.001	4.292	0.001	-4.29
Fe-O length(Å)	2.05	2.0598	1.9749	2.0582	1.9586	2.0569
Band gap (eV)	1.024	1.288	1.552		1.772	

<sup>1</sup> magnetic moment at only selected site

<sup>2</sup> average value

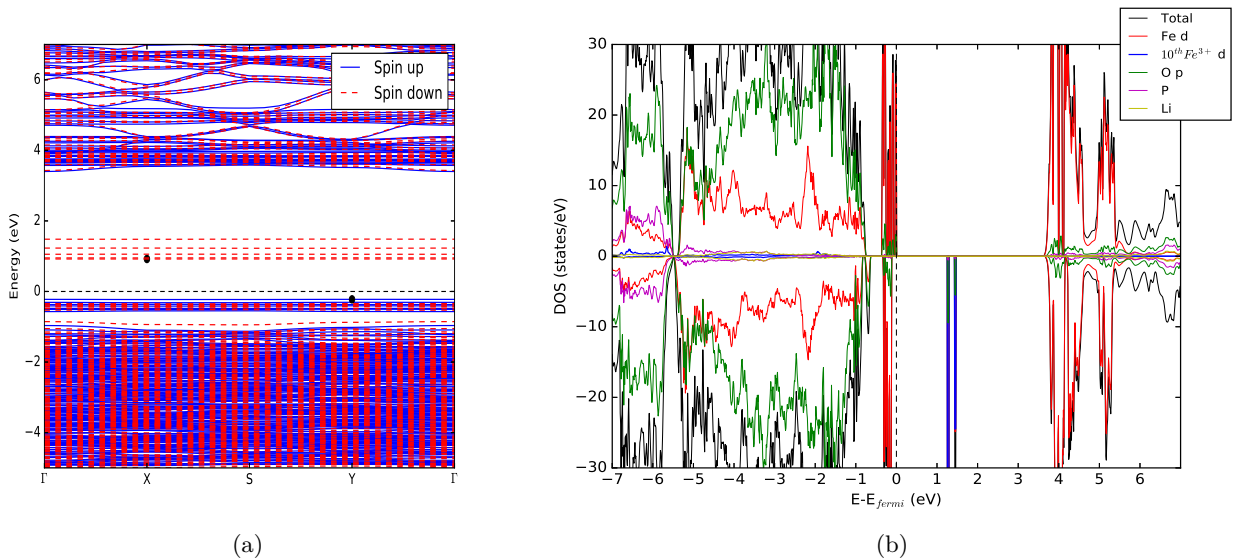


Figure 39: (39a) band structure and (39b) DOS of  $Li_{15}Fe_{16}(PO_4)_{16}$

According to table 10, Al dopant reduces the cell volume in agreement with the previous case. Magnetic moment and Fe-O bond length of some atom sites are chosen to verify the localization of Al doping and small hole polaron. An Al substituting at Fe site has zero magnetic moment with Al-O bond length around 1.9 Å. Since this system is doped under 1 Li deficiency, this induces the transition between  $Fe^{2+}$  and  $Fe^{3+}$  which causes the localization of small hole polaron ( $p^+$ ) around  $Fe^{3+}$  site. This can be confirmed by band structure and DOS as shown in fig 39 and fig 40. Obviously, there is extra state existing at the conduction band which is actually small hole polaron state. However, from the view of band gap energy, Al cannot provide the narrower band gap which is in good agreement with the calculated defect formation energy from Hoang [21]. Therefore, this case is needed to consider with the aspect of the energy barriers of Li and  $p^+$  hoppings by NEB calculation again to clarify whether Al doping with one Li deficiency improves conductivity performance.

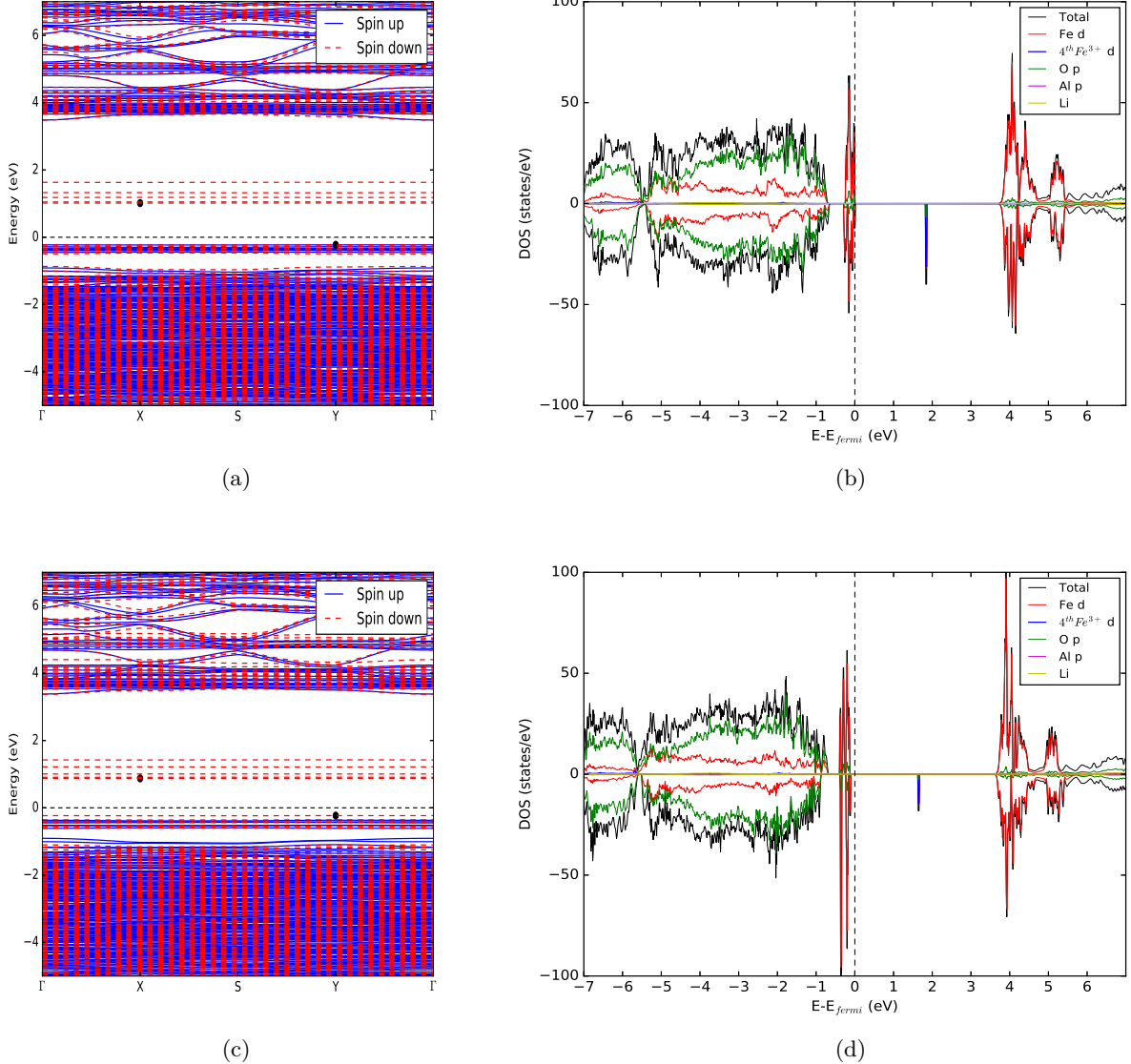


Figure 40: Band structure and density of state: (40a) and (40b) for  $\text{Li}_{14}\text{AlFe}_{15}(\text{PO}_4)_{16}$  and (40c) and (40d) for  $\text{Li}_{13}\text{Al}_2\text{Fe}_{14}(\text{PO}_4)_{16}$ .

**7.5.1.3 Two small hole polarons phase** In this section, we discuss effect of Al dopant on electronic structure and the additional number of lithium vacancy ( $V_{Li}^-$ ) for creating two small hole polaron. Thus, the structure can be written as  $\text{Li}_{14}\text{Fe}_{16}(\text{PO}_4)_{16}$  for undoped case,  $\text{Li}_{13}\text{AlFe}_{15}(\text{PO}_4)_{16}$  for 6.25% doping and  $\text{Li}_{12}\text{Al}_2\text{Fe}_{14}(\text{PO}_4)_{16}$  for 12.5% doping case. All of these cases are doped under two Li deficient environment (12.5% Li deficiency). The data is summarized as shown in table below.

Table 11: Calculated values of combined Al doping and two Li deficiency

Lattice parameters	Undope		6.25% doping		12.5% doping	
	unitcell	supercell	values	%difference	values	%difference
a(Å)	10.141	10.3408	10.2995	-0.399	10.249	-0.888
b(Å)	5.946	12.0785	12.0239	-0.452	11.979	-0.819
c(Å)	4.811	9.5206	9.5498	0.306	9.557	0.386
volume (Å <sup>3</sup> )	290.053	1189.1267	1182.6315	-0.546	1173.368	-1.325
Atom site	5 <sup>th</sup> Fe	9 <sup>th</sup> Fe	2 <sup>nd</sup> Fe	15 <sup>th</sup> Fe	1 <sup>st</sup> Fe	6 <sup>th</sup> Fe
Mag moment <sup>1</sup>	4.294	4.294	-4.297	-4.296	-4.284	4.291
Fe-O length(Å)	2.0598	2.0573	2.0687	2.0623	2.0663	2.0629
Band gap (eV)	0.947	1.244		1.09		1.134

<sup>1</sup> magnetic moment at only selected site

<sup>2</sup> average value

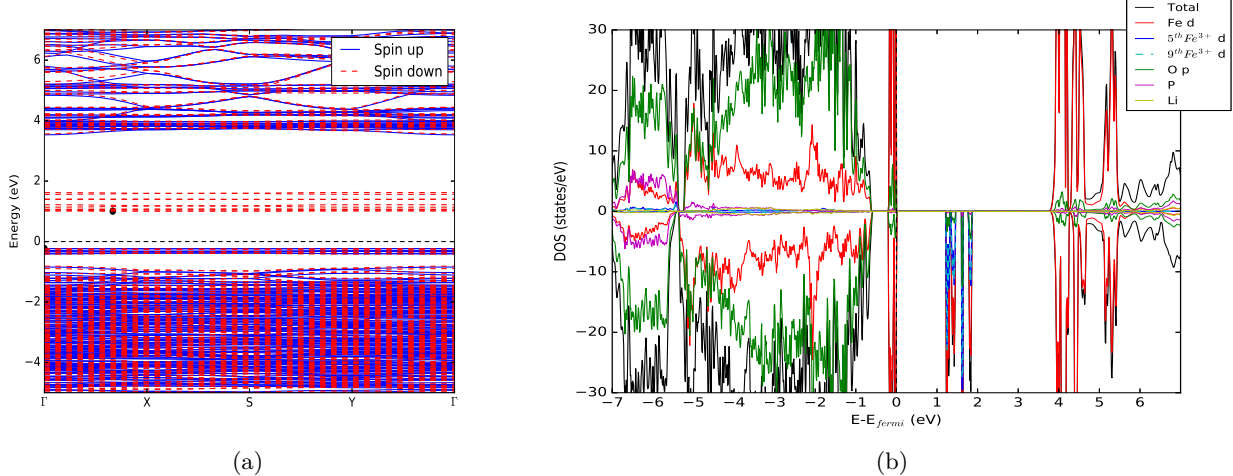


Figure 41: (41a) band structure and (41b) DOS of  $\text{Li}_{14}\text{Fe}_{16}(\text{PO}_4)_{16}$

As summarized in table 11, the cell volume is smaller when doping with Al. In this case, there are two small hole polaron ( $p^+$ ) existing in the system which can be affirmed by magnetic moment and Fe-O bond length. Moreover, the band gap energy is narrower so it can be useful for electronic conductivity. This narrower band gap is dominantly affected by the d orbital of  $\text{Fe}^{2+}$  at VBM and hole polaron state at CBM. Although the previous case also has polaron state, this case has more number of that state so the denser polaron state can reduce band gap.

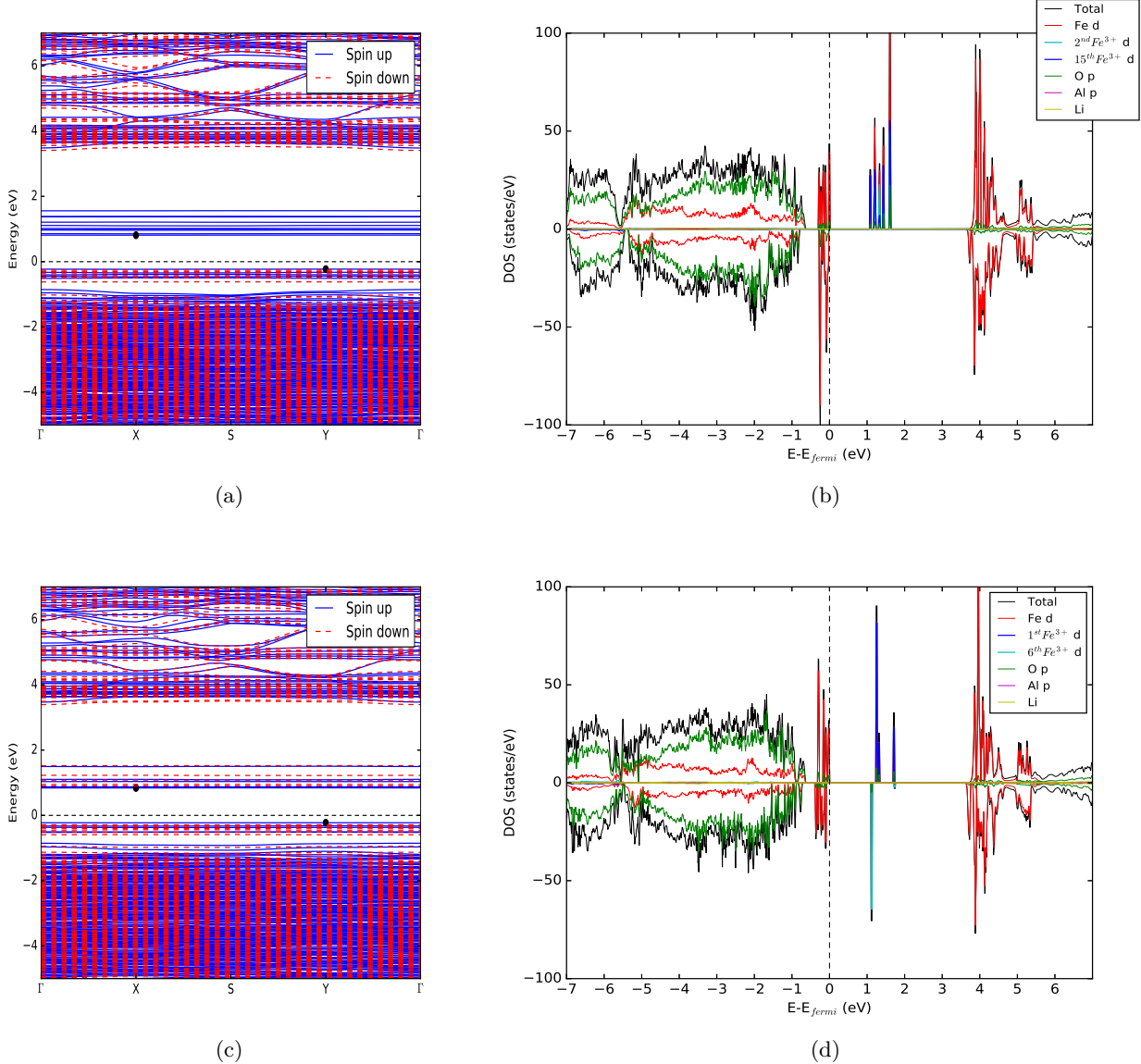


Figure 42: Band structure and density of state: (42a) and (42b) for  $\text{Li}_{13}\text{AlFe}_{15}(\text{PO}_4)_{16}$ , (42c) and (42d) for  $\text{Li}_{12}\text{Al}_2\text{Fe}_{14}(\text{PO}_4)_{16}$ .

**7.5.1.4 Three small hole polarons phase** In this section, we discuss effect of Al dopant on electronic structure and the additional number of lithium vacancy ( $V_{\text{Li}}^-$ ) for creating three small hole polaron. Hence, the formula can be written as  $\text{Li}_{13}\text{Fe}_{16}(\text{PO}_4)_{16}$  for undoped case,  $\text{Li}_{12}\text{AlFe}_{15}(\text{PO}_4)_{16}$  for 6.25% doping, and  $\text{Li}_{11}\text{Al}_2\text{Fe}_{14}(\text{PO}_4)_{16}$  for 12.5% doping. All cases are doped under 3 Li deficient environment. The data is summarized as shown in table below.

All electronic structures are provided by,

Table 12: Calculated values of Al doping and three small hole polarons

Lattice parameters (Å)	undope values	6.25% doping		12.5% doping	
		values	%difference	values	%difference
a	10.3205	10.2853	-0.341	10.2299	-0.878
b	12.0550	12.0156	-0.327	11.9434	-0.926
c	9.5394	9.5494	0.105	9.5747	0.370
volume (Å <sup>3</sup> )	1186.8229	1180.1202	-0.565	1169.726	-1.441
Atom site	5 <sup>th</sup> Fe 6 <sup>th</sup> Fe 9 <sup>th</sup> Fe	1 <sup>st</sup> Fe 6 <sup>th</sup> Fe 14 <sup>th</sup> Fe	2 <sup>nd</sup> Fe 4 <sup>th</sup> Fe 5 <sup>th</sup> Fe		
Magnetic moment <sup>1</sup>	4.296	4.297	4.292	-4.295	4.295
Fe-O bond length(Å)	2.0535	2.0582	2.0645	2.057	2.0687
Band gap (eV)	1.112			1.189	
					1.277

<sup>1</sup> shown only selected site

<sup>2</sup> average value

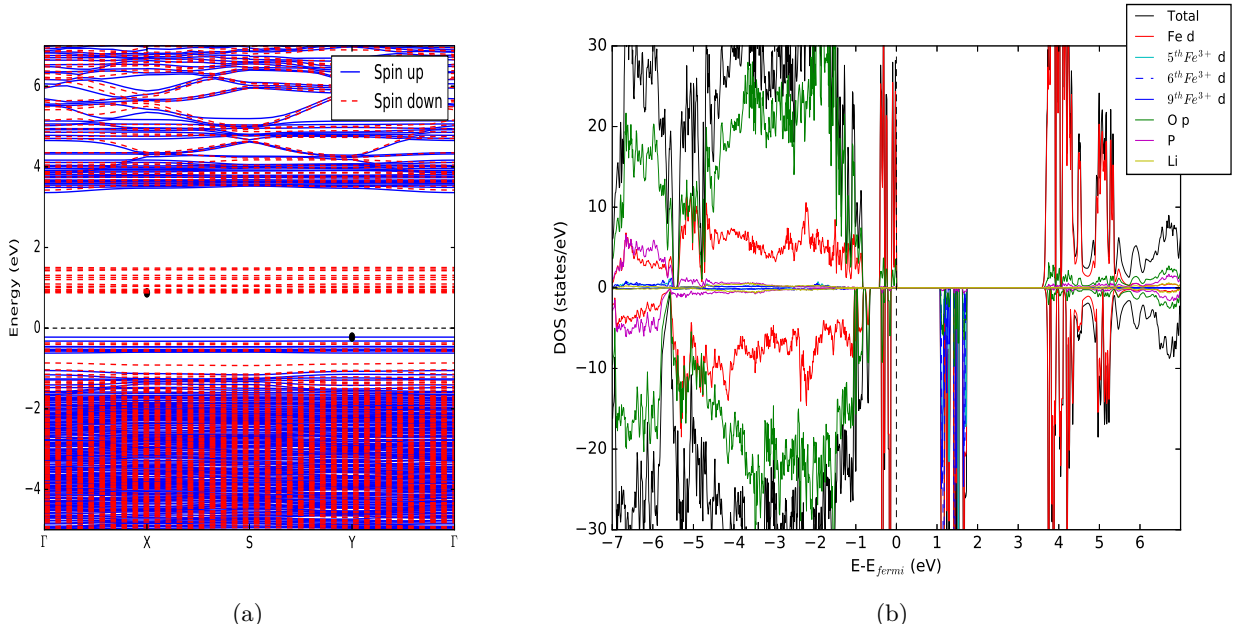


Figure 43: (43a) band structure and (43b) DOS of  $\text{Li}_{13}\text{Fe}_{16}(\text{PO}_4)_{16}$

According to table 12, the cell volumes are smaller in proportional to the doping concentration which satisfies with all previous results. In this case, values of magnetic moment and Fe-O bond length point out the localization of 3 small hole polarons. In the aspect of band gap energy, Al cannot reduce it and the dominant characters are  $\text{Fe}^{2+}$  at VBM and  $\text{p}^+$  state at CBM as seen in fig 44. The larger band gap of Al doping indicates Al cannot improve electronic conductivity.

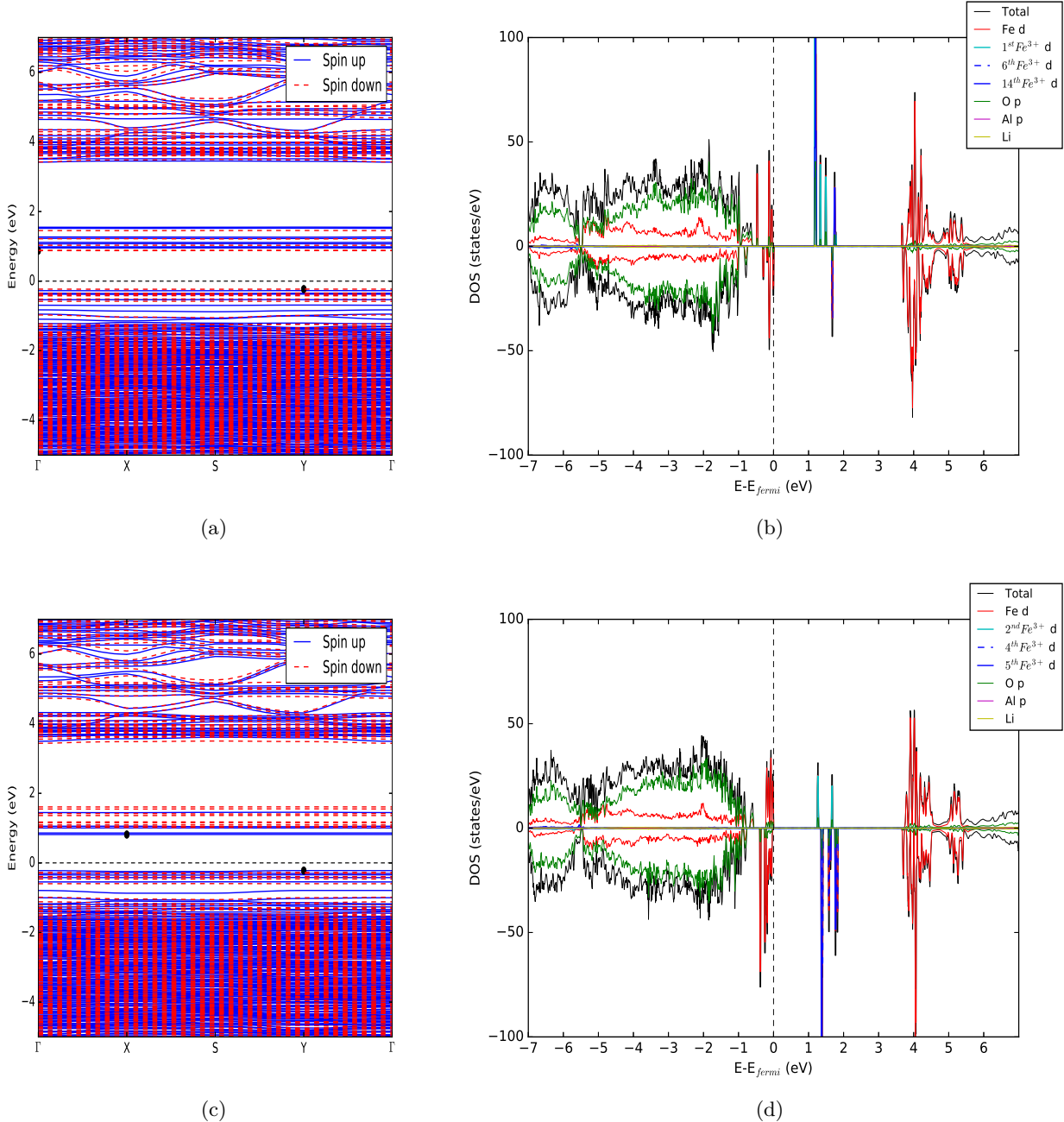


Figure 44: (44a) band structure and (44b) DOS of  $\text{Li}_{12}\text{AlFe}_{15}(\text{PO}_4)_{16}$  and (44c) band structure and (44d) DOS of  $\text{Li}_{11}\text{Al}_2\text{Fe}_{14}(\text{PO}_4)_{16}$

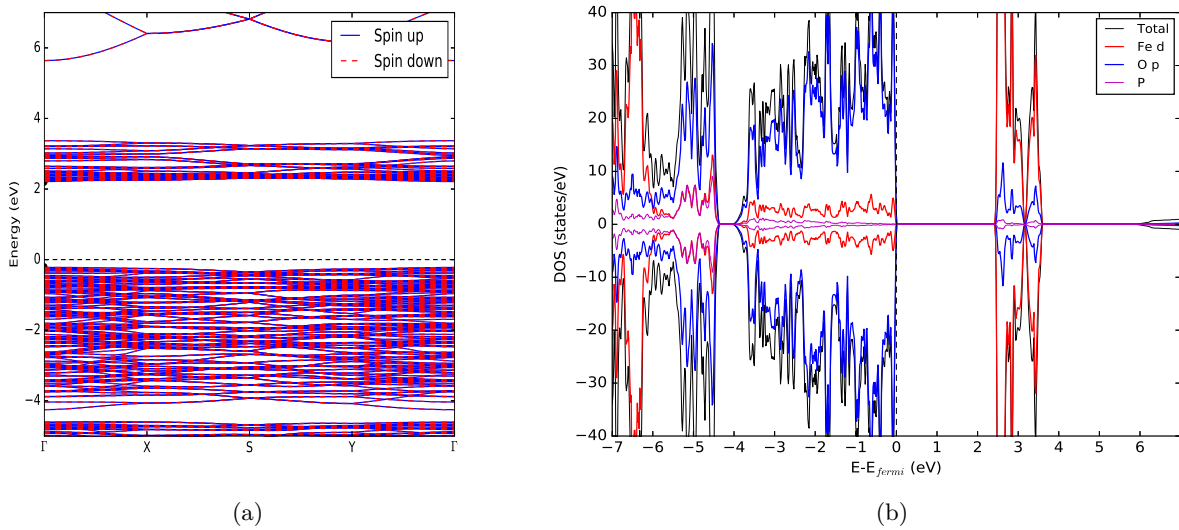
**7.5.1.5 Delithiation phase** In this section, we discuss effect of Al dopant on electronic structure with all Li removed. Chemical formula can be written as  $\text{Fe}_{16}(\text{PO}_4)_{16}$  for undoped case,  $\text{AlFe}_{15}(\text{PO}_4)_{16}$  for 6.25% doping,  $\text{Al}_2\text{Fe}_{14}(\text{PO}_4)_{16}$  for 12.5% doping, and  $\text{AlFe}_3(\text{PO}_4)_4$  for 25% doping. The data is summarized as shown in table below.

All electronic structures are provided by,

Table 13: Calculated values of Al doping

Lattice parameters (Å)	undope unitcell	supercell	6.25% doping values	%difference values	12.5% doping values	%difference values	25% doping values	%difference
a	9.932	9.9051	9.9233	0.184	9.905	0.002	9.853	-0.795
b	5.883	11.6093	11.7468	1.185	11.714	0.899	5.814	-1.173
c	4.859	9.4832	9.6882	2.161	9.666	1.924	4.807	-1.07
volume (Å <sup>3</sup> )	283.921	1090.4863	1129.3266	3.562	1121.472	2.841	275.367	-3.013
Atom site	1 <sup>st</sup> Fe	1 <sup>st</sup> Fe	1 <sup>st</sup> Fe	2 <sup>nd</sup> Fe	1 <sup>st</sup> Fe	2 <sup>nd</sup> Fe	1 <sup>st</sup> Fe	2 <sup>nd</sup> Fe
Magnetic moment <sup>1</sup>	-4.306	-4.308	-4.308	-4.308	-4.305	-4.31	-4.311	4.324
Fe-O bond length(Å)	2.06	2.0332	2.0332	2.0332	2.0516	2.0516	2.06	2.05
Band gap (eV)	2.431	2.447		2.377		2.366		2.341

<sup>1</sup> shown only selected site

<sup>2</sup> average value

 Figure 45: (45a) band structure and (45b) DOS of  $\text{Fe}_{16}(\text{PO}_4)_{16}$ 

As reported in table 13, the cell volume is shortened with the direct proportion to Al concentration. Turning to consider magnetic moment and bond length, even though both data indicate  $\text{Fe}^{3+}$  state, small hole polaron ( $\text{p}^+$ ) does not localize around that  $\text{Fe}^{3+}$  site. As mentioned earlier,  $\text{LiFePO}_4$  has two phases: delithiation and lithiation. It means that the structure and total charge are already stable in this case so the hole polaron does not need to occur for charge compensation. This nonexistence of  $\text{p}^+$  can be ensured by considering band structure and DOS as shown in figure 45 and figure 46. That is, there is no extra state at the conduction band near fermi level. Therefore, the reduction of band gap energy in this case is affected by Al doping only. It shows that the dominant state in valence band turns from d-orbital of  $\text{Fe}^{2+}$  state to p-orbital of O state because all  $\text{Fe}^{2+}$  is oxidized to  $\text{Fe}^{3+}$  which locates at the conduction band. For Al doping, this impurity destroys antiferromagnetic character so there are some states approaching the fermi level more than the pure case. Consequently, band gap energy is narrower.

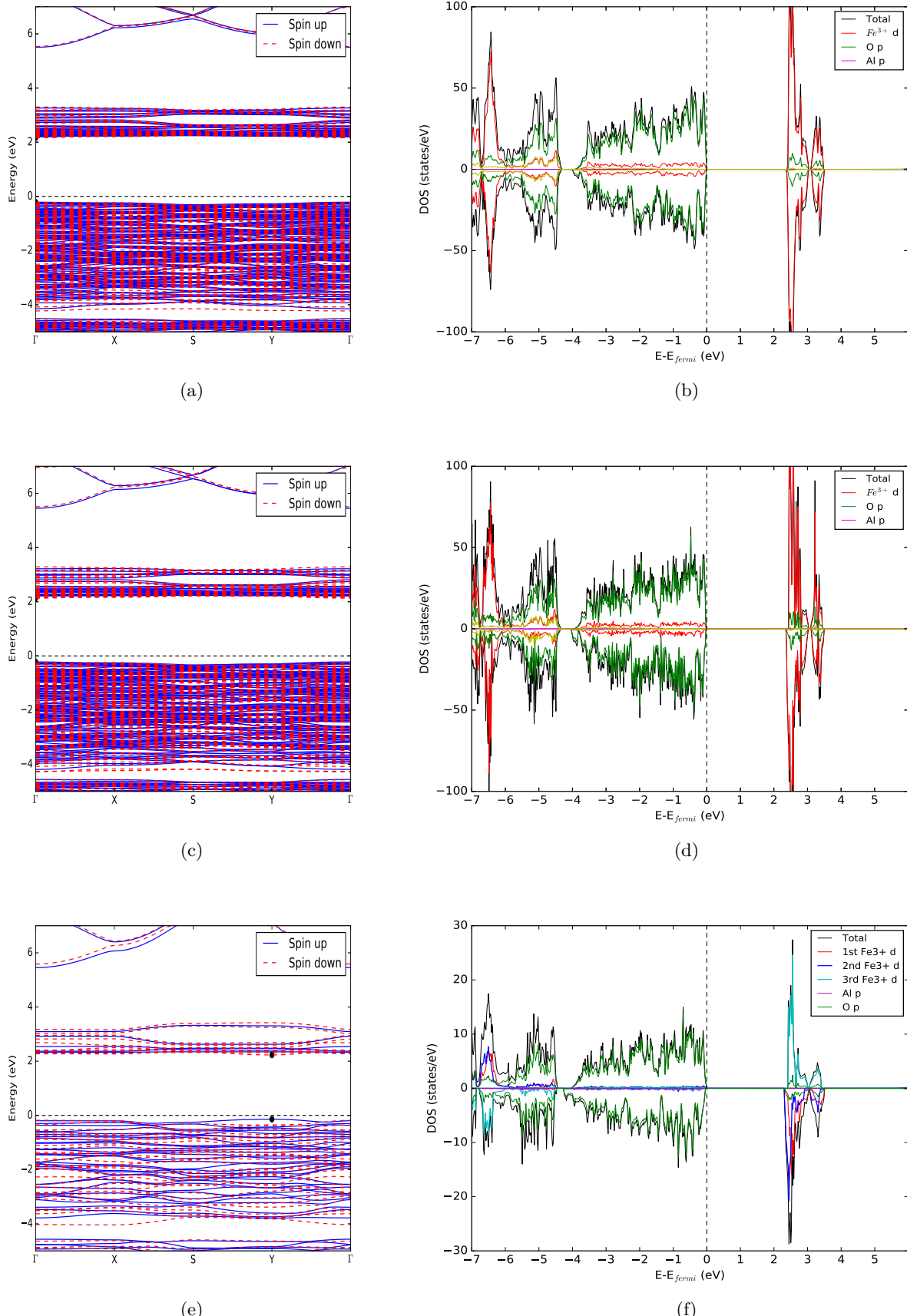


Figure 46: Band structure and density of state: (46a) and (46b) for  $\text{AlFe}_{15}(\text{PO}_4)_{16}$ , (46c) and (46d) for  $\text{Al}_2\text{Fe}_{14}(\text{PO}_4)_{16}$ , and (46e) and (46f) for  $\text{AlFe}_3(\text{PO}_4)_4$ .

**7.5.1.6 Conclusion** For Al doping, we have varied the studies into 5 cases consisting of lithiation, 1 Li deficiency, 2 Li deficiency, 3 Li deficiency, and delithiation cases. All results are illustrated as follows:

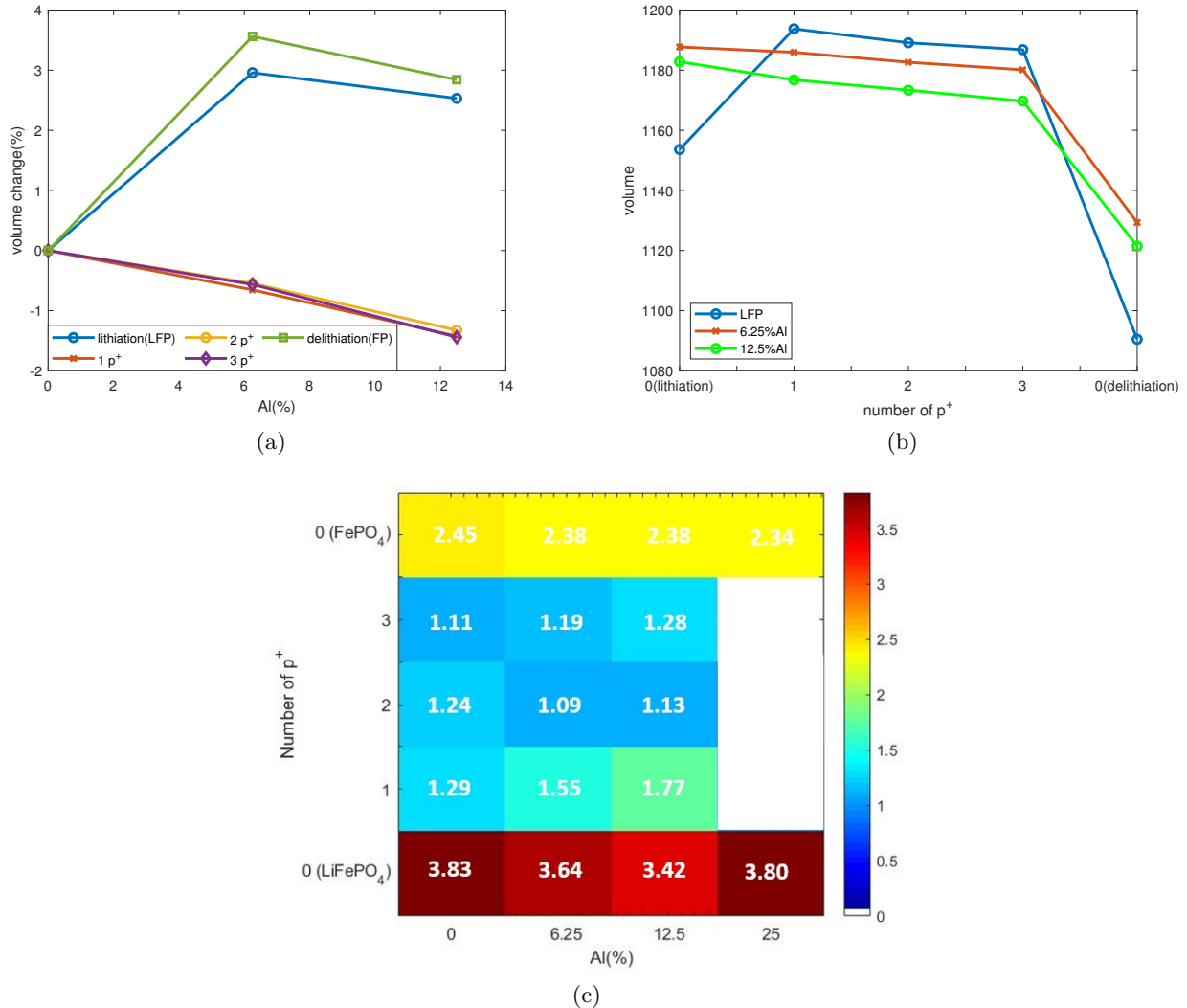


Figure 47: (47a) and (47b) cell volume , (47c) band gap energy

As seen in figure 47a and figure 47b, they are the same data performed in different viewpoints. For figure 47a, it demonstrates that the Al content has a different effect on the structure between two normal phases and Li deficient environment phases. For the first group, volumes in lithiation and delithiation phases are broadened at the first doping due to the effect of both Al dopant and Li vacancy defect. These two impurities result in the reconstruction of the crystal. That is, for the undoped cases  $\text{LiFePO}_4$  and  $\text{FePO}_4$ , whereas Al is substituted at Fe site, Li atom needs removing for charge compensation. Hence, the structure is first affected by both Al dopant and Li vacancy defect. All of which lead to the expansion of cell volume at the first doping. After that, their volumes are smaller because of effect of more Al concentration only. This is obviously different trend especially at the first doping when compared with Li deficiency case. That is, at the second group  $\text{Li}_{16-x}\text{Fe}_{16}(\text{PO}_4)_{16}$  ( $x = 1, 2, 3$ ), the structures are already doped with Li vacancy defect. Thus, after doping with Al, the structure is affected by only Al dopant which has smaller ionic radius than that of Fe. This causes the reduction of volume corresponding to Al concentration. For figure 47b, it shows the volume transformation resulted from Li vacancy only. It indicates that when the undoped

case LiFePO<sub>4</sub> is doped at the first time, the volume is expanded corresponding to the previous result. Then, the volume will be smaller due to removal of Li. However, for the doped cases, at the lithiation phase both are initially doped by Al and Li vacancy so when Li is more removed, it brings about the smaller volume. In the aspect of band gap as shown in figure 47c, small hole polaron localized during the Li deficient environment can reduce band gap obviously because the hole polaron state always exists in the conduction band near fermi level. In addition, Al dopant can also decrease the band gap especially for the lithiation and delithiation phases of 6.25% and 12.5% but for Li deficiency Al seems to be unable to reduce gap. Thus, Al will make useful contribution only for lithiation, delithiation, and 2p<sup>+</sup> cases. Due to reduction of band gap, it may help electron hop more easily and then improve electronic conductivity.

### 7.5.2 Effect of Titanium (Ti<sup>4+</sup>) on electronic structure

**7.5.2.1 Lithiation phase** In this section, we discuss effect of Ti dopant on electronic structure but the number of lithium vacancy ( $V_{Li}^-$ ) is implemented only for charge balance. Thus, all structures can be expressed as Li<sub>16</sub>Fe<sub>16</sub>(PO<sub>4</sub>)<sub>16</sub> for undoped case, Li<sub>14</sub>TiFe<sub>15</sub>(PO<sub>4</sub>)<sub>16</sub> for 6.25% doping case, Li<sub>12</sub>Ti<sub>2</sub>Fe<sub>14</sub>(PO<sub>4</sub>)<sub>16</sub> for 12.5% doping case, and Li<sub>2</sub>TiFe<sub>3</sub>(PO<sub>4</sub>)<sub>4</sub> for 25% doping case. The data is summarized as shown below.

Table 14: Calculated values of Ti doping

Parameter	Exp <sup>1</sup> [Ref.[58]]		Pure		6.25%doping		12.5%doping		25%doping	
	pure	doping	unitcell	supercell	value	%change	value	%change	value	%change
a	10.3148(1)	10.3233(2)	10.416	10.266	10.376	1.08	10.351	0.827	10.3166	-0.95
b	6.0009(7)	6.0031(8)	6.062	11.990	12.111	1.004	12.094	0.865	6.0288	-0.55
c	4.6897(5)	4.6969(7)	4.745	9.372	9.547	1.860	9.597	2.398	4.8716	2.67
V	290.28(5)	291.077(7)	299.61	1153.62	1199.67	3.992	1201.30	4.133	302.884	1.093
Atom	-		1 <sup>st</sup> Fe	1 <sup>st</sup> Fe	1 <sup>st</sup> Fe		1 <sup>st</sup> Fe		1 <sup>st</sup> Fe	
Moment <sup>2</sup>	-		3.76 $\mu_B$	3.77 $\mu_B$		-3.77 $\mu_B$		-3.77 $\mu_B$		3.77 $\mu_B$
Fe-O(Å)	-		2.16	2.16		2.15		2.17		2.18
Gap(eV)	-		3.827		1.046		1.101		0.973	

<sup>1</sup> Experiment 1% doping

<sup>2</sup> Magnetic moment ( $\mu_B$ )

After LiFePO<sub>4</sub> is doped with Titanium, the cell volume slightly expands corresponding to the Ti concentration. Up to 25% doping implemented in unit cell, the volume turns into decreasing because in this case there are more number of lithium vacancy in the structure. Then, values of magnetic moment and Fe-O bond length indicate that there is no localization of small hole polaron. Therefore, band gap now is influenced by only Ti doping as shown in figure 48. According to band structure and density of states of all cases, band gap is reduced due to the extra state of d-orbital of Ti existing near fermi level at the conduction band. This is different from Al doping cases since the normal orbital that dominates around fermi level of LiFePO<sub>4</sub> structure is d-orbital. Because Al has only s and p orbital, that is why the dominant atom is still Fe atom.

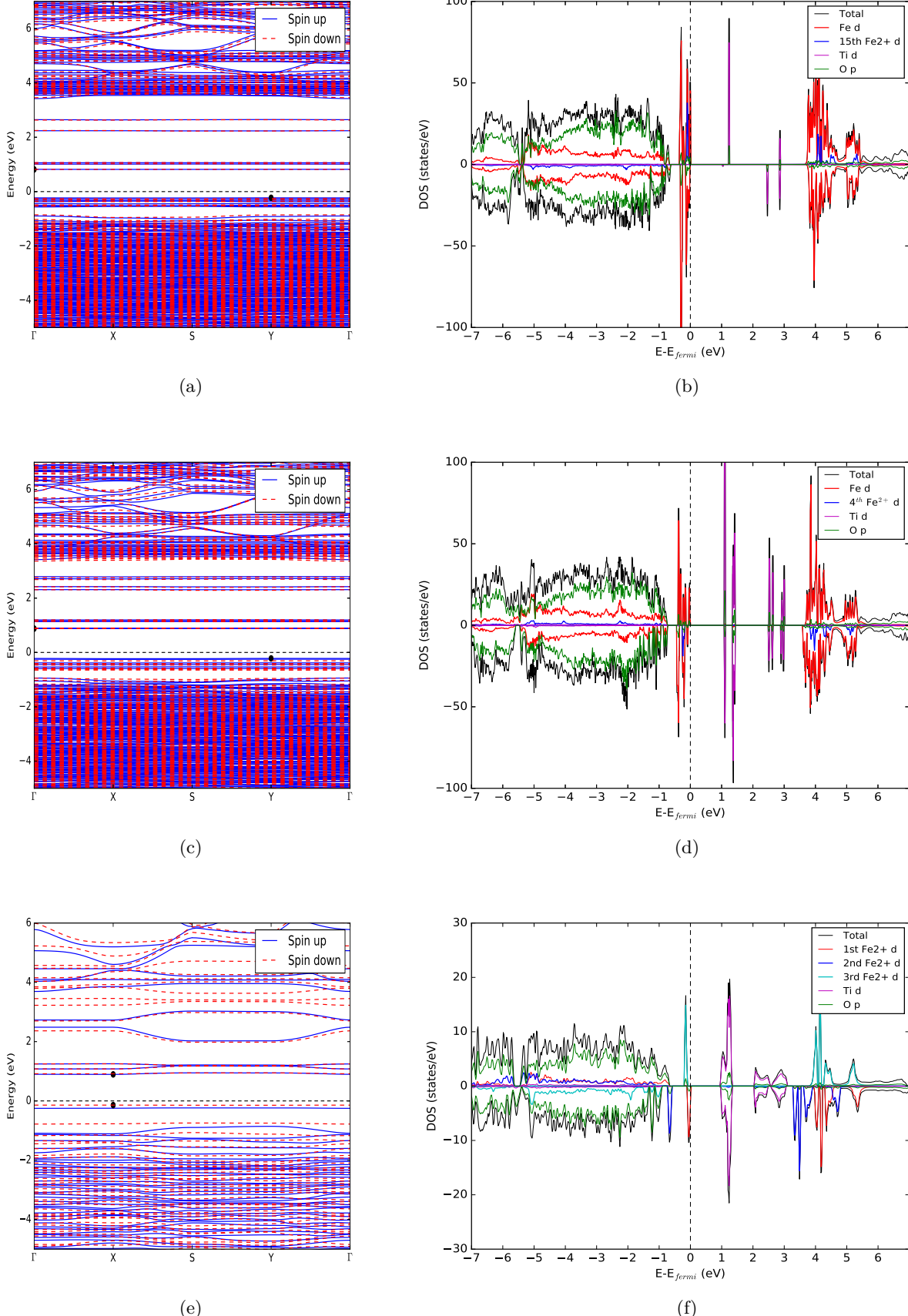


Figure 48: Band structure and density of state: (48a) and (48b) for  $\text{Li}_{14}\text{TiFe}_{15}(\text{PO}_4)_{16}$ , (48c), (48d) for  $\text{Li}_{12}\text{Ti}_2\text{Fe}_{14}(\text{PO}_4)_{16}$ , and (49a) and (49b) for  $\text{Li}_2\text{TiFe}_3(\text{PO}_4)_4$

**7.5.2.2 One small hole polaron phase** In this section, we discuss effect of Ti dopant on electronic structure and the additional number of lithium vacancy ( $V_{Li}^-$ ) for creating one small hole polaron. In other words, this phase is in Li deficient environment as follows:  $Li_{15}Fe_{16}(PO_4)_{16}$  for undoped case,  $Li_{13}TiFe_{15}(PO_4)_{16}$  for 6.25% doping and  $Li_{11}Ti_2Fe_{14}(PO_4)_{16}$  for 12.5% doping case. All of these are also doped under 1 Li atom deficiency. The data is summarized as shown in table below.

Table 15: Calculated values of combined Ti doping and one Li deficiency

Lattice parameters	Undope		6.25% doping		12.5% doping	
	unitcell	supercell	values	%difference	values	%difference
a(Å)	10.326	10.3727	10.3563	-0.157	10.3212	-0.497
b(Å)	6.027	12.1073	12.08	-0.225	12.07	-0.311
c(Å)	4.788	9.5056	9.571	0.693	9.617	0.338
Volume (Å <sup>3</sup> )	297.957	1193.7516	1197.418	0.307	1198.035	0.359
Atom site	3 <sup>rd</sup> Fe	10 <sup>th</sup> Fe	1 <sup>st</sup> Fe	15 <sup>th</sup> Fe	1 <sup>st</sup> Fe	4 <sup>th</sup> Fe
Mag moment( $\mu_B$ ) <sup>1</sup>	4.295	4.296	-3.77	-4.288	-3.772	4.291
Fe-O length(Å)	2.05	2.0598	2.179	2.071	2.175	2.07
Band gap (eV)	1.024	1.288	1.156		1.189	

<sup>1</sup> magnetic moment at only selected site

<sup>2</sup> average value

As reported in table 15, the volume is changed with the same tendency as the lithiation phase. However, magnetic moment and bond length point out the existence of small hole polaron. In the aspect of band gaps, band gaps are changed because of d-orbital of Ti. However, when Ti is doped more and more, band gap turns into increasing because the dominant state becomes d-orbital of small hole polaron instead of Ti. Normally, polaron state exists farther from the Fermi level than Ti state so this is reason why band gap is wider.

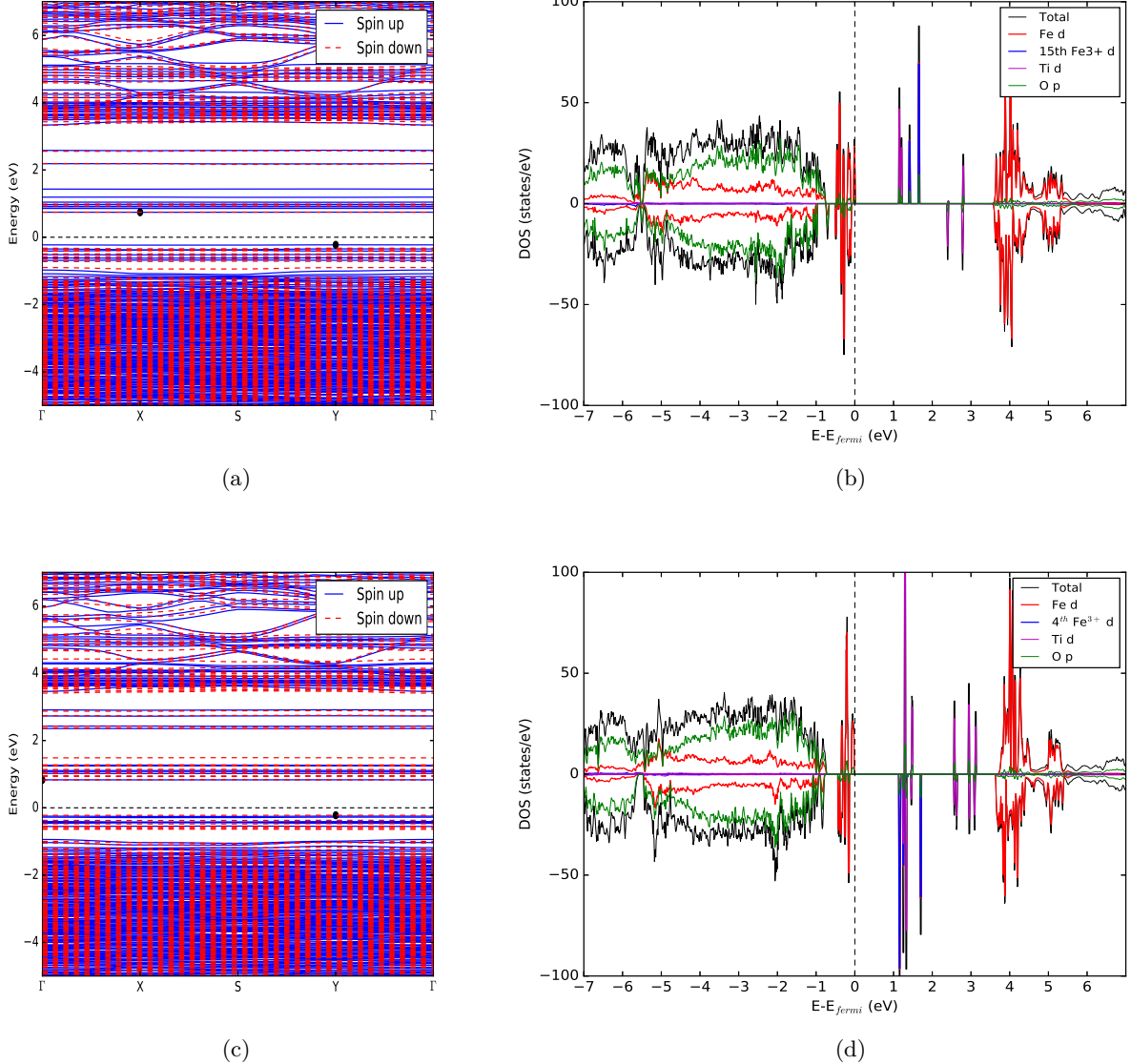


Figure 49: Band structure and density of state: (49a) and (49b) for  $\text{Li}_{13}\text{TiFe}_{15}(\text{PO}_4)_{16}$  and (49c) and (49d) for  $\text{Li}_{11}\text{Ti}_2\text{Fe}_{14}(\text{PO}_4)_{16}$ .

**7.5.2.3 Two small hole polarons phase** In this section, we discuss effect of Ti dopant on electronic structure and the additional number of lithium vacancy ( $V_{Li}^-$ ) for creating two small hole polarons. Thus, the structure can be written as  $\text{Li}_{14}\text{Fe}_{16}(\text{PO}_4)_{16}$  for undoped case,  $\text{Li}_{12}\text{TiFe}_{15}(\text{PO}_4)_{16}$  for 6.25% doping, and  $\text{Li}_{10}\text{Ti}_2\text{Fe}_{14}(\text{PO}_4)_{16}$  for 12.5% doping. All of these cases are doped under two Li deficient environment. The data is summarized as shown in table below.

All electronic structures are provided by,

Table 16: Calculated values of combined Ti doping and two Li deficiency

Lattice parameters	Undope		6.25% doping		12.5% doping	
	unitcell	supercell	values	%difference	values	%difference
a(Å)	10.141	10.3408	10.339	-0.02	10.279	-0.599
b(Å)	5.946	12.0785	12.073	-0.046	12.058	-0.171
c(Å)	4.811	9.5206	9.574	0.56	9.634	1.194
volume (Å <sup>3</sup> )	290.053	1189.1267	1194.989	0.493	1194.042	0.413
Atom site	5 <sup>th</sup> Fe	9 <sup>th</sup> Fe	1 <sup>st</sup> Fe	15 <sup>th</sup> Fe	3 <sup>rd</sup> Fe	13 <sup>th</sup> Fe
Mag moment <sup>1</sup>	4.294	4.294	-4.289	-4.297	4.3	-4.293
Fe-O length(Å)	2.0598	2.0573	2.0679	2.0561	2.057	2.057
Band gap (eV)	0.947	1.244	0.979		1.145	

<sup>1</sup> magnetic moment at only selected site

<sup>2</sup> average value

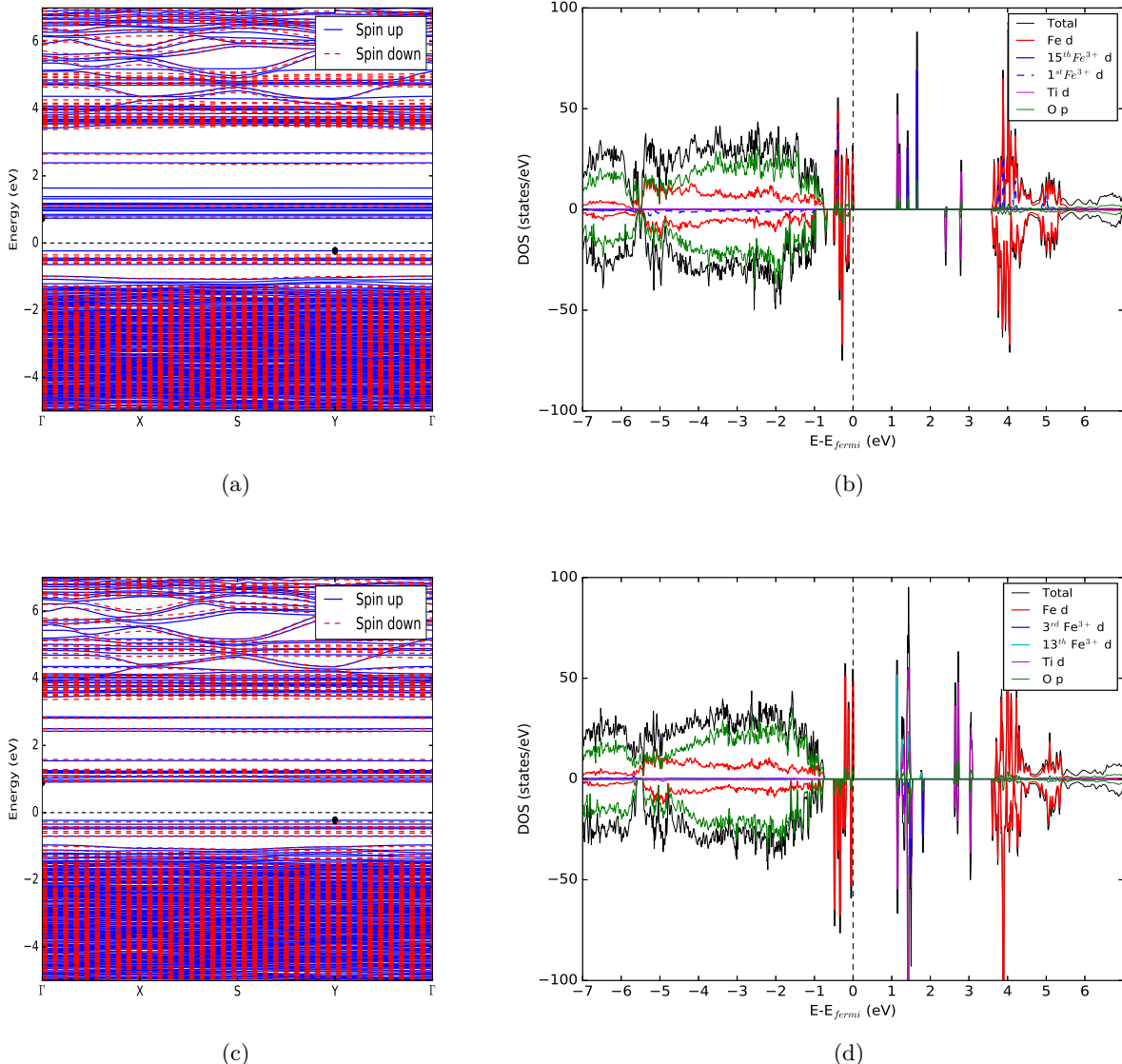


Figure 50: Band structure and density of state: (50a) and (50b) for  $\text{Li}_{12}\text{TiFe}_{15}(\text{PO}_4)_{16}$  and (50c) and (50d) for  $\text{Li}_{10}\text{Ti}_2\text{Fe}_{14}(\text{PO}_4)_{16}$ .

As reported in table 16, the volume is smaller corresponding to the Ti concentration. However, magnetic moment and bond length point out the existence of small hole polaron. In the aspect of band gaps, this phase has smaller band gap when doping with Ti because the dominant contribution near fermi level is Ti state as shown in figure 50. However when it is doped with more Ti, polaron state overcomes Ti state which makes band gap larger.

**7.5.2.4 Three small hole polarons phase** In this section, we discuss effect of Ti dopant on electronic structure and the additional number of lithium vacancy ( $V_{Li}^-$ ) for creating three small hole polaron. Hence, the formula can be written as  $Li_{13}Fe_{16}(PO_4)_{16}$  for undoped case,  $Li_{11}TiFe_{15}(PO_4)_{16}$  for 6.25% doping, and  $Li_9Ti_2Fe_{14}(PO_4)_{16}$  for 12.5% doping. All cases are doped under 3 Li deficient environment. The data is summarized as shown in table below.

Table 17: Calculated values of Ti doping and three small hole polaron

Lattice parameters (Å)	undope		6.25% doping		12.5% doping	
	values	%difference	values	%difference	values	%difference
a	10.3205		10.3049	-0.152	10.2665	-0.523
b	12.0550		12.0482	-0.057	12.0401	-0.124
c	9.5394		9.5834	0.461	9.6443	1.100
volume (Å <sup>3</sup> )	1186.8229		1189.7686	0.248	1192.0433	0.440
Atom site	5 <sup>th</sup> Fe	6 <sup>th</sup> Fe	9 <sup>th</sup> Fe	1 <sup>st</sup> Fe	6 <sup>th</sup> Fe	14 <sup>th</sup> Fe
Magnetic moment <sup>1</sup>	4.296	4.297	4.292	-4.292	4.296	4.294
Fe-O bond length(Å)	2.0535	2.0582	2.0645	2.0664	2.0753	2.0574
Band gap (eV)	1.112				1.156	
						1.067

<sup>1</sup> shown only selected site

<sup>2</sup> average value

According to table 17, cell volume is expanded when doped with Ti atom. Both magnetic moment and bond length also indicate the localization of three small hole polarons which shows at the conduction band from density of state. However, Ti atom is dominant atom in this case which makes band gap lower.

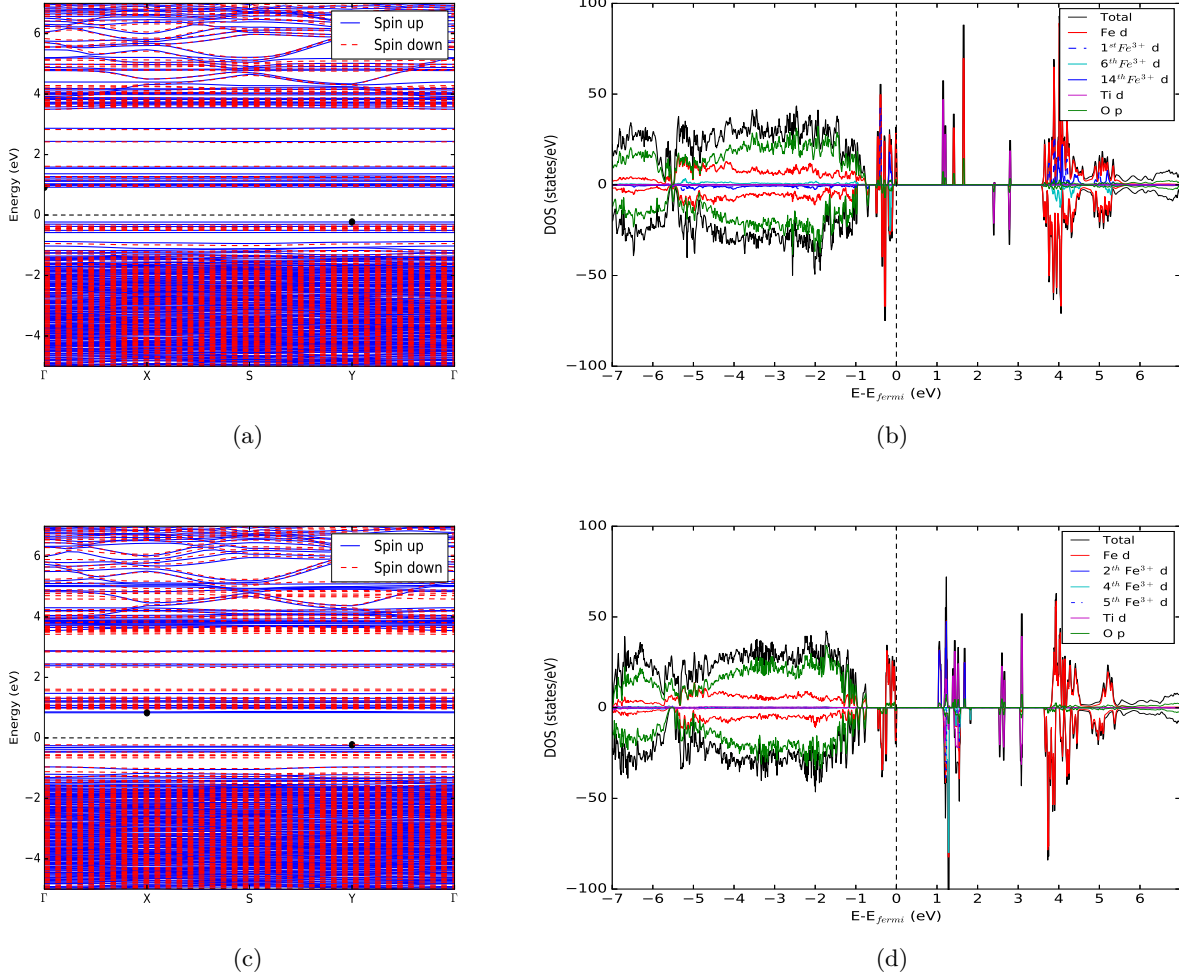


Figure 51: Band structure and density of state: (51a) and (51b) for  $\text{Li}_{11}\text{TiFe}_{15}(\text{PO}_4)_{16}$  and (51c), (51d) for  $\text{Li}_9\text{Ti}_2\text{Fe}_{14}(\text{PO}_4)_{16}$

**7.5.2.5 Delithiation phase** In this section, we discuss effect of Ti dopant on electronic structure with all Li removed. Chemical formula can be written as  $\text{Fe}_{16}(\text{PO}_4)_{16}$  for undoped case,  $\text{TiFe}_{15}(\text{PO}_4)_{16}$  for 6.25% doping,  $\text{Ti}_2\text{Fe}_{14}(\text{PO}_4)_{16}$  for 12.5% doping, and  $\text{TiFe}_3(\text{PO}_4)_4$  for 25% doping. The data is summarized as shown in table below.

Table 18: Calculated values of Ti doping

Lattice parameters (Å)	undope		6.25% doping		12.5% doping		25% doping	
	unitcell	supercell	values	%difference	values	%difference	values	%difference
a	9.932	9.9051	9.9586	0.540	9.9679	0.634	10.0006	0.691
b	5.883	11.6093	11.8160	1.781	11.8490	2.063	5.9167	0.573
c	4.859	9.4832	9.7322	2.625	9.7602	2.921	4.8959	0.759
volume (Å <sup>3</sup> )	283.921	1090.4863	1145.1953	5.017	1152.757	5.710	289.6843	2.030
Atom site	1 <sup>st</sup> Fe	1 <sup>st</sup> Fe	1 <sup>st</sup> Fe	8 <sup>th</sup> Fe	1 <sup>st</sup> Fe	8 <sup>th</sup> Fe	2 <sup>nd</sup> Fe	3 <sup>rd</sup> Fe
Magnetic moment <sup>1</sup>	-4.306	-4.308	-4.306	3.77	-4.306	3.77	-4.300	3.778
Fe-O bond length(Å)	2.06	2.0332	2.0528	2.1631	2.0528	2.1631	2.06	2.17
Band gap (eV)	2.431	2.447	0.979		1.111		0.937	

<sup>1</sup> shown only selected site

<sup>2</sup> average value

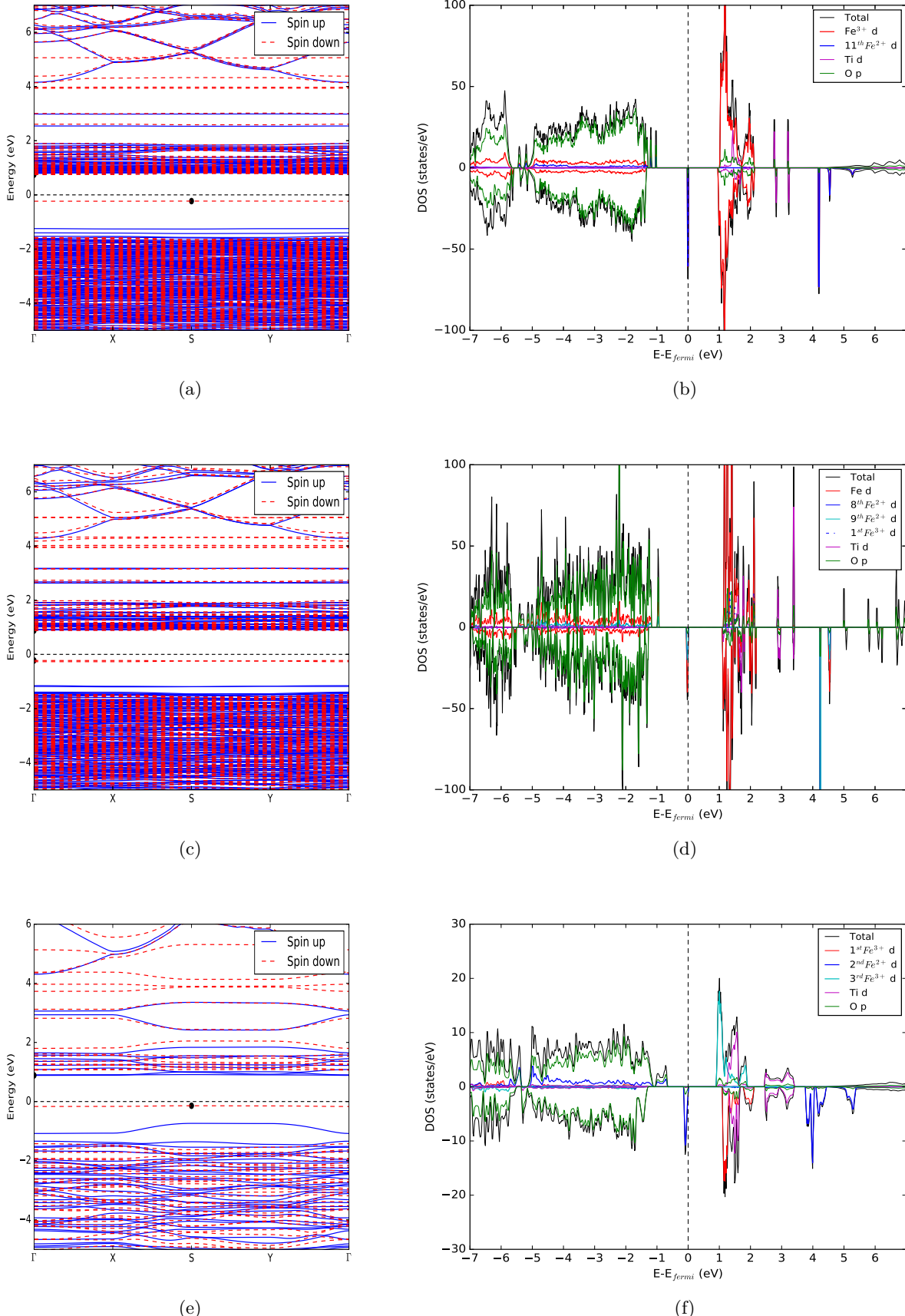


Figure 52: Band structure and density of state: (52a) and (52b) for  $\text{TiFe}_{15}(\text{PO}_4)_{16}$ , (52c) and (52d) for  $\text{Ti}_2\text{Fe}_{14}(\text{PO}_4)_{16}$ , and (52e) and (52f) for  $\text{TiFe}_3(\text{PO}_4)_4$

For the last phase, the tendency of cell volume is consistent with all above results. Normally, all Fe atoms in the undoped case in this phase have oxidation number  $3^+$  due to nonexistence of Li atom in the structure. However, for this Ti dopant, it has at least two Fe atoms which still has oxidation number  $2^+$  for charge balance. This is proven by the values of both magnetic moment and bond length. The presence of  $\text{Fe}^{2+}$  causes the reduction of band gap because there is  $\text{Fe}^{2+}$  state located at valence band near fermi level. Moreover, it also has  $\text{Fe}^{3+}$  state located at the conduction band near fermi level. These two occurring states are accidentally similar to the two small hole polaron case. That is why band gap is highly reduced.

**7.5.2.6 Conclusion** For Ti doping, we have varied the studies into 5 cases consisting of lithiation, 1 Li deficiency, 2 Li deficiency, 3 Li deficiency, and delithiation cases. All results are illustrated as follows:

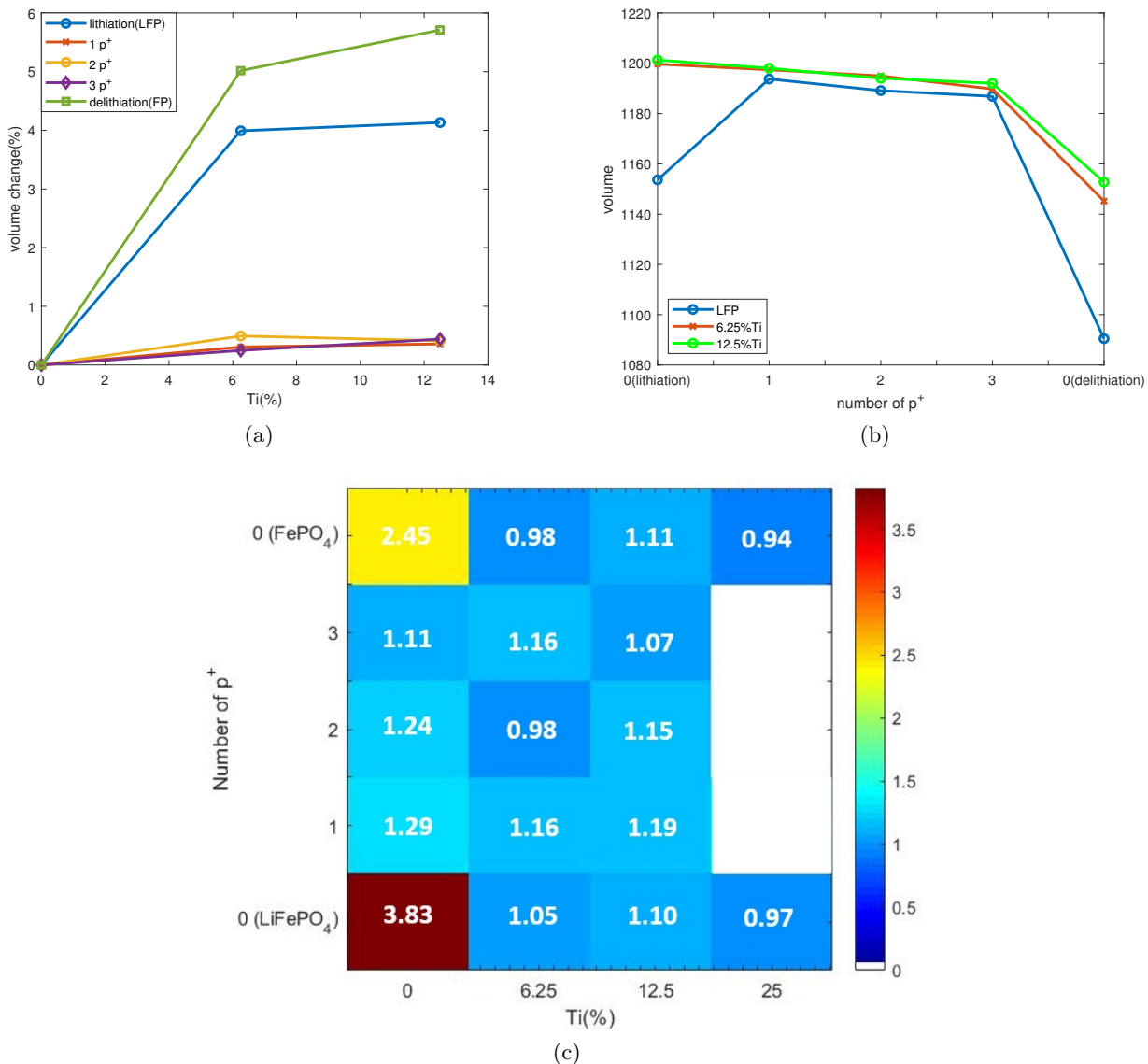


Figure 53: (53a) and (53b) cell volume , (53c) band gap energy

The volume changes shown in figure 53a have the same tendency as the Al doping case. That is, the volume will expand at the first doping of lithiation and delithiation phases. The reason for that behavior is that it has combination of Ti and lithium vacancy doping. After that it will slightly

enlarge due to Ti dopant but it will get smaller when doped 25% concentration. However, for the Li-deficient phases, although the crystal is in 0% Ti doping, it is already doped with lithium vacancy for charge balance. Therefore, when it is doped with Ti, the volume in all cases will slightly enlarge and get smaller at 25% doping. Then, turning to consider in the aspect of volume changes from lithium vacancy only as shown in figure 53b. The results illustrate differently with Al doping. The volume of structure doped with Ti will remain higher than the undoped case. This behaviour obviously results from Ti doping so it may be beneficial for  $\text{Li}^+$  hopping due to the wider space. This will be proven by energy barriers from NEB calculation again. Eventually, in the aspect of band gap, Ti can reduce its gap obviously. Even in the low concentration of Ti the band gap is decreased from around 3.8 eV to only 1.046 eV in case of delithiation phase (zero small hole polaron). This means that the reduction of band gap is directly affected by d orbital of Ti doping. This includes case of presence of small hole polaron. That is, Ti doping is still a dominant state for band gap. However, when Ti is doped with more concentration, band gap is wider because the polaron state makes Ti state farther from fermi level and some case it becomes the dominant state. In conclusion, Ti with 6.25% concentration provides smallest band gap energy and it is also true in almost all phases.

## 7.6 Effect of supervalent cation doping and Li deficient environment on phase stability

As discussed earlier, our studies are divided into 3 cases: undoped case, supervalent cation doping ( $\text{Al}^{3+}$ ,  $\text{Ti}^{4+}$ ,  $\text{Zr}^{4+}$ , and  $\text{Nb}^{5+}$ ) case, and supervalent cation with Li deficiency case. Therefore, it is necessary to investigate stability after doping. In order to do so, formation energy is applied as following.

Table 19: Calculated formation energy  $E_F$  (eV/formula unit(f.u.))

Dopants	$E_F(Li_{1-(n-2)x}M_x^{n+}Fe_{1-x}PO_4)$			$a = 0.0625$	$a = 0.125$	$a = 0.1875$
	$\text{Al}^{3+}$	$6.25\%$	$-0.1652$			
$12.5\%$		$-0.3099$		$0.2080$	$0.4086$	$0.6344$
$\text{Ti}^{4+}$						
$6.25\%$		$-0.1893$		$0.2269$	$0.4374$	$0.6480$
$12.5\%$		$-0.3926$		$0.2093$	$0.4062$	$0.6175$

For Al and Ti doping, the negative formation energy as shown in table 19 indicates that although  $\text{LiFePO}_4$  is doped with any concentration of Al and Ti, the structure is still stable. In other words,  $\text{LiFePO}_4$  with Al and Ti dopants can be synthesized. However, in Li deficient environment case, formation energy provides positive values in all number of Li removal which refer to instability of the structure. It is rational because these phases ( $a = 0.0625, 0.125, 0.1875$ ) are actually the intermediate phases of Li battery which mean that Li ion and polaron are hopping. This instability confirms the behaviour of charge carrier diffusion. In addition, It also makes useful for the structure. That is, if the structure has more instability, the structure prefers to transform to another phase more quickly and may improve the conductivity by faster diffusion.

## 8 Conclusion

The conductivity in  $\text{LiFePO}_4$  is weak as revealed by a large band gap. Our results indicate that this large band gap is mainly contributed by the  $d$ -orbital of the Fe atom which is consistent with other results available in literature. This large band gap can be reduced by several possible supervalent cation doping. Each impurity has a different effect on the band gap. That is, for the atom that has the  $p$ -orbital at maximum such as Al, the lithiation and delithiation phases are not much improved because the only  $d$ -orbital can make contribution to the state near the Fermi level. However, the band

gap is much reduced if it is doped in Li-deficient environment because there is localization of small hole polaron existing near the Fermi level. On the other hand, for atom that has the *d*-orbital at maximum, both lithiation and delithiation phases have much narrower band gaps. Moreover, when doping in Li deficiency, the extra hole polaron state can also decrease the band gap. Thus far, all of our results now have been concentrated on only the aspect of the band gap reduction which can predict the improvement only in case of the electronic conductivity. Although doping with those impurities (Al, Ti, Zr, Nb) had already been proven about the ability for improving the ionic conductivity, our work still requires the NEB calculation to confirm the results in both electronic and ionic conductivities and make our results much stronger and more comprehensive.

Consequently, the remaining work will be focused on doping with Zr and Nb. After that the most crucial parameter is energy barrier of Li and polaron hopping. Therefore, for our work, it is essential to implement NEB calculation in order to attain the desired results.

## 9 Proposed Research Plan/Schedule

Topic of research	Schedule
<b>Simulation and Data Analysis</b> <ul style="list-style-type: none"> <li>• Electronic structure investigation of Al dopant</li> <li>• Nudge elastic band calculation of Al dopant</li> <li>• Electronic structure investigation of Ti dopant</li> <li>• Nudge elastic band calculation of Ti dopant</li> <li>• Electronic structure investigation of Zr dopant</li> <li>• Nudge elastic band calculation of Zr dopant</li> <li>• Electronic structure investigation of Nb dopant</li> <li>• Nudge elastic band calculation of Nb dopant</li> </ul>	June 2019 - February 2020 (9 months)
<b>Short-term research project at JAIST, Japan</b> <ul style="list-style-type: none"> <li>• Electronic structure of 3.125% doping</li> <li>• Nudge elastic band calculation of 3.125% doping with extra hopping trajectories</li> </ul>	March - September 2020 (6 months)
<b>Theoretical study</b> <ul style="list-style-type: none"> <li>• Data comparison and conclusion</li> <li>• Thesis writing</li> </ul>	October 2020 (1 month)
<b>Thesis Defense</b> <ul style="list-style-type: none"> <li>• Progress Report</li> <li>• Thesis Examination</li> </ul>	November 2020

## 10 Output

1. Understanding of roles and mechanism of impurities and defects on ionic and electronic conductivities deeper, which will play crucial roles for improving Li battery technology.
2. If doping with both impurity and Li-deficient environment can enhance the number of  $\text{Fe}^{3+}$  and  $\text{V}_{\text{Li}}^-$  as hypothesized, it will be one of approaches to augment efficiency of ionic and electronic conductivities.

3. Knowledge related to first-principle methods to investigate lattice structure, electronic structure and other properties in materials can be applied to design Li battery and other systems.

## 11 Acknowledgement

All authors acknowledge the High Performance Computing (HPC) unit at the Synchrotron Light Research Institute (SLRI) for computational resources. Chanaprom Cholsuk is grateful to the Development and Promotion of Science and Technology Talent project (DPST) for a scholarship to study at Mahidol University. Pimsiree Suwanna would like to thank the Ministry of Science young research grant for this project.

## References

- [1] A. K. Padhi. "Phospho-olivines as Positive-Electrode Materials for Rechargeable Lithium Batteries". In: *Journal of The Electrochemical Society* 144.4 (1997), p. 1188. ISSN: 00134651. DOI: 10.1149/1.1837571. URL: <http://jes.ecsdl.org/cgi/doi/10.1149/1.1837571>.
- [2] J.-M. Tarascon and M. Armand. "Issues and challenges facing rechargeable lithium batteries". In: *Nature* 414.6861 (Nov. 2001), pp. 359–367. ISSN: 0028-0836. DOI: 10.1038/35104644. URL: <http://www.nature.com/articles/35104644>.
- [3] J. Gaubicher. "Li/ $\beta$ -VOPO<sub>4</sub>: A New 4 V System for Lithium Batteries". In: *Journal of The Electrochemical Society* 146.12 (1999), p. 4375. ISSN: 00134651. DOI: 10.1149/1.1392646.
- [4] N. Ravet. "Improved iron based cathode material". In: *Proceedings of the Electrochemical Society Fall Meeting , Honolulu, HI, Electrochemical Society: Pennington, NJ* 127 (Oct. 1999).
- [5] H. Huang, S.-C. Yin, and L. F. Nazar. "Approaching Theoretical Capacity of LiFePO<sub>4</sub> at Room Temperature at High Rates". In: *Electrochemical and Solid-State Letters* 4.10 (2001), A170. ISSN: 10990062. DOI: 10.1149/1.1396695.
- [6] Zhou Xin-wen et al. "Synthesis, characterization and properties of LiFePO<sub>4</sub>/C cathode material". In: *Wuhan University Journal of Natural Sciences* 10.5 (Sept. 2005), pp. 909–912. ISSN: 1007-1202. DOI: 10.1007/BF02832437. URL: <http://link.springer.com/10.1007/BF02832437>.
- [7] C. Delacourt et al. "Size Effects on Carbon-Free LiFePO<sub>4</sub> Powders". In: *Electrochemical and Solid-State Letters* 9.7 (2006), A352. ISSN: 10990062. DOI: 10.1149/1.2201987. URL: <http://esl.ecsdl.org/cgi/doi/10.1149/1.2201987>.
- [8] Sung Yoon Chung, Jason T. Bloking, and Yet Ming Chiang. "Electronically conductive phospho-olivines as lithium storage electrodes". In: *Nature Materials* 1.2 (2002), pp. 123–128. ISSN: 14761122. DOI: 10.1038/nmat732.
- [9] Deyu Wang et al. "Improving the rate performance of LiFePO<sub>4</sub> by Fe-site doping". In: *Electrochimica Acta* 50.14 (2005), pp. 2955–2958. ISSN: 00134686. DOI: 10.1016/j.electacta.2004.11.045.
- [10] Yanxuan Wen et al. "Structure and properties of LiFe0.9V0.1PO<sub>4</sub>". In: *Journal of Alloys and Compounds* 416.1-2 (2006), pp. 206–208. ISSN: 09258388. DOI: 10.1016/j.jallcom.2005.08.023.
- [11] H. Liu et al. "Doping effects of zinc on LiFePO<sub>4</sub> cathode material for lithium ion batteries". In: *Electrochemistry Communications* 8.10 (2006), pp. 1553–1557. ISSN: 13882481. DOI: 10.1016/j.elecom.2006.07.014.
- [12] Tatsuya Nakamura et al. "Structural and Surface Modifications of LiFePO<sub>4</sub> Olivine Particles and Their Electrochemical Properties". In: *Journal of The Electrochemical Society* 153.6 (2007), A1108. ISSN: 00134651. DOI: 10.1149/1.2192732.

- [13] D. Shanmukaraj et al. “Electrochemical studies on LiFe<sub>1-x</sub>CoxPO<sub>4</sub>/carbon composite cathode materials synthesized by citrate gel technique for lithium-ion batteries”. In: *Materials Science and Engineering B: Solid-State Materials for Advanced Technology* 149.1 (2008), pp. 93–98. ISSN: 09215107. DOI: 10.1016/j.mseb.2007.12.011.
- [14] Nathalie Ravet, Ali Abouimrane, and Michel Armand. “On the electronic conductivity of phospho-olivines as lithium storage electrodes”. In: *Nature Materials* 2.11 (Nov. 2003), pp. 702–702. ISSN: 1476-1122. DOI: 10.1038/nmat1009a. URL: <http://www.nature.com/articles/nmat1009a>.
- [15] Marnix Wagemaker et al. “Proof of Supervalent Doping in Olivine LiFePO<sub>4</sub>”. In: *Chemistry of Materials* 20.20 (2008), pp. 6313–6315. ISSN: 0897-4756. DOI: 10.1021/cm801781k.
- [16] Fei Zhou et al. “The electronic structure and band gap of LiFePO<sub>4</sub> and LiMnPO<sub>4</sub>”. In: *Solid State Communications* 132.3-4 (2004), pp. 181–186. ISSN: 00381098. DOI: 10.1016/j.ssc.2004.07.055.
- [17] Thomas Maxisch, Fei Zhou, and Gerbrand Ceder. “Ab initio study of the migration of small polarons in olivine LixFePO<sub>4</sub> and their association with lithium ions and vacancies”. In: *Physical Review B - Condensed Matter and Materials Physics* 73.10 (2006), pp. 1–6. ISSN: 10980121. DOI: 10.1103/PhysRevB.73.104301.
- [18] Brian Ellis et al. “Small polaron hopping in LixFePO<sub>4</sub> solid solutions: Coupled lithium-ion and electron mobility”. In: *Journal of the American Chemical Society* 128.35 (2006), pp. 11416–11422. ISSN: 00027863. DOI: 10.1021/ja0614114.
- [19] K. Zaghib et al. “Electronic, optical, and magnetic properties of LiFePO<sub>4</sub>: Small magnetic polaron effects”. In: *Chemistry of Materials* 19.15 (2007), pp. 3740–3747. ISSN: 08974756. DOI: 10.1021/cm0710296.
- [20] Khang Hoang and Michelle Johannes. “Tailoring native defects in LiFePO<sub>4</sub>: Insights from first-principles calculations”. In: *Chemistry of Materials* 23.11 (2011), pp. 3003–3013. ISSN: 08974756. DOI: 10.1021/cm200725j.
- [21] Khang Hoang and Michelle D. Johannes. “First-principles studies of the effects of impurities on the ionic and electronic conduction in LiFePO<sub>4</sub>”. In: *Journal of Power Sources* 206 (2012), pp. 274–281. ISSN: 03787753. DOI: 10.1016/j.jpowsour.2012.01.126. URL: <http://dx.doi.org/10.1016/j.jpowsour.2012.01.126>.
- [22] S. L. Dudarev et al. “Electron-energy-loss spectra and the structural stability of nickel oxide: An LSDA+U study”. In: *Phys. Rev. B* 57 (3 Jan. 1998), pp. 1505–1509. DOI: 10.1103/PhysRevB.57.1505. URL: <https://link.aps.org/doi/10.1103/PhysRevB.57.1505>.
- [23] Janina Molenda and Marcin Molenda. “Composite Cathode Material for Li-Ion Batteries Based on LiFePO<sub>4</sub> System.” In: *Metal, Ceramic and Polymeric Composites for Various Uses*. Ed. by John Cuppoletti. Rijeka: IntechOpen, 2011. Chap. 30. DOI: 10.5772/21635. URL: <https://doi.org/10.5772/21635>.
- [24] M. D. Johannes et al. “Hole polaron formation and migration in olivine phosphate materials”. In: *Physical Review B - Condensed Matter and Materials Physics* 85.11 (2012), pp. 1–6. ISSN: 10980121. DOI: 10.1103/PhysRevB.85.115106.
- [25] Yue Gu et al. “Tuning polaronic redox behavior in olivine phosphate”. In: *Physical Chemistry Chemical Physics* 21.8 (2019), pp. 4578–4583. ISSN: 14639076. DOI: 10.1039/c8cp06083e.
- [26] Zhaojun Liu, Xuejie Huang, and Dingsheng Wang. “First-principle investigations of N doping in LiFePO<sub>4</sub>”. In: *Solid State Communications* 147.11-12 (2008), pp. 505–509. ISSN: 00381098. DOI: 10.1016/j.ssc.2008.06.013.

- [27] Shyue Ping Ong, Vincent L. Chevrier, and Gerbrand Ceder. “Comparison of small polaron migration and phase separation in olivine LiMnPO<sub>4</sub> and LiFePO<sub>4</sub> using hybrid density functional theory”. In: *Physical Review B - Condensed Matter and Materials Physics* 83.7 (2011). ISSN: 10980121. DOI: 10.1103/PhysRevB.83.075112.
- [28] Ting-Feng Yi et al. “Recent developments in the doping and surface modification of LiFePO<sub>4</sub> as cathode material for power lithium ion battery”. In: *Ionics* 18.6 (June 2012), pp. 529–539. ISSN: 0947-7047. DOI: 10.1007/s11581-012-0695-y. URL: <http://link.springer.com/10.1007/s11581-012-0695-y>.
- [29] HANNES JÓNSSON, GREG MILLS, and KARSTEN W. JACOBSEN. “Nudged elastic band method for finding minimum energy paths of transitions”. In: *Classical and Quantum Dynamics in Condensed Phase Simulations*. WORLD SCIENTIFIC, June 1998, pp. 385–404. ISBN: 978-981-02-3498-0. DOI: 10.1142/9789812839664\_0016. URL: [http://www.worldscientific.com/doi/abs/10.1142/9789812839664%7B%5C\\_%7D0016](http://www.worldscientific.com/doi/abs/10.1142/9789812839664%7B%5C_%7D0016).
- [30] Graeme Henkelman, Blas P. Uberuaga, and Hannes Jónsson. “Climbing image nudged elastic band method for finding saddle points and minimum energy paths”. In: *Journal of Chemical Physics* 113.22 (2000), pp. 9901–9904. ISSN: 00219606. DOI: 10.1063/1.1329672.
- [31] Graeme Henkelman, Hannes Jónsson, and Hannes Jó Nsson. “Improved tangent estimate in the nudged elastic band method for finding minimum energy paths and saddle points A dimer method for finding saddle points on high dimensional potential surfaces using only first derivatives Optimization methods for finding mi”. In: *The Journal of Chemical Physics* 113.10 (2000), pp. 94107–2082. DOI: 10.1063/1.4961868. URL: <https://doi.org/10.1063/1.1323224%7B%5C%7D0A><http://aip.scitation.org/toc/jcp/113/22>.
- [32] Hao Lin et al. “A GGAU study of lithium diffusion in vanadium doped LiFePO<sub>4</sub>”. In: *Solid State Communications* 152.12 (2012), pp. 999–1003. ISSN: 00381098. DOI: 10.1016/j.ssc.2012.03.027. URL: <http://dx.doi.org/10.1016/j.ssc.2012.03.027>.
- [33] Guigui Xu et al. “First-principles study of structural, electronic and Li-ion diffusion properties of N-doped LiFePO<sub>4</sub> (010) surface”. In: *Solid State Ionics* 281 (2015), pp. 1–5. ISSN: 01672738. DOI: 10.1016/j.ssi.2015.08.013. URL: <http://dx.doi.org/10.1016/j.ssi.2015.08.013>.
- [34] Zhixiao Liu, Perla B. Balbuena, and Partha P. Mukherjee. “Hole Polaron Diffusion in the Final Discharge Product of Lithium-Sulfur Batteries”. In: *Journal of Physical Chemistry C* 121.32 (2017), pp. 17169–17175. ISSN: 19327455. DOI: 10.1021/acs.jpcc.7b06869.
- [35] Hua Zhang et al. “Antisite defects and Mg doping in LiFePO<sub>4</sub>: A first-principles investigation”. In: *Applied Physics A: Materials Science and Processing* 104.2 (2011), pp. 529–537. ISSN: 09478396. DOI: 10.1007/s00339-011-6309-0.
- [36] Dongxu Zhang et al. “First principles investigation on the elastic and electronic properties of Mn, Co, Nb, Mo doped LiFePO<sub>4</sub>”. In: *Computational Materials Science* 155.September (2018), pp. 410–415. ISSN: 09270256. DOI: 10.1016/j.commatsci.2018.09.010. URL: <https://doi.org/10.1016/j.commatsci.2018.09.010>.
- [37] G. Kresse and J. Hafner. “Ab initio molecular dynamics for liquid metals”. In: *Phys. Rev. B* 47 (1 1993), pp. 558–561. DOI: 10.1103/PhysRevB.47.558. URL: <https://link.aps.org/doi/10.1103/PhysRevB.47.558>.
- [38] G. Kresse and J. Furthmüller. “Efficiency of ab-initio total energy calculations for metals and semiconductors using a plane-wave basis set”. In: *Computational Materials Science* 6.1 (1996), pp. 15–50. ISSN: 0927-0256. DOI: [https://doi.org/10.1016/0927-0256\(96\)00008-0](https://doi.org/10.1016/0927-0256(96)00008-0). URL: <http://www.sciencedirect.com/science/article/pii/0927025696000080>.

- [39] G. Kresse and J. Furthmüller. “Efficient iterative schemes for ab initio total-energy calculations using a plane-wave basis set”. In: *Phys. Rev. B* 54 (16 1996), pp. 11169–11186. DOI: 10.1103/PhysRevB.54.11169. URL: <https://link.aps.org/doi/10.1103/PhysRevB.54.11169>.
- [40] Fuxiang Han. “Projector-Augmented Plane-Wave Method”. In: *Problems in Solid State Physics with Solutions* 50.24 (2012), pp. 391–396. DOI: 10.1142/9789814365031\_0023.
- [41] John P. Perdew, Kieron Burke, and Matthias Ernzerhof. “Generalized Gradient Approximation Made Simple”. In: *Phys. Rev. Lett.* 77 (18 Oct. 1996), pp. 3865–3868. DOI: 10.1103/PhysRevLett.77.3865. URL: <https://link.aps.org/doi/10.1103/PhysRevLett.77.3865>.
- [42] Lianxi Hou and Guohua Tao. “A first-principles study of bulk and surface Sn-doped LiFePO<sub>4</sub>: The role of intermediate valence component in the multivalent doping”. In: *Physica Status Solidi (B) Basic Research* 254.10 (2017). ISSN: 15213951. DOI: 10.1002/pssb.201700041.
- [43] Antonio Ruiz Puigdollers, Francesc Illas, and Gianfranco Pacchioni. “Structure and Properties of Zirconia Nanoparticles from Density Functional Theory Calculations”. In: *Journal of Physical Chemistry C* 120.8 (2016), pp. 4392–4402. ISSN: 19327455. DOI: 10.1021/acs.jpcc.5b12185.
- [44] Motoaki Nishijima et al. “Accelerated discovery of cathode materials with prolonged cycle life for lithium-ion battery”. In: *Nature Communications* 5 (2014), pp. 1–7. ISSN: 20411723. DOI: 10.1038/ncomms5553. URL: <http://dx.doi.org/10.1038/ncomms5553>.
- [45] K. W. Lee and W. E. Pickett. “Organometalliclike localization of 4d -derived spins in an inorganic conducting niobium suboxide”. In: *Physical Review B - Condensed Matter and Materials Physics* 91.19 (2015). ISSN: 1550235X. DOI: 10.1103/PhysRevB.91.195152. arXiv: [arXiv:1505.03563v1](https://arxiv.org/abs/1505.03563v1).
- [46] Hendrik J. Monkhorst and James D. Pack. “Special points for Brillouin-zone integrations”. In: *Phys. Rev. B* 13 (12 June 1976), pp. 5188–5192. DOI: 10.1103/PhysRevB.13.5188. URL: <https://link.aps.org/doi/10.1103/PhysRevB.13.5188>.
- [47] G. Rousse et al. “Magnetic Structures of the Triphylite LiFePO<sub>4</sub> and of Its Delithiated Form FePO<sub>4</sub>”. In: *Chemistry of Materials* 15.21 (2003), pp. 4082–4090. ISSN: 08974756. DOI: 10.1021/cm0300462.
- [48] Anubhav Jain et al. “Commentary: The materials project: A materials genome approach to accelerating materials innovation”. In: *APL Materials* 1.1 (2013). ISSN: 2166532X. DOI: 10.1063/1.4812323.
- [49] Hua Zeng et al. “Ab initio identification of the Li-rich phase in LiFePO<sub>4</sub>”. In: *Physical Chemistry Chemical Physics* 20.25 (2018), pp. 17497–17503. ISSN: 14639076. DOI: 10.1039/c8cp01949e.
- [50] Chang Ling Fan et al. “Structure, conductive mechanism and electrochemical performances of LiFePO<sub>4</sub>/C doped with Mg<sup>2+</sup>, Cr<sup>3+</sup> and Ti<sup>4+</sup> by a carbothermal reduction method”. In: *New Journal of Chemistry* 38.2 (2014), pp. 795–801. ISSN: 11440546. DOI: 10.1039/c3nj01285a.
- [51] N. V. Kosova and O. A. Podgornova. “Supervalent doping of LiFePO<sub>4</sub> for enhanced electrochemical performance”. In: *Chimica Techno Acta* 2.4 (2015), pp. 326–342. ISSN: 24095613. DOI: 10.15826/chimtech.2015.2.4.030.
- [52] Jianjun Yang and John S. Tse. “Li ion diffusion mechanisms in LiFePO<sub>4</sub>: An ab initio molecular dynamics study”. In: *Journal of Physical Chemistry A* 115.45 (2011), pp. 13045–13049. ISSN: 10895639. DOI: 10.1021/jp205057d.
- [53] Jongboo Jung, Maenghyo Cho, and Min Zhou. “Ab initio study of the fracture energy of LiFePO<sub>4</sub>/FePO<sub>4</sub> interfaces”. In: *Journal of Power Sources* 243 (2013), pp. 706–714. ISSN: 03787753. DOI: 10.1016/j.jpowsour.2013.06.030.
- [54] Ping Tang and N. A. W. Holzwarth. “Electronic structure of FePO<sub>4</sub>, LiFePO<sub>4</sub>, and related materials”. In: *Physical Review B* 68.16 (Oct. 2003), p. 165107. ISSN: 0163-1829. DOI: 10.1103/PhysRevB.68.165107. URL: <https://link.aps.org/doi/10.1103/PhysRevB.68.165107>.

- [55] Nonglak Meethong et al. “Aliovalent substitutions in olivine lithium iron phosphate and impact on structure and properties”. In: *Advanced Functional Materials* 19.7 (2009), pp. 1060–1070. ISSN: 1616301X. DOI: 10.1002/adfm.200801617.
- [56] Chang Kyoo Park et al. “The root cause of the rate performance improvement after metal doping: A case study of LiFePO<sub>4</sub>”. In: *Bulletin of the Korean Chemical Society* 32.3 (2011), pp. 921–926. ISSN: 02532964. DOI: 10.5012/bkcs.2011.32.3.921.
- [57] Ian D. Johnson et al. “Mechanistic insights of Li<sup>+</sup> diffusion within doped LiFePO<sub>4</sub> from Muon Spectroscopy”. In: *Scientific Reports* 8.1 (2018), pp. 1–6. ISSN: 20452322. DOI: 10.1038/s41598-018-22435-1.
- [58] G. X. Wang et al. “Synthesis and Characterization of LiFePO<sub>4</sub> and LiTi<sub>0.01</sub>Fe<sub>0.99</sub>PO<sub>4</sub> Cathode Materials”. In: *Journal of The Electrochemical Society* 153.1 (2006), A25. ISSN: 00134651. DOI: 10.1149/1.2128766. URL: <http://jes.ecsdl.org/cgi/doi/10.1149/1.2128766>.